

1 Controls on Greenland moulin geometry and evolution from the

2 Moulin Shape model

3 Lauren C. Andrews¹, Kristin Poinar^{2,3}, Celia Trunz^{4,5}

4 ¹Global Modeling and Assimilation Office, NASA Goddard Space Flight Center, Greenbelt, MD, 20771, USA

5 ²Department of Geology, University at Buffalo, Buffalo, NY, 14260, USA

6 ³Research and Education in eNergy, Environment and Water (RENEW) Program, University at Buffalo, Buffalo, NY, 14260,
7 USA

8 ⁴Geosciences Department, University of Arkansas, Fayetteville, AR, 72701, USA

9 ⁵[Department of Applied Geomatics, Université de Sherbrooke, Quebec, J1K 2R1, Canada](#)

10 **Correspondence:** Lauren C. Andrews (lauren.c.andrews@nasa.gov)

11 **Abstract.** Nearly all meltwater from glaciers and ice sheets is routed englacially through moulins. Therefore, the geometry
12 and evolution of moulins has the potential to influence subglacial water pressure variations, ice motion, and the runoff
13 hydrograph delivered to the ocean. We develop the *Moulin Shape* (MouSh) model, a time-evolving model of moulin geometry.
14 MouSh models ice deformation around a moulin using both viscous and elastic rheologies and ~~models~~ melting within the
15 moulin through heat dissipation from turbulent water flow, both above and below the water line. We force MouSh with
16 idealized and realistic surface melt inputs. Our results show that, under realistic surface melt inputs, variations in surface melt
17 change the geometry of a moulin by approximately ~~20~~10% daily and ~~by~~ over 100% seasonally. These size variations cause
18 observable differences in moulin water storage capacity, and moulin water levels, ~~and subglacial channel size~~ compared to a
19 static, cylindrical moulin. Our results suggest that moulins are important storage reservoirs for meltwater, with storage capacity
20 and water levels varying over multiple timescales. Representing/Implementing realistic moulin geometry within subglacial
21 hydrologic models ~~would~~may therefore improve the representation of subglacial pressures, especially over seasonal periods
22 or in regions where overburden pressures are high.

23 1 Introduction

24 Surface-sourced meltwater delivered to the glacier bed drives the evolution of the subglacial hydrologic system and associated
25 subglacial pressures (e.g., Iken and Bindschadler, 1986; Müller and Iken, 1973) The efficiency of the subglacial system, in
26 turn, changes the flow patterns of the overlying ice on daily, seasonal, and multi-annual timescales (e.g., Hoffman et al., 2011;
27 Iken and Bindschadler, 1986; Moon et al., 2014; Tedstone et al., 2015; Williams et al., 2020). Thus, glacial hydrology is a
28 crucial factor in short-term changes to glacier and ice sheet dynamics (Bell, 2008; Flowers, 2018).

29 On the Greenland Ice Sheet, (GIS), surface meltwater can take multiple paths, depending on its origin ~~location~~. In the
30 accumulation zone, meltwater may percolate through snow and firn, remaining liquid (Forster et al., 2014) or refreezing
31 (MacFerrin et al., 2019). In the ablation zone, meltwater runs over bare ice, coalesces into supraglacial streams, and pools into
32 supraglacial lakes (e.g., Smith et al., 2015). These surficial water features – rivers, streams, lakes, aquifers, etc. – direct
33 meltwater into englacial features that can deliver the water to the bed of the ice sheet (Andrews et al., 2014; Das et al., 2008;
34 Miège et al., 2016; Poinar et al., 2017; Smith et al., 2015). Englacial features include moulins, which are near-vertical shafts
35 with large surface catchments (~1–5 km² per moulin, Banwell et al., 2016; Colgan and Steffen, 2009; Yang and Smith, 2016),
36 and crevasses, which are linear features with limited local catchments (~0.05 km² per crevasse, Poinar et al., 2017). Together,
37 moulins and crevasses constitute a substantial fraction of the englacial hydrologic system in the ablation zone of the GIS.

38 Water fluxes through the englacial system, and therefore to the subglacial system, are non-uniform in space and time.
39 Quantifying these temporal variations in water fluxes to the glacier bed requires understanding the time evolution of the
40 supraglacial and englacial water systems that deliver it. Ongoing research is making great strides in characterizing the
41 supraglacial water network (Germain and Moorman, 2019; Smith et al., 2017; Yang et al., 2016). For instance, field
42 observations from Greenland indicate that much of the supraglacial water network terminates into crevasses and moulins
43 (McGrath et al., 2011; Smith et al., 2015) and that moulins are important modulators of surface melt inputs to the ice sheet bed
44 (Andrews et al., 2014; Cowton et al., 2013; Mejia et al., 2021; Smith et al., 2021).

45 Our knowledge of moulin sizes, scales, and time evolution has largely been informed by exploration and mapping of
46 the top tens to hundred meters of a few moulins (Benn et al., 2017; Covington et al., 2020; Gulley et al., 2009; Holmlund,
47 1988; Moreau, 2009). These sparse field data indicate that moulin shapes deviate greatly from simple cylinders. Furthermore,
48 deployments of tethered sensors into Greenland moulins have encountered irregularities including apparent ledges and plunge
49 pools (Andrews et al., 2014; Covington et al., 2020; Cowton et al., 2013), and seismic (Röösli et al., 2016) and radar (Catania
50 et al., 2008) studies suggest constrictions below the depths of human exploration. These direct near-surface and indirect deep
51 observations suggest that moulin geometry evolves a high degree of complexity at all depths.

52 State-of-the-art subglacial hydrology models are forced by meltwater inputs that enter the system through crevasses
53 or moulins. These models generally represent the geometry of moulins in a simplified and time-independent manner, for
54 instance as a static vertical cylinder (e.g., Hewitt, 2013; Hoffman et al., 2016; Werder et al., 2013) or cone (Clarke, 1996;
55 Flowers and Clarke, 2002; Werder et al., 2010). The basis for the cylindrical simplification arises from the assumption that
56 depth-dependent variations in moulin size are small relative to the vertical scale of the moulin. The basis for time independence
57 is the assumption that the moulin capacity is, again, small relative to that of the subglacial system. However, neither of these
58 assumptions have been tested. Here, we explore the extent to which time evolution of an evolving moulin geometry affects can
59 impact moulin water level, capacity, and water volume, each of which can impact the rate evolution of the subglacial meltwater
60 input and subglacial pressure in channelized regions of the bed system.

61 We present the Moulin Shape (MouSh) model, a new, physically based numeric model that evolves moulin geometry
 62 over diurnal and seasonal periods. The MouSh model can be coupled to subglacial hydrology models to more completely
 63 characterize the time evolution of the englacial and subglacial hydrologic systems, which are intimately linked.

64 2 Moulin physical model

65 We develop the Moulin Shape (MouSh) model, a numeric model of moulin evolution that considers ice deformation and ice
 66 melt associated with the dissipation of energy from turbulently flowing meltwater (Fig. 1). We include here a detailed
 67 description of the model framework and each module that influences the time-evolving geometry of the modeled moulin (Fig.
 68 2a).

69 2.1 Moulin geometry coordinate system

70 We discretize our model in the vertical (z) and radial (r_1 and r_2 , or generally r_m) directions, treating the moulin as a stack of
 71 egg-shaped (semi-circular, semi-elliptical) holes in the ice that both change in size and move laterally relative to each other.
 72 We calculate moulin geometry (elliptical radii r_1 and r_2) and water level (h_w) with a 5-minute timestep dt . Model calculations
 73 are performed in cylindrical coordinates, where $\Pi(z)$ is the perimeter of the semi-circular, semi-elliptical moulin, using
 74 Ramanujan's approximation:

$$75 \quad \Pi \approx \pi r_1 + \frac{1}{2}\pi[3(r_1 + r_2) - \sqrt{(3r_1 + r_2)(r_1 + 3r_2)}] \quad (1)$$

76 Here, r_1 and r_2 are the minor and major radii, respectively, for each node in the vertical direction. The minor radius r_1 is also
 77 the radius of the half-circle.

78 We calculate the cross-sectional area A_m of the semi-circular, semi-elliptical moulin as follows:

$$79 \quad A_m = \frac{\pi r_1}{2}(r_2 + r_1) \quad (2)$$

80 The plan-view orientation of the radii and the coordinate system, as detailed on a remotely sensed moulin, are indicated in
 81 Fig. 2b-d. The elliptical shape was chosen to reflect the observation that supraglacial meltwater flows into a moulin along a
 82 single side above the water line. This asymmetry leads to a nonuniform, noncircular geometry above the water level, ~~which~~
 83 ~~can affect the total amount and evolution of water storage at high water levels.~~ This choice is in line with observations of a
 84 GreenlandGIS moulin becoming more elliptical over time (Röösli et al., 2016). For simplicity, MouSh also contains an
 85 option to set the moulin cross-sectional geometry to a circle, rather than an egg (see Supplement S2). 2.2.

86 Each module is also dependent on the depth varying hydrostatic and cryostatic pressures. We subtract the cryostatic
 87 pressure, P_i , from the hydrostatic pressure, P_w , to get calculate the total depth-dependent effective pressure ΔP at all vertical
 88 levels z within the moulin:

$$89 \quad P_i = \rho_i g(H_i - bz) \quad (3a)$$

$$90 \quad P_w = \rho_w g(h_w - bz) \quad (3b)$$

$$P = P_w - \rho_i H_i \quad (3c)$$

where H_i is the ice thickness; h_w is the height of the water above the bed; (moulin water level); z is the vertical coordinate; ρ_i and ρ_w are ice and water density, respectively; and g is gravitational acceleration (Table 1). Note that P is not effective pressure, which is defined as $P = P_i - P_w$ (Cuffey and Paterson, 2010). In this formulation, positive pressures causes outward expansion of the moulin walls (radial growth), and negative pressures reduces the size of the moulin (radial closure). We use a flat bed at sea level for all model runs presented here, so bed elevation is $z = b = 0$.

2.2 Ice deformation modules

We represent the deformation of the ice with the simplest possible combination of elastic and viscous components: a Maxwell rheology, where elastic and viscous deformation occur independently, without interaction (Turcotte and Schubert, 2002). The Maxwell model comprises an elastic element (a spring) and a viscous element (a dashpot) in series and is standard in geophysical modeling. The response timescale in our Maxwell model is equal to $(E \times A \times \tau)^{-1}$ where E is Young's modulus, A is the viscous flow law parameter, and τ is stress (Table 1; Turcotte and Schubert, 2002). The Maxwell timescale is thus roughly 10–100 hours for typical Greenland ice. On timescales shorter than the Maxwell timescale, ice deformation is primarily elastic. On longer timescales, viscous deformation dominates.

Elastic deformation is described in Sect. 2.2.1. We represent total viscous deformation in two modes: (1) radial opening and closure of the moulin, which changes the size of the moulin (Sect. 2.2.2), and (2) vertical shear of the moulin, which changes the shape but not the size of the moulin (Sect. 2.2.3).

2.2.1 Elastic deformation

Field measurements indicate that, nearly universally during the melt season, the water level in a moulin varies at a sub-hourly timescale (Andrews et al., 2014; Covington et al., 2020; Cowton et al., 2013; Iken, 1972). This variability is shorter than, but comparable to, the Maxwell timescale for ice (10–100 hours; see Sect. 2.2); therefore, we must assume that elastic deformation plays a role in the response of the ice to variations in moulin water level.

Weertman (1971, 1973, 1996) applied dislocation fracture mechanics principles to vertical glaciological features: water-filled crevasses. These equations have applied to supraglacial lake drainages (Krawczynski et al., 2009) and slow ice hydrofracture (Poinar et al., 2017). However, these problems are Cartesian (linear), not cylindrical, so their solutions are not readily adaptable to a moulin. The stress and deformational patterns around cylindrical boreholes have been well studied in the rock mechanics literature (Amadei, 1983; Goodman, 1989; Priest, 1993). We therefore base our description of the stress field surrounding the moulin on that of a fluid-filled borehole in a porous rock medium, described by Aadnøy (1987) and based on the Kirsch equations, which describe stresses surrounding a circular hole in a rigid plate (Kirsch, 1898). We assume plane strain and approximate our moulin as a stack of such plates with analogous holes (Goodman, 1989). A subtle difference is that our moulin shape is not circular, but egg-shaped: half circular, half elliptical.

123 At each vertical level z in the moulin, we apply Hooke's Law to the stress field to calculate the strain, in horizontal
 124 cross-section, at all points on the moulin wall and in the surrounding ice for both radii r_1 and r_2 . We then integrate these strains
 125 from an infinite distance (cylindrical coordinate $r = \infty$) to the moulin wall ($r_1, r_2 = r_m$). A full derivation, based on the stress
 126 states in a borehole described by Aadnøy (1987), is in Supplement S1. We express the total radial elastic deformation r_e of a
 127 moulin segment as:

$$128 \quad r_e = \frac{r_m}{E} [(1 + \nu)N(\Delta P - \frac{1}{2}(\sigma_x \Delta \sigma_x + \sigma_y \Delta \sigma_y)) + \frac{1}{4}(\sigma_x \Delta \sigma_x - \sigma_y \Delta \sigma_y)(1 - 3\nu - 4\nu^2) + \frac{1}{4}\tau_{xy} \Delta \tau_{xy}(2 - 3\nu - 8\nu^2)] \quad (4)$$

130 Here, E is Young's modulus for uniaxial deformation; ΔP is the change in cryo-hydrostatic pressure (Eq. 3c) over a time interval,
 131 ν is Poisson's ratio; r_m is used to refer to r_1 or r_2 ; and $\sigma_x \Delta \sigma_x$, $\sigma_y \Delta \sigma_y$, and $\tau_{xy} \Delta \tau_{xy}$ are the changes in background deviatoric
 132 and shear stresses that describe the regional setting of the moulin (typically compressive and of order 100 kPa; Poinar and
 133 Andrews, 2021). The model is designed to accept user-defined deviatoric and shear stresses; however, we choose values σ_x at
 134 neutral surface stress state ($\Delta \sigma_x = \Delta \sigma_y = \Delta \tau_{xy} = 0$ kPa, $\sigma_x = 50$ kPa, and $\tau_{xy} = -50$ kPa. However, for
 135 experimental simplicity and because these stresses and their changes over time are poorly constrained,
 136 we also test the simplification $\sigma_x = \sigma_y = \tau_{xy} = 0$ (Supplement S2), which reduces elastic deformation

137 r_e :

$$138 \quad r_e = \frac{r_m}{E} (1 + \nu)N\Delta P \quad (5)$$

139 Unlike viscous deformation and melting, elastic deformation is instantaneous. However, we take advantage of the
 140 observation that elastic deformation is driven by changes in the cryostatic and hydrostatic pressures (Supplement S1.5).
 141 Therefore, we express Eq. 4 and Eq 5 as an elastic 'deformation rate' for non zero (Eq 6a) and zero (Eq 6b) stresses:

142 Therefore, we express Eq.

$$143 \quad \frac{dr_e}{dt} = \frac{1}{E} \left(r_m (1 + \nu) \frac{dN}{dt} + [(1 + \nu)N - \frac{1}{2}(\sigma_x + \sigma_y)] + \frac{1}{4}(\sigma_x - \sigma_y)(1 - 3\nu - 4\nu^2) + \frac{1}{4}\tau_{xy}(2 - 3\nu - 8\nu^2) \right) \frac{dr_m}{dt} \quad (6)$$

144 4 and Eq 5 as an elastic 'deformation rate' for varying (Eq. 6) and constant (Eq. 7) surface stresses:

$$145 \quad \frac{dr_e}{dt} = \frac{1}{E} \left(r_m (1 + \nu) \frac{dP}{dt} + [(1 + \nu) \left(-\frac{1}{2} \left(\frac{d\sigma_x}{dt} + \frac{d\sigma_y}{dt} \right) + \frac{1}{4} \left(\frac{d\sigma_x}{dt} - \frac{d\sigma_y}{dt} \right) (1 - 3\nu - 4\nu^2) + \frac{1}{4} \frac{d\tau_{xy}}{dt} (2 - 3\nu - 8\nu^2) \right] \right) \quad (6)$$

$$146 \quad \frac{dr_e}{dt} = \frac{(1 + \nu)}{E} \left(r_m \frac{dN}{dt} + N \frac{dr_m}{dt} \right) \frac{r_m}{E} (1 + \nu) \left(\frac{dP}{dt} \right) \quad (7)$$

148 Equations 6 and 7 assume that both effective pressure and moulin radius vary smoothly over the time interval in question,
 149 which is generally true for small timesteps (5-minutes in our model). We apply Eq. 6 or 7 to both moulin radii, the semi-
 150 circular radius r_1 and the semi-elliptical major radius r_2 , separately. When water is above the flotation level, elastic deformation
 151 opens the moulin at all depths below the water line. When the water level is below flotation, which is the typical case, elastic
 152 deformation closes the moulin at all depths. The values of the surface stresses σ_x , σ_y , and τ_{xy} determine the sign
 153 of the deformation above the water line. The dominant term in Eq. 6 is the first term, since $\frac{dP}{dt}$ (~1 kPa over a typical hour

154 during the melt season) greatly exceeds the rate of change of the surface stresses (~1 kPa over a year), as explained in the
 155 Supplement S1. Equation 7 is commonly used for dilatometer testing in rock mechanics (Goodman, 1989).

156 2.2.2 Viscous radial opening and closure

157 Moulins close when they lose their water source at the end of a melt season (Catania and Neumann, 2010). Similarly, boreholes
 158 close if they are not filled with drilling fluid with a density ~~similar to~~ like ice (Alley, 1992). Our modeled moulin is intermediate
 159 to these edge cases because it typically contains water. When the moulin is filled with water to the flotation level, it will stay
 160 open at its base and viscously close at and below the water level. ~~When the water level is above flotation, the~~ The moulin will
 161 viscously open in regions where hydrostatic pressure exceeds the cryostatic pressure. When the water level is below flotation,
 162 which is the typical case, viscous deformation shrinks the moulin at all depths.

163 We calculate strain rate ~~($\dot{\epsilon}$)~~ $\dot{\epsilon}$ from the total depth-dependent ~~effective~~ pressure NP (Eq. 3c) using Glen's Flow Law:

$$164 \quad \dot{\epsilon} = \underline{F_* F^*} A(T_i, P_i) \cdot \left(\frac{1}{3} N\right)^{\frac{1}{n}} \left(\frac{1}{3} P\right)^n \quad (8)$$

165 where $\underline{F_* F^*}$ is the flow law enhancement factor, ~~and~~ $A(T_i, P_i)$ is the flow law parameter, ~~and~~ n is Glen's Flow Law exponent.
 166 For the flow law parameter, we use the standard relationship from Cuffey and Paterson (2010, Eq. 3.35), which is a function
 167 of ice temperature T_i and ice pressure P_i .

168 We follow borehole studies by Naruse et al (1988) and Paterson (1977) to write strain, ϵ , in the radial direction as

$$169 \quad \epsilon = \ln\left(\frac{r_f}{r_0}\right) \quad (9)$$

170 where a moulin with initial radius r_0 and final radius r_f underwent radial strain of ϵ .

171 We use the time derivative of Eq. (9) to calculate the change in moulin radius due to viscous deformation:

$$172 \quad dr_v = r_m \exp(\dot{\epsilon} dt) - r_m \quad (10)$$

173 with strain rate given by Eq. (8). This is the same relationship used by Catania and Neumann (2010).

174 2.2.3 Shear deformation

175 We use Glen's Flow Law to calculate the change in shape of the moulin due to regional-scale ice flow. This deforms the entire
 176 moulin in bulk, shearing it in the vertical and shifting it laterally downstream, without changing its radii. Basal sliding is not
 177 currently included in the model. To represent deformation, we discretize the moulin as a stack of plates with elliptical (or
 178 circular) holes with a thickness dz and represent deformational ice flow as displacement between these plates.

179 We calculate the rate of deformational ice flow u_d in the downstream direction from ice temperature T_i and pressure
 180 NP_i , surface slope α , a constant ~~enhancement factor F_* and ice thickness F^*~~ , and H_i , using Glen's Flow Law (Cuffey and
 181 Paterson, 2010):

$$182 \quad u_d = \underline{2F_* (\rho_i g \alpha)^{\frac{1}{n}} 2F^* (\rho_i g \alpha)^n} \cdot \int_b^{H_i} A(T_i, P_i) (H_i - z)^n dz \quad (11)$$

184 where b is the ice sheet bed. We obtain ice deformation rates of $\sim 20 \text{ m yr}^{-1}$, which is typical of the ablation zone in western
 185 Greenland (Ryser et al., 2014).

186 2.3 Phase change modules

187 The second mode that changes the geometry of the moulin is ice ablation from or accretion to the moulin walls. During the
 188 melt season, the flow of water into and through the moulin generates turbulence, which as it dissipates acts to melt back the
 189 moulin walls, expanding the size of the moulin. There is also a small component of melting due to temperature differences
 190 between the water and surrounding ice. Outside the melt season, conduction of latent heat into the surrounding ice causes
 191 stagnant water to freeze back onto the moulin walls, contracting the size of the moulin.

192 2.3.1 Refreezing

193 Refreezing occurs in cold ice when water flow is absent or slow enough that the rate of heat conduction into the
 194 surrounding ice drops the water temperature to the freezing point. These conditions occur primarily outside the melt season.
 195 When these conditions are met, we apply a radial freezing ~~term~~, which is parameterized economically, following Alley
 196 (2005):

$$197 \quad dr_f = 2 \frac{T_i - T_{pmp}}{L_f} \frac{\sqrt{\frac{k_i c_p}{\pi \rho_i}}}{\sqrt{\frac{k_i c_p}{\pi \rho_i}}} \left(\sqrt{t_t} - \sqrt{t_t - dt} \right) \quad (12)$$

198 Here, $T_i - T_{pmp}$ is the depth-varying difference between the far-field temperature (prescribed as from borehole temperature
 199 observations) and the moulin water temperature, which is taken as the pressure melting temperature T_{pmp} . L_f is the latent heat
 200 of fusion; K_i is water's thermal conductivity; C_p is the specific heat capacity of ice. The refreezing rates ~~thus~~ evolve exclusively
 201 based on the elapsed time since the cessation of turbulent flow; t_t .

202 We calculate the change in moulin water volume from freezing, V_{fz} , by summing the refrozen ice thickness in a
 203 ~~time step~~, dr_f , around the perimeter of the moulin at all depths z , and converting ice volume to water volume:

$$204 \quad V_{fz} = \frac{\rho_i}{\rho_w} \int_b^{h_w} \Pi(z) r_f(z) dz \quad (13).$$

205 2.3.2 Moulin wall melting

206 During the melt season, turbulent energy dissipation from water flowing through the moulin melts back the moulin walls. The
 207 dissipation of turbulent energy and the associated melting of the surrounding ice will increase the local moulin radius. We
 208 parameterize turbulence in two separate spatial domains: (1) within the water column of the moulin, where r_1 and r_2 are evolved
 209 uniformly, and (2) above the water level along the side of the moulin, as supraglacial input falls to the water level, where only
 210 r_2 is evolved.

211 The parameterizations of turbulently driven melting we use in both regimes rely on three simplifications. First, the
 212 volume of water moving through each vertical model node is constant within each time step. This ensures that water mass is

213 conserved and that all model elements below the water line are water filled; however, this eliminates the potential long-term
 214 storage of meltwater within plunge pools caused by non-uniform incision into the ice. Second, all energy generated from
 215 turbulent dissipation is instantaneously applied to melting the surrounding ice. This neglects any heat transport within the
 216 water, which is a common approximation in subglacial models (e.g., Hewitt, 2013; Schoof, 2010; Werder et al., 2013). Third,
 217 we also make the simplifying assumption that meltwater entering the moulin is at 0°C and at the pressure melting temperature
 218 T_{pmp} at all points below the water line, ~~though~~although we do not model the impact of this temperature change on melting
 219 because moulin water temperatures are unknown.

220

221 *Submerged zone:* Below the water line, the vertical velocity of the water is dictated by the hydraulic gradient within the system
 222 and the local cross-sectional area of the moulin. Under such conditions, head loss – the departure of the hydraulic head from
 223 that calculated by Bernoulli’s equation – reflects the energy dissipated as heat. We parameterize head loss using the Darcy–
 224 Weisbach equation, which relates water velocity u_w to changes in the hydraulic gradient dh_w/dl (head loss per unit length along
 225 flow), via the hydraulic radius R_h and a dimensionless friction factor f . Because water velocity is constrained by mass balance
 226 within the system, we calculate the head loss dh_w/dl as follows:

$$227 \quad \frac{dh_w}{dl} = \frac{u_w^2 f}{8R_h g} \quad (14)$$

228 The differential element dl represents the path length over which the water experiences head loss: ~~$dl = \sqrt{\partial x^2 + \partial z^2} dl =$~~
 229 ~~$\sqrt{dx^2 + dz^2}$~~ for horizontal distance dx and vertical drop dz . The friction factor f is a unitless model parameter that controls
 230 the rate of head loss within the system. Its value thus directly affects the amount of melting. Most subglacial models fix the
 231 Darcy–Weisbach friction factor, with values ranging from 0.01 to 0.5 (e.g., Colgan et al., 2011b; Schoof, 2010; Spring and
 232 Hutter, 1981) or use equivalent values of Manning’s n (e.g., Hewitt, 2013; Hoffman and Price, 2014). Alternatively, other
 233 models parameterize channel roughness using a geometry-dependent friction factor (e.g., Boulton et al., 2007; Clarke, 2003;
 234 Flowers, 2008). Thus, MouSh has options for fixed or variable f .

235 The friction factor within the submerged zone is indicated by f_m and in the open channel zone by f_{oc} . To explore the
 236 impact of the chosen friction factor, we complete a sensitivity study (Sect. ~~2.3 and 3.2~~ where we vary the friction factor in
 237 water filled sections, f_m , over an expected range, centered on $f_m = 0.1, 2.5, 2$ and 3.2). We use a constant $f_m = 0.1$ for all other
 238 model runs presented.

239 Because we approximate the moulin as a half-circular, half-elliptical cylinder with perimeter Π , the hydraulic radius
 240 R_h of a water filled node is:

$$241 \quad R_h = \frac{A_m}{\Pi} \quad (1615).$$

242 To calculate moulin wall melting, we use a simple energy balance equation, following previous work (e.g., Gulley et al., 2014;
 243 Jarosch and Gudmundsson, 2012; Nossokoff, 2013):

$$244 \quad \rho_i C_w (T_{pmp} - T_i) \frac{dA_m}{dt} + \rho_i L_f \frac{dA_m}{dt} = Q \left(\rho_w g \frac{dh_w}{dt} \right) Q_{out} \left(\rho_w g \frac{dh_w}{dt} \right) \quad (1716)$$

245 where C_w is the heat capacity of water. The first term represents the energy needed to warm the surrounding ice to the pressure
 246 melting temperature of water T_{pmp} . Equation (4716) can be rearranged and combined with equation (14) to provide the area
 247 of ice melted:

$$248 \quad dA_t = Q_{out} \left(\rho_w g \frac{u_{wf}^2}{4R_h g} \right) (\rho_i C_w (T_{pmp} - T_i) + \rho_i L_f)^{-1} dt \quad (4817)$$

249 ~~Where~~ Q_{out} is the discharge from the moulin-subglacial system as dictated by the subglacial model component (Sect.
 250 2.4.2); and ~~$T_i - T_{pmp}$~~ $T_{pmp} - T_i$ is the temperature difference between the water (prescribed to be at the pressure melting point)
 251 and the surrounding ice, ~~which we can.~~ We vary from site to site around Greenland T_i based on observations as described in
 252 Table 1- and Sect. 2.5.2. Note that Eq. 4817 determines the area of ice that is removed through melting. For each time step, we
 253 reframe Eq. 4817 into radial melting within an egg-shaped moulin using information about the previous geometry and the
 254 assumption that melting occurs uniformly around the perimeter:

$$255 \quad dr_t = 2dA_t / [\pi(5r_1 + 3r_2 - \sqrt{(3r_1 + r_2)(r_1 + 3r_2)})] \quad (4918).$$

256 Equation 4918 is simplified when considering a circular geometry ($r_1 = r_2$).

257

258 *Unsubmerged zone:* Above the water line, a variety of complex processes drive melting. A first-principles approach would be
 259 to quantify melting due to the potential energy loss of falling water, following the work on terrestrial waterfalls (e.g.,
 260 Scheingross and Lamb, 2017). However, nearly all waterfall-based parameterizations rely on abrasion between waterborne
 261 sediment and the substrate as the primary mechanism of erosion. Instead, we implement a simple parameterization for open-
 262 channel flow with the understanding that the complexities of thermal erosion are not completely captured. In our model, open-
 263 channel melting occurs only on the up-glacier wall of the moulin and follows two ad-hoc rules based on the slope between the
 264 vertical nodes: (1) open-channel turbulent melting is applied if the slope of the upstream moulin wall allows water to flow
 265 over it; and (2) a small, prescribed amount of melting is applied when the upstream wall slope is vertical or overhung, because
 266 while water cannot flow directly along the ice, spray and other processes likely drive some amount of melting. These cases are
 267 respectively (1) the open-channel zone and (2) the falling water zone.

268 In the open-channel zone, we use a similar approach as for melting below the water line. However, the hydraulic
 269 radius R_h is adjusted to reflect the observation that water runs down only one wall of the moulin, and a higher friction factor is
 270 used to parameterize complex geometries. Due to the presence of a discontinuity between open-channel and water-filled
 271 regions (at the water line), we parameterize the hydraulic radius of open channel flow as $R_{h_{open}} = 0.5r_2$. We also use a higher
 272 open channel friction factor f_{oc} of 0.8 to parameterize observed extensive scalloping (e.g., Gully et al., 2014; Covington et al.,
 273 2020). We apply melting to only the elliptical side of the moulin, defined by r_2 ~~derived~~ using Eq. 18. Note that the hydraulic
 274 radius prescribed for open-channel flow is likely larger than the small region over which water is flowing in the natural system
 275 (Fig. 2a,d2). Further, the resulting open channel melt dA_{oc} is applied only to the major radius to calculate the change in open
 276 channel radius dr_{oc} .

277 In the falling water zone, there is very limited interaction between the moulin walls and the water. For simplicity, we
 278 assume that a small fraction, f_p , of the potential energy lost as water falls is deposited into the moulin walls, perhaps as the
 279 kinetic energy of spray. The change in radius due to this process is as follows:

$$280 \quad dr_{mf} = f_p \frac{(\rho_w/\rho_i)gQ}{L_f H} \frac{(\rho_w/\rho_i)gQ_{out}}{L_f \Pi} dt \quad (2019)$$

282 We set f_p to 0.1 for all model runs presented [here](#).

283 We add the volume of ice melted to the water already in the moulin, similarly to Eq. 12 for V_{fz} . We calculate the
 284 change in moulin water volume from melting by summing the melted ice thickness, r_{mf} , around the perimeter of the moulin at
 285 all depths z , and converting ice volume to water volume:

$$286 \quad V_{wallmelt} = \frac{\rho_i}{\rho_w} dt \int_b^{H_i} \Pi(z) r_{mf}(z) dz + A_{oe}(z) + A_e(z) dz$$

$$287 \quad (21dt \int_b^{H_i} (\Pi(z) dr_{mf}(z) + A_{oc}(z) + A_t(z)) dz) \quad (20).$$

288 2.4 Water flux into and out of the moulin (Mass conservation)

289 Water balance within the moulin and the subglacial channel is dictated by recharge from a supraglacial stream (Q_{in} , [Sect.](#)
 290 [2.4.1described below](#)), discharge through a subglacial channel (Q_{out} , Q_{base} ; [Sect. 2.4.2described below](#)) and any change in
 291 volume due to melting or refreezing, such that the volume of water in the system (V) is:

$$292 \quad \frac{dV}{dt} = Q_{in} - Q_{out} + Q_{base} + \frac{(dV_{wallmelt} - dV_{fz})}{dt} \quad (22) \frac{(dV_{wallmelt} - dV_{fz})}{dt}$$

$$293 \quad (21).$$

294 The [integralfinal](#) term varies in space and time, with high [melt-rates of volume lost to melt](#) above the water line during
 295 the melt season (when $Q_{in} > 0$), and moderate [melt-rates of volume lost to melt](#) at and below the water line during and after
 296 the melt season, when there is water flow through the moulin ($Q_{out} > 0$) and refreezing below the water line throughout the
 297 winter (when $Q_{in} = Q_{out} = 0$). The MouSh model can also accept an additional prescribed [base-flowbaseflow](#) Q_{base} directly
 298 to the subglacial module. We design [base-flowbaseflow](#) as a loose approximation of additional subglacial water inputs from
 299 varied upstream sources, including other moulins on the same subglacial channel, regional basal melt, and the addition and
 300 removal of meltwater from subglacial storage. [Base-flowBaseflow](#) is generally required to maintain realistic moulin water
 301 levels. In the moulin runs forced by realistic Q_{in} , we represent subglacial flow from ~ 5 surrounding moulins by prescribing
 302 [base-flowbaseflow](#) as five times the running 5-day mean of Q_{in} . In other model runs, we do not include [base-flowbaseflow](#).
 303 The addition of [base-flowbaseflow](#) is designed to represent the widespread seasonal evolution of surface melt; its inclusion
 304 maintains a slightly larger subglacial channel than would otherwise occur, which reduces otherwise unrealistically large daily
 305 swings in modeled moulin water level: [\(Supplement S2.2.5\)](#).

306 2.4.1 Meltwater runoff from the ice-sheet surface

307 We force the MouSh model with time-varying water inputs from the supraglacial environment, Q_{in} . We use two different Q_{in}
308 scenarios: a simple diurnal cosine with ~~maximum and minimum discharges ranging between -1 and a mean discharge of~~ $5 \text{ m}^3\text{s}^{-1}$
309 ¹, in rough agreement with observations near the margins of the GIS (Eq. 2322, Chandler et al., 2013; McGrath et al., 2011;
310 Smith et al., 2017); and realistic supraglacial discharge over a melt season, determined by using in-situ surface melting data
311 and internally drained catchment size and geometry (Yang and Smith, 2016).

312 We use the following cosine curve to represent our simplest form of supraglacial discharge into the moulin during
313 sensitivity studies:

$$314 \quad Q_{in} = \cos(\pi(t - 19.5)/12) + 3 \text{ } \underline{\hspace{15em}} \quad (235 \text{ } \underline{\hspace{15em}}) \quad \underline{\hspace{15em}} \quad (22)$$

315

316 Here, t is time in hours and Q_{in} is in $\text{m}^3 \text{ s}^{-1}$. This function has its daily peak at 19:30 hours and a daily minimum at 07:30.

317 To examine a set of realistic moulins, we select three supraglacial basins from Yang and Smith (2016) and
318 ~~derive/extract~~ their size, distance from terminus from information provided therein (Basin 1-3; Table 2). We derive surface
319 runoff from MERRA-2 reanalysis (Gelaro et al., 2017; Smith et al., 2017). ~~Surface runoff values for the 2019 melt season were~~
320 ~~modified using a synthetic unit hydrograph derived for the ablation zone and parameters appropriate for western Greenland~~
321 ~~(Table 2, Smith et al., 2017). The use of a unit hydrograph parameterizes the time and magnitude adjustments expected from~~
322 ~~meltwater routing over the ice surface. The parameters for the unit hydrograph were determined during the middle of the melt~~
323 ~~season and therefore may inaccurately represent routing delays at the beginning and end of the melt season. Further details on~~
324 ~~supraglacial and internal catchment characteristics are included in Sect. 2.5.2. Further details on supraglacial input~~
325 ~~characteristics are included in Sect. 2.5.3.~~

326 2.4.2 Water flow from the subglacial system

327 We couple the moulin model and a single evolving subglacial channel controlled by melt opening and creep closure (Covington
328 et al., 2020; Schoof, 2010) using a reservoir-constriction model (Covington et al., 2012) that simulate flows between the moulin
329 and subglacial channel. Following Covington et al. (2020), the rate of change of moulin water level h_w is

$$330 \quad \frac{dh_w}{dt} = \frac{1}{A_m(h_w)} \frac{\partial V}{\partial t} \quad (24dV)$$

331

332 With the change in water volume within the system being dV and the volume of the moulin-subglacial system is related to the
333 channel S and the moulin cross-sectional area A_m . The water volume is related to ~~Q_{in}~~ , Q_{in} , Q_{base} and Q_{out} , where Q_{out} is the
334 meltwater output from the subglacial channel, defined as follows:

$$335 \quad Q_{out} = c_3 S^{5/4} \Psi / \sqrt{|\Psi|} \quad (2524)$$

336 ~~Here, S is the subglacial channel cross-sectional area.~~ The hydraulic gradient $\Psi = -\rho_i g \frac{d(h_w - b)}{dL}$ is a linear gradient in h_w to
337 the outlet at a horizontal distance L , where the pressure head is zero. In our calculations, the bed elevation b is zero. Finally,
338 c_3 is a flux parameter:

$$339 \quad c_3 = \frac{2^{5/4}}{\pi^{1/4}} \sqrt{\frac{\pi}{(\pi+2)\rho_w f}} \quad \text{---}$$
$$340 \quad \text{(26)} \quad \sqrt{\frac{\pi}{(\pi+2)\rho_w f_{sub}}} \quad \text{---} \quad (25)$$

341 Equation (2625) for c_3 follows Covington et al. (2020), who corrected a small error from the original Schoof (2010)
342 formulation.

343 We use an equation from Schoof (2010) for the time rate of change in subglacial channel cross-section area S , with
344 the first part describing the turbulent melting of the subglacial channel walls, and the second term describing closure due to
345 the pressure of the overlying ice, ~~which is dependent on effective pressure~~ $N = P_i - P_w$:

$$346 \quad dS = (c_1 Q_{out} \Psi - c_2 N^n S) dt \quad (2726)$$

347 Here, the constant $c_1 = \frac{1}{\rho_i L_f}$ ~~with ρ_i the ice density and L_f the latent heat fusion of ice,~~ the constant $c_2 =$
348 ~~$2A(T_i, N)n^{-n}2A_{sub}n^{-n}$~~ with the Glen's flow law parameters for the subglacial component defined as ~~$A = 6 \cdot 10^{-24} A_{sub} =$~~
349 ~~$6 \cdot 10^{-24} \text{Pa}^{-3} \text{s}^{-1}$.~~

350 Replacing Q_{out} , Ψ , and N in Eq. (2726) yields

$$351 \quad dS = c_1 c_3 S^{5/4} \left(\frac{\rho_w g h_w}{L} \right)^{3/2} - c_2 (P_i - \rho_w g h_w)^n S) dt \quad \text{---}$$
$$352 \quad \text{(2827)}$$

353 Equations (2423) and (2827) are numerically solved simultaneously, as in Schoof (2010) and Covington et al. (2021). The
354 parameters used in this module are included in Table 1 and are the same as those used in the englacial component of MouSh,
355 apart from the flow law parameter A_{sub} . In the englacial system, A is calculated from local temperature within the ice column,
356 which can be as cold as -23°C in western Greenland (Iken et al., 1993). This contrasts with the temperature at the ice-bed
357 interface, which must be at the melting point; ~~thus,~~ the subglacial component of MouSh uses a ~~higher~~ fixed A_{sub} value.

358 In its current configuration, the subglacial module provides a single set of outputs representative of conditions at the
359 moulin. This is primarily because this study focuses on the evolution of a moulin and is not representative of a channel running
360 from a moulin to the terminus in a natural system. A more complex subglacial model would more accurately resolve the spatial
361 changes in subglacial channel geometry and flow.

362 2.5 Suites of model experiments

363 To examine the sensitivity of the MouSh model to uncertain parameters, ice and meltwater characteristics, and model choices,
364 and difference from previous moulin parameterizations, we run four suites of experiments. While these experiments do not

365 cover the complete range of possibilities, they were designed to address primary uncertainties in the MouSh model and examine
366 how moulin geometry might vary spatially and temporally.

367 **2.5.1 Quasi-equilibrium and the impact of diurnal supraglacial variability**

368 Under steadily varying conditions such as a repeating diurnal variation, the modeled moulin reaches a quasi-equilibrium state
369 independent of initial conditions with melting opposing viscous and elastic deformation and the only change being driven by
370 shear deformation. ~~We examine the quasi-equilibrium state and the impact of supraglacial variability on this state. Supraglacial
371 runoff Q_m is highly variable with seasonal, event, and diurnal variability in surface melting modified by supraglacial drainage
372 basin characteristics as it is routed to a moulin.~~ Moulin water level and shape respond to these patterns of variability. To
373 examine the impact of Q_m magnitude (mean) and Q_m amplitude (variability), we perform a series of model runs that vary the
374 magnitude of a cosine curve between 1 and 20 $\text{m}^3\text{sm}^3\text{s}^{-1}$ with a fixed amplitude of 0.5 $\text{m}^3\text{sm}^3\text{s}^{-1}$ and a series of runs that vary
375 the amplitude of a cosine curve between 0 and 2 $\text{m}^3\text{sm}^3\text{s}^{-1}$ with a fixed magnitude of 5.0 $\text{m}^3\text{sm}^3\text{s}^{-1}$. The amplitude ~~asis~~ one half
376 the diurnal range. These runs use Basin 1 ice conditions (Table 2; Sect. ~~2.5.4~~ ~~with no base flow prescribed~~ ~~2.5.3~~). Further
377 details can be found in Supplement S2.1 ~~and Figures S2-4~~.

378 **2.5.2 Sensitivity to uncertain parameters**

379 We explored the sensitivity of our results to the values of seven parameters, shown in ~~FigFigs.~~ ~~3-5~~, with the prescribed ranges
380 shown in Table 1. We ~~studied~~ ~~examined~~ the effect on the water level, the moulin radius at the equilibrium water level, the
381 volume and water storage of the moulin, and the cross-sectional area of the subglacial channel at the end of a ~~ten~~ ~~40~~-day model
382 run. These values reach equilibrium, with daily oscillations superimposed, after ~~3-5-15~~ days. We also tested the dependence
383 of our results on the initial moulin radius, r_0 , which we varied across an order of magnitude from 0.65 to 5.0 meters.

384 We varied the value of a uniform deformation enhancement factor ~~EF^*~~ over an order of magnitude (~~EF^*~~ = 1 to 9),
385 which affects viscous flow of the ice surrounding the moulin. While the range of enhancement factors tested ~~exceeds that likely
386 to be observed in the field, the variation of an order of magnitude was chosen to match the range of other rheological
387 parameters.~~ ~~here cover a variety of ice conditions, including ice shelves and temperate glaciers, the GIS likely has values
388 between 4 and 6 (e.g., Cuffey and Paterson, 2010). Outside of testing the model sensitivity to the enhancement factor, we
389 assigned $F^* = 5$.~~ We also tested the effect of ice temperature, independent of the enhancement factor. We used five different
390 temperature profiles: cold ice temperatures (mean $\sim -15^\circ\text{C}$, range -23.1°C to the pressure melting point) measured in the center
391 of Jakobshavn Isbræ (Iken et al., 1991); moderate ice temperatures (mean $\sim -7^\circ\text{C}$, range -13.5°C to the pressure melting point)
392 measured at the GULL site in Pâkitsoq (Lüthi et al., 2015; Ryser et al., 2014); warmer ice temperatures (mean $\sim -5^\circ\text{C}$, range -
393 9.3°C to the pressure melting point) measured at the FOXX site in Pâkitsoq (Lüthi et al., 2015; Ryser et al., 2014); a
394 hypothetical linear profile from -5°C at the surface to 0°C at the bed; and, finally, a fully temperate ice column. These different
395 ice temperature scenarios affected the creep closure rates of ice through the temperature-dependent softness parameter A by
396 approximately a factor of 6 from the coldest profile (Iken et al., 1993) compared to the fully temperate column.

397 We also examined moulin sensitivity to elastic deformation by varying Young's modulus (E) of the ice column
398 between 1–9 GPa (Vaughan, 1995) and the sensitivity to the values of friction factors for the moulin walls. MouSh has two
399 friction factors: f_m (below the water line) and f_{ic} (above the water line). We varied these friction factors across two orders of
400 magnitude: (0.01 to 1). We did not vary the subglacial channel friction factor. Finally, we varied values for basal ice softness
401 A_{sub} over two orders of magnitude (5e-25 to 5e-23) and independently examined moulins over a range of ice thicknesses (670–
402 1570 m) and corresponding distance from the terminus (~20–110 km), which in combination results in variations in hydraulic
403 gradient.

404 2.5.3 Sensitivity to local conditions

405 We examined moulins over a range of ice thicknesses and corresponding distances from the terminus (Table 2). Each moulin
406 is associated with a supraglacial basin derived by Yang and Smith (2016). The moulins were selected based on ice thicknesses
407 that broadly represent the range of ice thicknesses within the ablation zone of the western ~~Greenland Ice Sheet~~GIS and
408 supraglacial drainage basin sizes and geometries that were visually similar to nearby drainage basins and approximately
409 representative of the mean supraglacial drainage basin area for the given ice thicknesses (553m, 741m, and 1315m). To derive
410 broadly representative Q_{in} values for each basin, we integrate 3-hourly modeled surface melting from a downscaled version
411 of MERRA-2 (Gelaro et al., 2017) over the surface area of each moulin surface drainage basin. We then use synthetic unit
412 hydrograph parameters derived for a supraglacial basin from western Greenland during the middle of the ~~2015 melt season~~
413 ~~(Smith et al., 2017) to estimate supraglacial discharge into each moulin.~~ 2019 melt season (Smith et al., 2017) to estimate
414 supraglacial discharge into each moulin. Surface runoff values for the 2019 melt season were modified using a synthetic unit
415 hydrograph derived for the ablation zone and parameters appropriate for western GIS (Smith et al., 2017) with manual
416 dampening of diurnal variability to minimize long periods of no surface melt during the beginning and end of the season. We
417 apply this dampening because the parameters for the unit hydrograph were determined during the middle of the melt season
418 and therefore may inaccurately represent routing delays at the beginning and end of the melt season.

419 The supraglacial discharge curves for each moulin are only meant to capture the seasonal change in discharge rates
420 and diurnal variability and occasional increases in runoff due to surface melt events during the 2019 melt season. The primary
421 goal of this exercise is to examine season-long and daily differences in model outputs, the variation in each model component
422 (viscous, elastic and phase change), and the relative importance of each component in driving moulin geometry and water level
423 change at different representative locations of the western ~~Greenland Ice Sheet~~GIS (Figs. 6-9).

424 2.5.4 Comparison to a cylindrical moulin

425 Subglacial models generally use a time-invariant vertical cylinder to represent moulins. To investigate and quantify the efficacy
426 of our time-evolving moulin shape model, we drove MouSh and a static cylinder with the same meltwater inputs. We use the
427 time-mean radius at the water level as the radius of the static cylinder; this is 1.6 m and 1.4 m for Basin 1 and ~~1.3 m for~~ Basin
428 2, respectively. We compared the resulting moulin water level, moulin capacity, subglacial cross-sectional area and meltwater

429 input difference (due to melt generated within the model itself) across these runs. We compared the moulin water level values
430 directly (*cylindrical water level – variable water level*) and ~~compared other metrics~~ *moulin capacity* by percentage difference
431 (*cylindrical – variable*) / (*variable*); differences are presented in Figure 10.

432 2.5.5 Sensitivity to model choices

433 As part of MouSh development, we made several decisions about how to represent moulin geometry, water inputs, and the
434 associated subglacial system that can directly impact the shape and water level of a modeled moulin. ~~These~~ *We test the impact*
435 *of these* decisions ~~include~~ *in a series of experiments, including* (1) representing moulin cross-~~sect~~ *sectional* area as a semi-
436 elliptical, semi-circular “egg” instead of as a circle (Sect. 2.1 ~~and 2.3.2~~); (2) the inclusion of ~~estimated surface stresses in the~~
437 ~~representation of~~ elastic deformation (Sect. 2.2.1); (3) the use of a parabolic ice sheet profile to determine the surface slope
438 and distance to terminus for a given ice thickness (Cuffey and Paterson, 2010); (4) the use of prescribed ~~base flow~~ *baseflow*
439 into the subglacial component of the model (Sect. 2.4); and (5) the use of a time-evolving subglacial channel (*Sect. 2.4.2*).

440 *To explore the impact of our model choices for experiments 1-4, we perform a series of comparisons against a slightly*
441 *modified seasonal run for Basin 1. This allows us to capture the effect of our choices during periods of increasing and*
442 *decreasing Q_m . We change only the parameter of interest to isolate the effect on moulin water level and moulin capacity, the*
443 *two variables that most directly affect water flow within the subglacial system. Further description of these runs is included*
444 *in Supplement S2.2 and resulting differences are highlighted in Figures S5.*

445 The first two choices pertain to the complexity of the model, with our choices being more complex; simplification
446 may be beneficial in some circumstances. ~~Choices 4 and~~ *In experiment 1, the model is initialized with the same circular*
447 *geometry as the control run (Supplement S2.2.1) but melting above the water line is uniformly distributed around the moulin*
448 *perimeter, thus there is only one radius to evolve (Supplement S2.2.2). In experiment 2, we test model sensitivity to the*
449 *inclusion of elastic deformation (Supplement S2.2.3).*

450 *Experiments 3 - 5 reflect the need for a simplicity of the current* subglacial hydrologic model and would be eliminated
451 if MouSh was configured to function with either specific observational data or with a more comprehensive subglacial model.
452 ~~We also test the impact of the magnitude and diurnal variability of Q_m on the timescale for the moulin to reach quasi-~~
453 ~~equilibrium.~~ *In experiment 4, we test using a subglacial channel length of one half, and one and one half the length defined in*
454 *the control run (Supplement S2.2.4). In experiment 4, we prescribe a lower baseflow (Supplement S2.2.5).*

455 ~~To explore the impact of our model choices for decisions 1-4~~ *In experiment 5, we perform a series of experimental*
456 *comparisons against the seasonal run for Basin 1. This allows us to capture the effect of our choices during periods of increasing*
457 *and decreasing Q_m . We change only the parameter of interest to isolate the effect on moulin water level and moulin capacity,*
458 *the two variables that most directly affect water flow within the subglacial system.*

459 ~~To~~ *examine the effect of an evolving versus a fixed-radius* ~~geometry~~ *subglacial channel (Supplement S2.2.6). The*
460 *fixed* subglacial channel, *cross-sectional area is set to 1.95 m². For these runs we complete a series of runs with the same ice*
461 *thickness and distance from terminus as Basin 1 but use a simpler Q_m , the eosinusoidally* ~~co-sinusoidally~~ *varying function*

462 described in Sect. ~~2.4.1. Further description of these runs is included~~2.4.1. Details about this simplification are described in
463 Supplement S2.2.6 with results in Figure S6.

464 3 Results

465 3.1 Quasi-equilibrium and dependence on Q_{in}

466 Under ~~uniforma constant~~ supraglacial ~~inputs~~input, the moulin water level, radius, and water capacity reach
467 equilibrium within ~~1015~~ days (red line, Fig. S2S2c). However, supraglacial inputs are rarely, if ever, uniform, so under
468 constantly varying conditions, the moulin will reach a ‘quasi-equilibrium’ state. This is a mean state (geometry, water level,
469 deformation rates) with superimposed variability on the timescale of variations in Q_{in} alone. Therefore, if the forcing is diurnal,
470 the moulin will exhibit diurnal variability from a mean state. The quasi-equilibrium state is also dependent on model
471 characteristics and parameters (Sect. 3.2; Supplement S23.2).

472 The magnitude and amplitude of Q_{in} alter the moulin water level and major radius at the mean water level (a proxy
473 for moulin geometry) in predictable ways (Fig. S2 and Fig. S3). Increasing the diurnal amplitude of Q_{in} increases the diurnal
474 variability and mean moulin water level (Fig. S2b, Fig. S4). This occurs due to the disparate timescales of ice deformation
475 versus melting. The daily increase in Q_{in} raises the water level quickly because the moulin and subglacial channel is slow to
476 expand by melting. Conversely, the nightly fall in Q_{in} is muted by a fast viscous contraction of the moulin and subglacial
477 channel. This behavior drives the daily peak in moulin water level higher above the mean water level than daily minimum
478 water level falls below it (Fig. S2b). The “extra” time spent with higher water levels reduces the visco-elastic closure of the
479 moulin while also increasing turbulent melting, resulting in a larger moulin, as indicated by the moulin radius at the mean
480 water level (Fig. S2c). Higher diurnal amplitudes in Q_{in} magnify this effect.

481 As the Q_{in} magnitude increases, both the mean water level and its diurnal variability decrease (Fig. S3a-b). This occurs
482 because the moulin becomes larger in response to increasing Q_{in} and subsequent increases in subglacial discharge. As the
483 moulin and subglacial channel widen, they can readily accommodate the fluctuations in Q_{in} with ~~more limited~~lower variations
484 in moulin water level. This accommodation is evident in the moulin radius at the mean water level (Fig. S3c). Higher Q_{in}
485 magnitude drives a linear increase in melt rates within the moulin alongside nonlinear increases in visco-elastic deformation,
486 causing an overall nonlinear increase in mean moulin water level (Fig. S4). However, when moulin water levels exceed
487 flotation, the moulin grows due to both visco-elastic deformation and melting, resulting in a moulin larger than would be
488 expected ~~moulin (red~~based on the equilibrium water level (blue line, Fig. S3c).

489 3.2 Sensitivity of MouSh to parameter values and deformational processes

490 A range of ice characteristics affect the time evolution of moulin geometry. These include the initial moulin size, temperature
491 and viscosity of the ice column, viscosity of basal ice, friction factors, and ice thickness. Some of these factors are highly
492 spatially variable (e.g., ice thickness) and others are poorly known (e.g., basal ice viscosity). We quantify the effect of these

493 factors on moulin water level and moulin volume, moulin geometry, and subglacial channel cross-sectional area over both
494 multi-day and diurnal timescales by performing multiple independent sensitivity studies (Sect. 2.3).

495 We find that moulins reach a quasi-equilibrium ~~within 10 days~~, where the mean moulin water level and the moulin
496 radius at this location ~~are constant. This oscillate consistently around a daily mean value, within 15-20 days of model~~
497 ~~initialization. The~~ quasi-equilibrium ~~value~~ is independent of the initial moulin radius (Fig. 3a–b, Fig 4a–b), ~~apart from locations~~
498 ~~above the water line (Supplement S2.2; Fig. S2.4g) where surface deviatoric and shear stresses impact moulin shape).~~

499 ~~Three major~~ Two primary parameters affect the degree of viscous ~~and elastic~~ deformation in the moulin: the ice flow
500 enhancement factor $E_2 F^*$ ~~and the ice temperature profile $T_I(z)$, and Young's modulus E~~ . We tested a span of reasonable
501 values representative of ~~Greenland glacier and ice sheet~~ ice (Table 1) and found a limited effect on moulin geometry.
502 Equilibrium moulin water level, subglacial channel area, and their diurnal variabilities remain constant (<0.1% change) over
503 the tested range of these parameters (Fig. 3d,f,h ~~&and~~ 4d,f,h). Moulin capacity and water storage show ~~moderate~~ high sensitivity
504 (~~~20~~ 100–150% in equilibrium value and ~~~40~~ 100–200% in diurnal range) across the range of $E_2 F^*$ and T_I scenarios tested; a
505 decrease in moulin capacity and water storage pair with an increase in the diurnal variability for these variables. For instance,
506 varying $E_2 F^*$ across an order of magnitude grew the equilibrium major radius by ~~23~~ 26% and shrank the equilibrium minor
507 radius by ~~44~~ 72%, with a net effect that moulins had ~~23~~ 65% less volume and ~~20~~ 58% less water storage capacity in softer ice
508 ($E_2 F^* = 9$) compared to harder ice ($E_2 F^* = 1$) (Fig. 3c–d). Similarly, the different ice temperature profiles we tested caused
509 variations of ~~11~~ 29% in moulin major radius, ~~18~~ 65% in moulin minor radius, ~~and 24~~ 63% in moulin capacity and ~~73%~~ in moulin
510 water storage, with warmer ice hosting smaller moulins (Fig. 3e–f). ~~We also varied Young's modulus E across one order of~~
511 ~~magnitude, but this affected moulin radius, water volume, and moulin capacity by ~0.01%. This is due to the low magnitude~~
512 ~~of elastic deformation overall compared to viscous deformation (Fig. 5g).~~

513 ~~We varied Young's modulus, E , across one order of magnitude. With the highest Young's modulus, moulin major~~
514 ~~radius increased by 50% compared to the lowest, minor radius decreased by 15%, moulin water volume increased by 38%,~~
515 ~~and moulin capacity increased by 56% (Fig. 3g–h). The equilibrium water level decreased insignificantly (<0.1%) and the~~
516 ~~subglacial channel area increased insignificantly (<0.1%) across this range of E . These effects are comparable to those of F_2 ,~~
517 ~~which we also varied over one order of magnitude, and T , which changed the englacial flow law parameter A by approximately~~
518 ~~a factor of 6.~~

519 ~~In contrast to the above parameters, we~~ We find that moulin geometry is strongly sensitive to the choice of basal ice
520 softness and the friction factors used within the moulin (f_m and f_{oc}). Melting due to the dissipation of turbulent energy is partially
521 controlled by the friction factors chosen for the moulin walls. The friction factor above the water line (f_{oc} , “open channel”)
522 does not significantly affect moulin water level (<0.1% change for f_{oc} variations over two orders of magnitude), moulin volume
523 (~~46%~~ 6%), moulin water storage (~~20.1%~~ 20.1%), or subglacial channel area (<0.1%) over either long or diurnal timescales (Fig. 3m–n
524 and 4m–n). However, like the deformational parameters, the open channel friction factor does affect moulin radii, with the
525 major radius growing by ~~36~~ 50% as the open channel friction factor increases over two orders of magnitude, and the minor

526 radius decreasing by 2724%. This dampens the diurnal variability in ~~both~~the major and minor radii by 70% and 24%,
527 respectively (Fig. 4m).

528 Increasing the friction factor below the water line (f_m) had similar effects to changing f_{oc} . Increasing f_m by two orders
529 of magnitude increased the cross-sectional area of the moulin by 106%, via a 1510% increase in the major radius and a 9593%
530 increase in the minor radius. The water volume increased by 116127% and the storage capacity increased by 10074% (Fig.
531 3k-l) while the equilibrium water level and the subglacial channel area changed by <0.1%. Increasing f_m also increased the
532 diurnal variability of the moulin capacity and water storage (~~Fig. 4k-l~~)by 130% and 126%, respectively, by increasing the
533 diurnal differential melt rate: (Fig. 4k-l).

534 The two parameters which have the largest impact on moulin water level are the basal ice softness A_{sub} and the
535 moulin location on the ice sheet, described jointly by the ice thickness (H_i) and distance from the terminus (L). This sensitivity
536 indicates an interplay among these parameters, the subglacial hydraulic gradient, and moulin water level.

537 We varied basal ice softness A_{sub} by two orders of magnitude. Softer basal ice increased the size and storage capacity
538 of the moulin: the major radius by 2123%, the minor radius by 2523%, the total capacity by 8841%, and the stored water
539 volume by 11288% (Fig. 3i-j). These changes also increased the equilibrium water level by 5734% and the subglacial channel
540 area by 2414%, unlike tests on englacial parameters (E , TF^* , T_i , and YE), which did not affect the water level or subglacial
541 channel area. These changes occur because softer basal ice increases the rate of subglacial creep closure, which reduces
542 subglacial channel cross-sectional area, which reduces water throughflow in the moulin and increases water level, which in
543 turn reduces the amount of viscous and elastic radial closure in the moulin. Increasing the basal ice softness to approximately
544 $10^{-23} \text{ Pa}^{-3}\text{s}^{-1}$ increases the diurnal variability in the sizes of the subglacial channel and moulin (Fig. 4i-j); however, increasing
545 A_{sub} above this value causes moulin water levels to rise high enough that diurnal fluctuations are truncated by the ice
546 thickness resulting in an observed decrease in diurnal range that would not be present in thicker ice (Fig. 4j).

547 We co-varied ice thickness and distance from terminus using a parabolic approximation for a perfectly plastic ice
548 surface profile (Cuffey and Paterson, 2010). ~~Variations~~; this covariance alters the hydraulic gradient of the system. Changes
549 in ice thickness from 670 to 1570 m (80%) increase the equilibrium subglacial ~~conditions~~channel area by 2024% and increase
550 equilibrium water levels by 107203% (Fig. 3o-p). Increasing ice thickness and distance from the terminus increases the moulin
551 major and minor radii by 47%, increases moulin volume by 9793%, and increases moulin water storage by 114235% (Fig. 4p).
552 We also find significant increases in diurnal variability in subglacial channel size (2829%), water level (105178%), moulin
553 radii (major radius 8584% and minor radius 2224%), moulin volume (130%), and moulin water storage (140750%) in thicker
554 ice farther from the terminus (Fig. 4o-p).

555 Overall, we find that MouSh-modeled moulins are primarily sensitive to the friction factors for water flow through
556 the moulin, basal ice softness, and location on the ice sheet (ice thickness and distance from the terminus). The results are less
557 sensitive to englacial material factors that govern elastic and viscous deformation. The observed sensitivity to the ice thickness
558 and distance from terminus signals that moulin geometry can vary spatially. The sensitivity to friction factors and basal ice

559 softness indicates that the values of these poorly constrained parameters should be carefully chosen and kept in mind when
560 interpreting model output.

561 3.2.1 Contributions to moulin shape

562 Figure 5 illustrates the role of each process ~~that changes moulin radius under equilibrium conditions~~, phase change, viscous
563 deformation, and elastic deformation. ~~We use standard, in determining moulin radius under different hydraulic potential~~
564 ~~gradients with median model values for all parameters~~ (Table 1). Elastic deformation has little impact on moulin shape or
565 ~~variability (Fig. 5f,g) and we vary is persistently an order of magnitude smaller than either viscous deformation or radius~~
566 ~~evolution due to phase change. Viscous deformation and phase change due to melting peak near the daily maximum water~~
567 ~~line, with the daily mean of each increasing with increasing ice thickness and distance from terminus. We find that moulin~~
568 ~~shape (Figure 5f); however, the opposite effect is observed near the bed, where lower mean water levels in moulins in thinner~~
569 ~~ice increase viscous deformation at the bed; melting also increases in response to the higher hydraulic potential gradient.~~

570 ~~At any given depth, viscous deformation and phase change due to melting are similar below the waterline; however,~~
571 ~~the diurnal variation in these parameters is quite similar across different (Fig. 5g), ice thicknesses, while~~ At the mean water
572 level, moulin capacity (Fig. 5a–e) and the diurnal range in moulin radius (Fig. 5g) increase with ice thickness. We also analyze
573 ~~temporal variations in each process (Fig. growth due to melting varies less than 0.04 m day⁻¹, with the shape of the diurnal~~
574 ~~variability dependent on the parameterization of melting both above and below the water line. In contrast, viscous deformation~~
575 ~~displays diurnal variations between 0.08 m day⁻¹ in the thinnest ice and more than 0.21 m day⁻¹ in the thickest ice (5g)).~~ The times
576 ~~of maximum melt and maximum viscous closure are slightly offset, with peak melting occurring during the most rapid decline~~
577 ~~in viscous deformation (Fig. 5g). This offset aligns with the rising limb of the input hydrograph, when the moulin is small and~~
578 ~~increases in Q_{in} raise water level and, in turn, elevate englacial melt rates and reduce viscous deformation.~~

579 ~~Melt rates both above and below the water line contribute to moulin growth (Fig. 5f–g). Melt above the water level~~
580 ~~occurs due to stream or waterfall erosive processes, which in MouSh occur only within a fraction of the total circumference~~
581 ~~(Fig. 2a,d), which manifests as growth of the major radius. The actual rate of melting, however, is also dictated by the area~~
582 ~~over which water flow occurs, which under our parameterization is related to the cross sectional area of the moulin at any~~
583 ~~given depth (Fig. 5f).~~

584 ~~Elastic deformation, like viscous deformation, closes the moulin except when the water level is above flotation. Elastic~~
585 ~~deformation rates are generally smaller than viscous rates, except between 100–300 meters above the bed, where viscous~~
586 ~~deformation is minimized by cold ice temperatures (Lüthi et al., 2015; Ryser et al., 2014). Diurnally, elastic deformation varies~~
587 ~~with a similar pattern to viscous deformation, though over less range.~~

588 3.3 Moulin shape in different environments

589 We modeled the seasonal growth and collapse of moulins in a range of environments across the [Greenland Ice Sheet GIS](#) using
590 realistic melt forcings derived for the 2019 melt season (Sect. 2.4.1 and Sect. 2.5.3). These model runs varied with respect to

591 ice thickness, moulin distance from the terminus, ~~base flow~~baseflow, and the magnitude, diurnal range, and seasonal evolution
592 of supraglacial inputs (Table 2; Fig. 6a). Overall, we find that moulin setting affects the scale of diurnal and seasonal variability
593 in the size and water capacity of moulins as well as the evolution of subglacial channels (Fig. 6 and 7).

594 The sizes of all three modeled moulins reach equilibrium with the melt forcing within ~~40-15~~ days of the onset of the
595 melt seasons (Fig. 6b–c). As the water flux increases over the next few weeks, each moulin grows in response to increasing
596 supraglacial inputs, both diurnally and with a long-term trend, ~~though~~although this growth is more significant in thicker ice
597 (Fig. 6c and Fig. 7). The subglacial channel grows with a similar pattern, but interestingly, the setting and fluxes of Basin 1
598 and Basin 2 result in very similar subglacial channel cross-sectional areas despite different moulin water levels and capacities
599 (Fig. 6d).

600 ~~Though~~Although the three moulins all evolve in a similar fashion, there are differences in moulin ~~water~~ capacity,
601 ~~equilibrium~~ water level (Fig. 6), overall moulin geometry (Fig. 7), and the magnitude of englacial deformation (Fig. 8). ~~Diurnal~~
602 ~~variation~~Basin 3 exhibits the largest seasonal change in moulin capacity ~~is slightly larger in thicker ice, part because a lower~~
603 ~~supraglacial input and subglacial hydraulic gradient results in a smaller subglacial channel and periods where moulin water~~
604 ~~level is above flotation (Fig. 6). This causes substantial variability of viscous deformation while limiting variations in melt due~~
605 ~~to higher rates of deformation within the moulin (Fig. changing moulin 8a). This occurs because daily water level (Fig. 8a).~~
606 ~~fluctuations are greater in thicker ice due to the non-linearity~~One of ice creep in conjunction with the ~~linearity~~largest periods
607 of melt driven ~~Basin 3 moulin~~ growth (Sect. 3.1). Furthermore, in thick ice, visco-elastic deformation plays a relatively larger
608 role in moulin evolution (dark purple line in Fig. 8b), for the same reason. The only exception is during periods of low diurnal
609 variability in Q_{in} , which occurred around Day ~~occurs starting at day~~ 30 of the 2019 melt season (Fig. 6a). During this period,
610 ~~the minimum daily~~supraglacial inputs ~~are quite high~~experience a step change (Fig. 7a); moulin water levels stayed near
611 flotation ~~for a few~~and were less variable for several days (Fig. 7b), keeping effective pressure near zero and retarding
612 deformation, ~~and slightly increasing melt rates~~ (Fig. ~~8b~~8a). In this case, viscous deformation hovers around zero (~~though~~
613 ~~causing and causes~~ moulin opening), resulting in a high ratio of ~~elastic~~elastic to viscous deformation and a high ratio of phase
614 change to viscous deformation (purple line in Fig. ~~9b~~8b). Similar behavior also occurs around day 110. Basins 1
615 ~~and 2 exhibit smaller seasonal variations in moulin capacity because the ratio of melting to deformation stays near one until~~
616 ~~near the end of the season (Fig. 8b). This occurs because viscous deformation in Basins 1 and 2 is only slightly lower than in~~
617 ~~Basin 3 and melt rates tend to be higher (Fig 8a) due to increased subglacial discharge associated~~ growth in moulin capacity
618 (Fig. 7e). Ultimately, this is a response to multiple days where melt inputs do not exhibit substantial diurnal variability.

619 The ratio of elastic to viscous deformation generally ranges from ~~~0.4 to ~0.7~~, depending on ice thickness (Fig. 8b).
620 Elastic deformation rates in the moulin depend on a linear function of ice thickness, while viscous rates are related to ice
621 thickness cubed. Thus, at lower elevations, the elastic contribution is maximized (~~~0.8 of~~with a higher hydraulic gradient.
622 ~~Further, there are fewer periods where water levels above flotation drive~~ viscous deformation), while at high elevations,
623 significant increases in viscous closure lowers the relative contribution of elastic deformation (~~~0.4 of~~ viscous deformation).

624 ~~This increase in viscous closure in thick ice also minimizes subglacial channel size in thick inland ice (Fig. 6d), despite closure~~
625 ~~rates being retarded by daily periods of above overburden water pressures opening.~~

626 _____ Each moulin has a different daily mean capacity (Fig. 7c). This, in addition to differences in supraglacial inputs,
627 ensures that daily moulin water level variations are substantially different across moulins. Basin 1 exhibits the largest variation
628 in daily moulin water level, followed by Basin 2 (Fig. 9a). Basin 3 shows the lowest daily change; however, this is due to at least
629 in part to the fact that water overtops the moulin nearly daily (Fig. 6b and 7m–n). Changing water levels drive changes in
630 moulin and subglacial capacity. Over the melt season, daily change in moulin capacity can be as low as ~~52%~~ during lulls in
631 diurnal melt variability (Basin 3) or as high as ~~3112%~~ following a recovery from a low melt day (Basin 1; Fig. 9b). However,
632 in general all moulins display a similar daily change in capacity of ~~~205-10%, with peak values of 12 to 13%~~.

633 The subglacial system undergoes diurnal variations in channel size between 1 and ~~2120%~~ (Fig. 9c). These changes
634 are similar in magnitude to daily capacity changes within the moulin but exhibit more variability across ice thicknesses ~~and~~.
635 ~~Like changes in moulin capacity, these variations~~ are related to the daily changes in moulin water level (Fig. 9a). This suggests
636 that the time evolution of moulin geometry ~~dampens dampen~~ the diurnal pressure fluctuations that drive subglacial channel
637 growth and collapse. Evidence for this can be seen in the temporal pattern of moulin water level and subglacial channel cross-
638 sectional area (Fig. 9a,c). ~~To test this idea, we compared results from static and time-evolving moulins (Sect. 3.4).~~

639 3.4 Comparison to cylindrical moulins

640 To examine the role moulin evolution plays in modifying the subglacial hydrologic system, we compared moulin water levels,
641 moulin capacity, and subglacial channel size between model runs with a fully evolving moulin and runs with a static cylindrical
642 moulin. We performed these tests with realistic melt inputs based on the 2019 melt season (Sect. ~~2.4.1, 2.5.3~~), at moulins with
643 low and moderate ice thicknesses (553 m – Basin 1 and 741 m – Basin 2). We defined the radius of the ~~fixed static~~ cylinder as
644 ~~the mean radius at the mean water level: 1.46 m and 1.34 m for Basin 1 and 2, respectively.~~ This results in fixed moulin cross-
645 sectional areas (~~~6 m² and ~5 m²) that are to 8 m²~~) within the range of ~~the~~ spatially invariant moulin cross-sectional areas ~2–
646 10 m² often prescribed in subglacial models (e.g., Andrews et al., 2014; Banwell et al., 2013; Bartholomew et al., 2012; Cowton
647 et al., 2016; Meierbachtol et al., 2013; Werder et al., 2013). ~~Inter-comparison of these runs allows us to examine the role~~
648 ~~moulin geometry has on subglacial pressures (Covington et al., 2020; Trunz, 2021).~~

649 Comparison of ~~moulin~~ water level, ~~moulin and~~ capacity, ~~moulin water storage, and subglacial cross sectional area~~
650 between ~~fixed static cylindrical~~ and evolving moulins show differences on both the diurnal and seasonal times scales (Fig. ~~10~~).
651 ~~Moulin water levels (fixed – variable) can be substantial (Fig. 10a–b), with short term differences driven by variable melt~~
652 ~~conditions reaching a maximum of 97 m (Basin 1) and 145 m (Basin 2), but values can also be negative, indicating that the~~
653 ~~realistic run moulin has higher water levels, up to 46 m for Basin 1 and 25 m for Basin 2. 10).~~ The long-term daily average
654 ~~differences are 6 m and 35 m for Basin 1 and Basin 2, respectively. These differences are driven by a combination of~~
655 ~~differences in moulin capacity and subglacial channel size (Fig. 10c–f) and are despite a total increase in the meltwater input~~

656 into an evolving moulin, due to melt generated from turbulent dissipation (less than 2%). These results indicate that diurnal
657 variability is an important component not effectively represented with a cylindrical moulin.

658 Generally, the evolving moulin is larger (Fig. 10c-d), stores more water and maintains a larger subglacial channel
659 (Fig. 10e,f), which all contribute to the observed difference in water levels. Midway through the melt season, the evolving
660 moulin exhibits capacities only slightly larger than those of the fixed cylinder, but these capacity differences are
661 exacerbated water level (both positive and negative) are generally great during higher Q_m values (Fig. 10e-d). As
662 meltwater lower supraglacial inputs taper at the beginning and end of the melt season (day 100), the capacity and storage
663 volume in the evolving moulin falls below that of the fixed cylinder, whose volume does not adjust in response to the forcings
664 (Fig. 10e-d). This seasonal evolution is consistent between the two ice thicknesses tested, with the relatively limited differences
665 occurring during the highest discharges (Fig. 10a-b). These values are both positive, indicating that the static radius moulin
666 has higher water levels, and negative, indicating that the evolving moulin has higher water levels. Differences in moulin water
667 level can reach nearly 20 m, but are most commonly below 10 m. The seasonal mean water level difference between the static
668 cylindrical and evolving moulin in both basins is less than 1 m.

669 The capacity differences between the variable and fixed moulin contribute directly to dampening the supraglacial
670 input signal and dampening of moulin water levels. This, in turn, drives an increase in subglacial channel size (Fig. 10e-f),
671 both diurnally and over the season. The seasonal difference between the variable and fixed moulin forcing is relatively constant,
672 though punctuated by dips associated with reduced moulin water level differences (Fig. 10a-b).

673 Moulin capacity also displays a clear seasonal pattern; in both basins, the static cylindrical moulin larger than the
674 evolving moulin at the beginning of the melt season with the evolving moulin gradually growing larger as the melt season
675 progresses (Fig. 10c-d). After peak melt (day ~60), the evolving moulin begins to viscously close and gradually becomes
676 smaller than the static cylindrical moulin. The static cylindrical moulin can be more than 100% larger than the variable moulin
677 during the tails of the melt season with the evolving moulin becoming 36% and 42% larger than the static cylindrical moulin
678 during mid-melt season. Overall, the mean capacity difference between the static cylindrical and evolving moulin is less than
679 5%, with the static cylindrical moulin being slightly larger.

680 The radius of the cylindrical moulin was chosen to minimize differences with the evolving moulin. This is evident by
681 the limited long-term differences between the two moulins in both Basin 1 and 2. As such, there is limited differences (<1%)
682 between the modeled subglacial channels. We expect difference in moulin water level, moulin capacity, and subglacial
683 geometry to change if the static cylindrical moulin geometry is poorly chosen; if the different or different experimental
684 parameters are used; or the setting changes (e.g., different hydraulic gradients). For example, we use commonly used values
685 of ice softness A for both the moulin and subglacial channel; however, these values are poorly known, and their choice can
686 directly impact the relative importance of moulin shape in dictating moulin water levels and subglacial channel size (Fig. 4).

687 3.4.5 Impact of model choices on moulin geometry

688 Chosen parameterizations have the potential to impact the representation of moulin water level and capacity (Supplement S2).
689 Overall, we find that a circular geometry has limited impact on moulin water level with the circular geometry having water
690 levels that are less than 3 m higher than the egg-shaped geometry, ~~though~~ although in nearly all instances the difference is less
691 than ~~0.5 m~~ 5 m (Fig. S5a); however, the impact on capacity is slightly larger (the circular moulin is up to ~~4731%~~ smaller) and
692 displays a seasonal trend as the egg-shaped moulin elongates along its elliptical axis (Fig. S5b). ~~Altering the deviatoric and
693 shear stresses used in the calculation of elastic deformation results in minimal changes, primarily above the water line. Moulin
694 water levels are typically within 0.25 m of the control run (Fig. S5c). Prescribing the surface stresses to be zero results in a
695 maximum increase in moulin capacity of less than 10% (Fig. S5d).S5b).~~

696 Elastic deformation within the moulin is small (Supplement S1 and S2.2.3; Figure 8a). Excluding elastic deformation
697 has a negligible impact on moulin water levels and moulin capacity (< 1%; Figure S5c-d).

698 In contrast to the previous choices, the distance from the terminus (L) and the prescribed ~~base flow~~ (baseflow Q_{base})
699 can have a substantial impact on moulin water level and capacity (Fig. S5e-h). Distance from the terminus is defined by the
700 position of a given moulin on the ice sheet, and as such is not a choice or parameter per se; however, does directly influence
701 the hydraulic gradient. A shorter L increases the hydraulic gradient and ~~base flow~~ reduces both moulin water levels and
702 capacities (Fig. S5e-f). Baseflow is used here to mitigate the use of a simplistic subglacial hydrology model. Reducing the
703 baseflow within the subglacial system increases moulin water levels and reduces moulin capacity (Fig. S5g-h).

704 Finally, we examine the impact of fixing the subglacial channel cross-sectional area S . Experimental results using a
705 fixed S and a seasonally evolving melt curve resulted in ~~extremely unrealistically~~ low and extremely high or zero water levels
706 ~~resulting in during low, early season Q_{in} and complete moulin viscous collapse of the moulin if the subglacial channel size
707 was prescribed to be too large, or persistently high (always above the ice thickness) water levels and runaway moulin growth,
708 respectively if the subglacial channel was prescribed to be too small.~~ Therefore, we explore the impact of fixing S using a
709 constant mean Q_{in} with an overlaid diurnal variability (Supplement ~~Seet~~ S2.2.6). ~~When~~ With constant variability, we can easily
710 prescribe the fixed S is smaller than to be the mean value of the time-varying subglacial channel S (1.95 m). In this instance,
711 the fixed S experiment displays a ~~variable S , similar mean~~ similar mean moulin water ~~levels are higher and exhibit less level, but lower~~
712 variability ~~while moulin capacity is larger than the experiment with a time-varying S~~ (Fig. S6). Further details are included in
713 the Supplement S2.

714 4 Discussion

715 4.1 Timescales of moulin formation and evolution

716 We consider the formation timescales of moulins in the context of the shape evolution of a mature moulin. Using MouSh, we
717 find that in the absence of external forcing, such as time-variable ~~Q_{in}~~ Q_{in} , the size of a moulin reaches its equilibrium value in

718 ~~~1–10~~15 days depending on ice -and supraglacial input conditions and initial moulin geometry (Fig. 5g, Fig. S2 and Fig. S3).
719 This relaxation time is comparable to the Maxwell time for ice (10–100 hours), as expected for a linear visco-elastic system.
720 Our relaxation time also compares well to the equilibration timescale defined by Covington et al. (2020) for their modeled
721 moulin – subglacial conduit system, which Trunz (2021) found to be 1–20 days. The most realistically sized moulins in Trunz
722 (2021) had relaxation times closer to 1 day. Their modeled system was governed solely by melt and viscous deformation and
723 lacked elastic deformation; ~~this may explain their modestly longer relaxation time compared to ours. however, elastic~~
724 deformation in MouSh is small explaining why our relaxation times are comparable.

725 If the process of moulin formation occurs on a timescale shorter than the ~~1–10~~15-day relaxation time, the formation
726 process likely will not influence the overall form of the englacial system at equilibrium. This time range includes hydrofracture
727 during rapid lake drainage (~2 hours) and slow lake drainage (<~6 days, e.g., Selmes et al., 2011), and likely also the
728 reactivation of existing moulins in ensuing melt seasons, which, based on the timing difference between surface melt onset
729 and ice acceleration, occurs over multiple days (Andrews et al., 2018; Hoffman et al., 2011). On the other hand, moulin
730 formation by cut-and-closure occurs over years to decades (Gulley et al., 2009), well above the MouSh relaxation time and the
731 Maxwell time for ice ~~and,~~ are more likely to create subvertical englacial channels. The interdependence of formation and
732 evolution of these moulins gives us less confidence in applying our model to moulins with cut-and-closure origins. Those
733 moulins primarily occur in temperate near-surface ice within polythermal glaciers (Gulley et al., 2009) and have not been
734 reported on the Greenland Ice Sheet GIS.

735 4.2 Comparison of modeled and observed moulin geometries

736 Field observations suggest that moulin geometry evolves a high degree of complexity. Observations include anecdotes of
737 difficulty deploying sensors to the bottom of a moulin, which suggests the presence of kinks, ledges, knickpoints, and other
738 twists (Andrews et al., 2014; Covington et al., 2020; Cowton et al., 2013). Complex geometry revealed during mapping moulins
739 above the water line further suggests that moulins are not simply vertical cylindrical shafts (Covington et al., 2020; Moreau,
740 2009).

741 The MouSh model suggests that the energy transfer from turbulent meltwater entering the moulin to the surrounding
742 ice drives highly spatially variable melt rates above the water line. We incorporated the open-channel melt module to allow a
743 large opening to emerge above the water line (Fig. 5a–e and 7). When we run MouSh without the open-channel module (~~See~~
744 2.3.2), the surface expression of the moulin ~~is much smaller than observed in remote sensing images~~ becomes dependent on
745 surface stresses and can in some ~~eases, the moulin will~~ instances pinch closed ~~at the ice sheet surface~~. The open channel module
746 also permits the development of an egg-shaped geometry, which is supported by seismic observations and a resonance model
747 of a moulin, which ~~suggests~~ suggests that ~~the moulin increased~~ moulins may increase in ellipticity over time (Röösli et al., 2016).

748 The value of the open-channel friction factor and the size of the spatial footprint over which melting occurs directly
749 affects the size of the upper, air-filled chamber of the moulin, which differs from when ~~treated~~ the moulin is modeled as circular
750 and open-channel melting is applied uniformly around the perimeter (Fig. S5b). MouSh ~~consistently predicts~~ can predict ledges

751 at the top and bottom of a consistent diurnal range in water level. Thus, we infer that energetic subaerial water flow drives
752 formation of moulin complexity above the water line, and diurnal fluctuations around a steady multi-day water level drive
753 ledge formation through a differential in melting and ~~visco-elastic~~viscous deformation above and below the water line.
754 Energetic water flow is commonly observed at stream-fed moulins near the peak of the melt season (Pitcher and Smith, 2019)
755 or during and immediately following rapid lake drainage (Chudley et al., 2019). This suggests that complex moulin geometries
756 form during periods of relatively consistent water supply. Conversely, multi-day rises in water level, driven by either the
757 surface water supply (Q_{in}) or the basal water supply (baseflow), can erase geometric complexities such as ledges, as seen in
758 MouSh results during a melt event (Fig. 7).

759 Above the water line, explored moulins in Greenland show highly variable shapes from moulin to moulin (e.g.,
760 Covington et al., 2020). Some moulins, for example the FOXX moulin, are nearly cylindrical within the explored depth (~100
761 m), with radii comparable to what we model (~~~2 meters~~1.5 m). Others, ~~like the Phobos moulin,~~ open some tens of meters
762 below the surface to large caverns with radii approaching 10 meters, a similar morphology to karst caves with narrow entrance
763 shafts (Covington et al., 2020). MouSh can produce large openings above the water line if we use a suitably large open channel
764 friction parameter, although we lack a narrow entrance shaft and substantial vertical variability. These differences are due to
765 the inability of model parameterizations to represent complex geometries such as scalloping, plunge pools, and knickpoint
766 migration (Gulley et al., 2014; Mankoff et al., 2017). Indeed, instead of modeling processes above the water line as turbulent
767 open flow, they could, in the future, be modeled using geomorphic parameterizations to model waterfall migration, perhaps
768 resulting in the clearer development of steps and plunge pools. This would require development and inclusion of a supraglacial
769 channel model as well.

770 Below the water line, MouSh results indicate that a cylinder is a reasonable representation for newly formed moulins
771 in Greenland. However, there are two caveats. First, moulin cross-sectional area, and thus water storage capacity, can vary
772 substantially over the course of a day or season (Fig. ~~96c. and 9b~~) and features such as englacial crevasses and reservoirs may
773 be present (e.g., McQuillan and Karlstrom, 2021). Second, in instances where moulins are reactivated over multiple melt
774 seasons (Chu, 2014; Smith et al., 2017), there may be substantial deformation, as suggested by cable breakage in boreholes
775 (Ryser et al., 2014; Wright et al., 2016).

776 Observations show a wide range of moulin volumes above the water line, and moulin volumes predicted by MouSh
777 are sensitive to the ~~value of the open channel friction factor~~consideration of turbulent melting and associated parameter
778 choices. Given the flexibility of model results, we should continue to rely on field exploration to measure moulin size and
779 geometry above the water line and make efforts to constrain the parameters that affect sub-seasonal growth and collapse.
780 MouSh results below the water line are less sensitive to uncertain parameter values, so direct observations of underwater
781 geometry would be less relevant for model validation than subaerial observations. Overall, results from the MouSh model
782 demonstrate that moulin geometry evolves substantially over diurnal to seasonal timescales and varies with ice conditions.

783 4.3 Diurnal water level oscillations and moulin size

784 Moulin geometry can directly alter the relationship between meltwater inputs and moulin water level changes – the primary
785 driver of subglacial channel evolution (Andrews et al., 2014; Cowton et al., 2013). Field measurements of moulin water levels
786 indicate diurnal oscillations of 3–12% (Covington et al., 2020), ~25% (Andrews et al., 2014), and >20% (Cowton et al., 2013)
787 of overburden pressure with mean water levels of ~70% of overburden. These diurnal fluctuations are larger than those
788 observed in boreholes, which are generally, though not always, thought to sample inefficient components of the subglacial
789 hydrologic system (Andrews et al., 2014; Meierbachtol et al., 2013; Wright et al., 2016).

790 Our model results agree well with observations of moulin water level: diurnal fluctuations of ~~15–approximately~~ 25
791 ~~to 50%~~ of overburden pressure, with larger absolute oscillations occurring in thicker ice. To explain larger-than-expected daily
792 oscillations (~10%) in thinner ice, Covington et al. (2020) incorporated moulin cross-sectional area as a free parameter into
793 their model. Matching field measurements of water level required a modeled moulin radius of ~5 m (~75 m² cross-sectional
794 area) at ice thickness 500 m and a much larger moulin (radius ~20 m and cross-sectional area ~1500 m²) at ice thickness 700
795 m (Covington et al., 2020). For comparison, MouSh predicts average radii ~~of ~1.3 to 1.4 m (~56 m² cross-sectional area) at~~
796 ~~these in similar~~ ice thicknesses using parameters described in Table 2, including substantially larger meltwater inputs compared
797 to Covington et al. (2020). The drastic differences in moulin size despite similar variations in diurnal water level between our
798 study and Covington et al. (2020) cannot easily be attributed to a single factor but may be explained by our limited ability to
799 model processes above the water line, our inclusion of ~~base flow~~ baseflow (Fig. S5g–f), substantial differences in meltwater
800 input (e.g., ~~Figs~~ Fig. S2 and S3), fluctuations in moulin capacity; ~~(Covington et al. (2020) use a fixed moulin geometry)~~, or that
801 their measured water levels were not from the same moulin they mapped englacially. ~~Nevertheless, we observe substantial~~
802 ~~differences in water level between fixed and variable geometry moulins~~ However, our results suggest that are dependent on
803 supraglacial inputs and ice conditions (Fig. 10). Water levels are less variable and generally lower in the an evolving moulins
804 compared moulin capacity may be important to the fixed cylindrical moulin. represent realistic moulin water levels and capacity
805 (Fig. 10). Thus, to match observed moulin water level fluctuations without evolving the moulin geometry, a fixed cross-
806 sectional area substantially larger than the associated subglacial channel may be necessary, as reported in Covington et al.
807 (2020).

808 4.3.4 Magnitude of viscous moulin deformation

809 Viscous and elastic deformation drive moulin closure. The role of elastic deformation in the glacial hydrologic system is
810 discussed below ~~(Seet. 4.4)~~; viscous deformation is the primary closure mechanism of moulins, boreholes and subglacial
811 channels (e.g., Catania and Neuman, 2010; Paterson, 1977, Shreve, 1972), with viscous deformation dependent on local
812 effective pressure, ice characteristics, and the geometry of the feature of interest (Flowers, 2015). Viscous deformation within
813 our moulin varies in response to meltwater inputs (Fig. 5g and Fig. 8a) with the highest deformation rates occurring at the

814 water line (Fig. 5f) because at the water line, inward cryostatic pressure is least offset by outward hydrostatic pressure (see Eq.
815 3).

816 During our realistic runs, viscous deformation can exceed 0.525 m d^{-1} for short periods at of the highest
817 elevation day at all three moulin locations (Fig. 8a). These deformation rates are substantially larger than measured borehole
818 deformation rates for the primary reasons that boreholes are often at or above flotation due to high subglacial water pressures
819 (e.g., Ryser et al., 2014) or because creep measurements are recorded in much smaller boreholes in colder ice (e.g., Paterson,
820 1997).

821 A previous moulin modeling effort focused on understanding moulin closure rates (Catania and Neumann, 2010).
822 Their results indicate that an air-filled moulin will close within a single day at the bed. However, in this instance there is no
823 opposing hydrostatic pressure. While our modeled closure rates are similar to those calculated by Catania and Neuman (2010)
824 near the surface, the moulins modeled here always contain water even at the end of the melt season (Fig. 6b). This continued
825 retention of meltwater is in line with borehole observations that subglacial pressures tend to be highest outside the melt season
826 (Downs et al., 2018) and preclude the presence of completely air-filled moulins in areas where viscous deformation rapidly
827 shuts down the hydrologic system as supraglacial inputs fall.

828 **4.45 The role of elastic deformation in ice sheet hydrology**

829 Our model results indicate that the equilibrium moulin geometry is dictated by a balance of visco-elastic deformation and
830 turbulence-driven melting (Fig. 5 and Fig. 8). In both the sensitivity study and realistic model ~~run~~ experiments, visco-elastic
831 deformation generally closes the moulin, while melting of the surrounding ice consistently opens the moulin. The exception is
832 when moulin water levels exceed flotation, in which case all three mechanisms open the moulin. In all model runs, we find
833 that ~~elastic and the rates of viscous deformation are of the same order exceed elastic deformation by three to four orders of~~
834 ~~magnitude, and that the elastic mode can be between 40% and 80% of the viscous deformation~~ (Fig. 5g and Fig. 8). ~~The~~
835 ~~importance of elastic~~ Elastic deformation ~~holds even in~~ rates are greatest near the water line and at the bottom few hundred
836 ~~meters of the ice column, where stress conditions are similar to those in subglacial models (Fig. 5f). However, the relative~~
837 ~~importance of viscous and~~, at a few centimeters per year of closure within a moulin of radius ~ 1 meter. This moulin size is
838 comparable to that of a typical subglacial channel in our model ($A \sim 2 \text{ m}^2$, or radius 1.1 m), implying that elastic closure of a
839 subglacial channel would also amount to a few centimeters per year. Elastic closure rates scale linearly with moulin radius;
840 thus, larger moulins or channels would undergo commensurately faster elastic closure. The contribution of elastic deformation
841 in closing the moulin is also dependent on the values of Young's modulus and viscous enhancement factor (Fig. 5 and Fig. 8).
842 Despite extensive study of these parameters, their values are difficult to constrain. Currently, the space of viscous and elastic
843 parameter values could conceivably allow either elastic or relative to viscous deformation to dominate the closure of a moulin.
844 This underscores the importance of including both modes in the MouSh model; increases with increasing ice thickness (Fig.
845 5f); at $H = 670$ meters, viscous deformation is 4000 times larger than elastic deformation at the water line, while at $H = 1570$
846 meters, it is 2000 times larger.

847 Current subglacial hydrology models represent subglacial channel development (opening) by turbulent energy
848 dissipation and destruction (closing) by viscous deformation alone. ~~Some more recent~~ However, work involving elastically
849 responding storage elements or elastic flexure of the ice sheet has occurred (Clarke, 1996; Dow et al., 2015), and there have
850 been efforts to use elastic deformation or fluid compressibility to improve numeric stability of channel equations (Clarke,
851 2003; Spring and Hutter, 1981, 1982). Interestingly, Clarke (2003) chose to use fluid compressibility due to model integration
852 times. Yet, elastic deformation has generally been omitted from current models of ~~subglacial channelization~~ englacial hydrology,
853 even when modeling rapid changes in meltwater inputs (< 1 day; e.g., Hewitt, 2013; Hoffman et al., 2016; Werder et al., 2013).
854 ~~This choice is likely because~~ Our investigation of the role of elastic deformation ~~was considered negligible over timescales of~~
855 ~~subglacial evolution (e.g., days to weeks). However, the importance of elastic deformation~~ in diurnally closing moulins,
856 particularly in ~~thinner~~ thicker ice (Fig. 8b and S5c,d), suggests that its exclusion from subglacial channel models ~~could~~
857 ~~result~~ should cause errors of <0.1% and is warranted. On length scales considerably larger than ~1 meter moulins, as well as
858 ~~in the underestimation of channel closure rates when water levels are below flotation~~ problems where elastic flexure is more
859 central to the geometry, elastic deformation remains important. These applications include ice shelves (e.g., Reeh et al, 2003;
860 Walker et al., 2016), large marine-terminating glaciers (Christmann et al., 2021), crevasse opening (Poinar et al., 2017), and
861 rapid supra- and subglacial lake drainage (Dow et al., 2016; Dow et al., 2015; Lai et al., 2021).

862 ~~This leads us to ask why elastic deformation is absent from subglacial models, particularly because its importance~~
863 ~~relative to viscous deformation is difficult to constrain given the current range of observed Young's modulus (Vaughan, 1995).~~
864 ~~Hypothetical subglacial channel models that included elastic deformation alongside viscous deformation would show less~~
865 ~~temporal asymmetry, particularly in thinner ice, where channel closure may be strongly dictated by elastic deformation.~~
866 ~~Elastic incorporating models would also likely predict larger diurnal variations in channel size and moulin water level. This~~
867 ~~in turn would incite stronger local pressure gradients at the bed, increasing connectivity between the channel and the~~
868 ~~surrounding distributed system.~~

869 **4.56 Moulin geometry and the englacial void ratio**

870 Subglacial hydrology models use an englacial void ratio parameter to represent bulk storage and release of meltwater in the
871 englacial system (see Flowers and Clarke (2002) for the best description). Because the englacial void ratio acts as short term,
872 pressure dependent, storage for subglacial models, it can improve the representation of diurnal water pressure fluctuations in
873 subglacial models (Flowers and Clarke, 2002) ~~and, if coupled to a dynamical ice model, corresponding diurnal variations in~~
874 ~~ice flow.~~ This parameter represents bulk behavior and is usually ~~set constant over the model domain, yet it must be~~ tuned by
875 comparing to local observations (e.g., Bartholomaus et al., 2011; Hoffman et al., 2016; Werder et al., 2013). The inclusion of
876 ~~moulin~~ time-varying moulin geometry, potentially in addition to time varying representation of englacial fractures (Gajek et
877 al., 2021), that evolve in response to meltwater inputs and subglacial pressures could reduce subglacial model dependence on
878 this ~~highly~~ parameterized englacial storage, particularly in light of observations of time varying englacial features (Church et
879 al., 2020) and meltwater content (e.g., Vankova et al, 2018).

880 Recent work suggests that fluctuations in water level are controlled by the size of the moulin near the water level
881 (Trunz, 2021): moulins with larger cross sectional areas have lower diurnal variability in water level, if given the same melt
882 input. Furthermore, our results suggest that the amount of water stored in a moulin is highly dependent on local conditions,
883 such as water pressure on daily to seasonal timescales, and ice thickness (Fig. 6c and Fig. 7). Thus, we explore the possibility
884 that detailed model based information on moulin sizes and shapes could inform the englacial void ratio used in subglacial
885 hydrology models. This would allow time dependence and finer spatial variation, including in the vertical dimension as well
886 as horizontal, than is currently possible with a bulk parameter. Periods of increased supraglacial inputs can require a sizable
887 increase in englacial void ratio for subglacial models to accurately predict moulin water level (Hoffman et al., 2016). During
888 these times, MouSh predicts rapid growth in moulin capacity (Fig. 7 and Fig. 8). This correspondence suggests plausible close
889 ties between moulin size and the englacial void ratio: moulin size modifies englacial storage spatially and temporally.

890 MouSh can be used to infer both moulin size and shape, which would effectively change the englacial void ratio in
891 all three spatial dimensions and time. The shape of the moulin imposes new temporal variability on water level and subglacial
892 channel size: moulins with large near surface chambers that funnel down to become narrower at the water line, for instance,
893 have lower magnitude and smoother variations in water level compared to cylindrical moulins, whereas moulins with small
894 surface openings that widen toward the water line have larger and peakier water level variations (Trunz, 2021). Thus, when
895 the shape of a moulin is explicitly resolved, any assumed linear relationship between melt input rates and the range or pattern
896 of oscillations in water level and subglacial channel size breaks down. The relationship also changes with the water level in
897 the moulin; hence it varies in time.

898 MouSh demonstrates that moulin capacity can vary greatly both seasonally and during short periods of large
899 variability variations in supraglacial input. Moulin growth rates are largest particularly when water levels are above flotation,
900 maximizing turbulent when both melting and outward visco-elastic/viscous deformation: work to increase moulin capacity.
901 Our results show that moulin capacity changes by ~20 up to 13% daily under realistic conditions (Fig. 409b) and ~50-100
902 to 138% over the melt season (Fig. 6c and Fig. 8b), with larger changes during periods of large supraglacial input variability
903 and at locations with thicker ice. 6c). These variations in moulin shape and size may explain difficulties with modeling
904 subglacial behavior during melt events (Cowton et al., 2016), which are sometimes addressed by temporarily increasing
905 englacial storage (Hoffman et al., 2016). Our results with MouSh lead us to recommend suggest that modeling moulin shape
906 and size be modeled alongside the evolution of the subglacial system could potentially improve the representation of subglacial
907 pressures, especially during periods of large meltwater variability, in order to more accurately predict subglacial water
908 pressures and ice motion.; however, additional development is necessary to explore the impact of multiple moulins evolving
909 along with the subglacial system.

910 Practical limits on model complexity or computational costs may preclude fully time-evolving moulin geometries.
911 While not ideal, an arbitrary static shape is still may preferable to a static cylinder (Trunz, 2021). Therefore, we interpret our
912 moulin shape results (Fig. 7) to recommend a representative shape for a static moulin. Below the water line, a cylinder is a
913 reasonable approximation, especially in thinner ice or for newly made moulins, for which full-column ice deformation is

914 minimized. Above the water line, moulin shape is widely variable in time, by location, and across parameter combinations. It
915 is especially sensitive to the friction parameter for open-channel flow (Fig. 3m and Fig. 4m), with low friction values making
916 bottle-shaped moulins that have narrow necks above the water line and larger chambers below the water line, and high friction
917 values making goblet-shaped moulins with open rooms and amphitheatres above the water line atop a narrower geometry
918 below the water line. Exploration of Greenland moulins to date has uncovered multiple goblet-shaped moulins and a few
919 instances of near-cylindrical moulins, but no bottle-shaped moulins (Covington et al., 2020; Moreau, 2009; Trunz, 2021).
920 Overall, our MouSh results support goblet-shaped moulins, although with great variation in the height and width of the upper
921 chamber.

922 **4.6.7 Limitations of the current MouSh englacial – subglacial model**

923 Moulins are a dynamic component of the channelized englacial–subglacial system, ~~and; therefore,~~ explicitly modeling their
924 evolution can ~~therefore~~ improve the accuracy of ~~englacial–subglacial~~ glacial hydrology models ~~(Sect. 3.4).~~ MouSh currently
925 uses a single subglacial channel to represent the entire subglacial system, limiting its accuracy. ~~An optional baseflow term,~~
926 which parametrizes subglacial water flow from surrounding regions, improves MouSh performance. This ~~base flow~~ baseflow,
927 added directly to the subglacial channel, is necessary to produce realistic equilibrium water levels with the realistic supraglacial
928 inputs we prescribed (Fig. 6a). The baseflow value we used does not explicitly represent any specific process because our
929 model runs resolve only a single moulin connected to a single channel, whereas in the real world, multiple moulins feed a
930 network of channels. The idealized baseflow term conceptually connects to multiple potential water sources, including (1)
931 basal melting from geothermal and frictional heating, (2) supraglacial water delivered via nearby moulins that are connected
932 to the same subglacial channel, and (3) water that moves from the channelized system to the surrounding inefficient system at
933 high pressures and then flows back into the subglacial channel at lower water pressures (Hoffman et al., 2016; Mair et al.,
934 2001, 2002; Tedstone et al., 2015).

935 The addition of baseflow maintains a larger, less variable subglacial channel. This can alternately be achieved by
936 lessening the local hydraulic gradient, thus increasing the mean water pressure along a given reach. This may locally occur
937 where one subglacial channel enters another in an arborescent network (Fountain and Walder, 1998). MouSh currently does
938 not have an interconnected network of channels; however, this is under development (Trunz, 2021).

939 We use a highly simplified model of the subglacial hydrology system: a single channel that connects the moulin to
940 the ice-sheet margin. Yet, MouSh results clearly indicate that including and evolving a moulin can ~~reduce diurnal and long-~~
941 ~~term~~ alter the hydraulic gradient of the subglacial ~~pressure~~ system via time-varying storage in the moulin (Fig. 10a). ~~This has~~
942 ~~implications for~~ 10, ~~though in our current single moulin configuration, there is limited impact on~~ subglacial channel growth
943 ~~and size (Fig. 10c). Nevertheless~~ geometry. ~~Further,~~ MouSh currently lacks a distributed system, which limits its fidelity for
944 assimilating daily meltwater volumes into the subglacial system. ~~Realistically; realistically,~~ the channelized subglacial system
945 cannot always accommodate the full volume of meltwater produced during summer days, and a portion of this water goes into
946 the distributed system (e.g., Mair et al., 2001, 2002). In our model, however, when the ~~channelized~~ system is overwhelmed,

947 the water level in the moulin rises above what is typically observed, and sometimes even exceeds the height of the ice (Figs.
948 6b, ~~S2b, S3bS4b~~). The melt-driven opening and creep closure processes in the subglacial model explain this behavior: A lower
949 water input to the moulin (Q_{in}) lowers the water flux into the subglacial system (Q_{out}), which lowers the melt rates that keep
950 subglacial channels open, reducing the size of the subglacial channels and thus further reducing the subglacial water flux. This
951 increases the water level in the moulin. Thus, a reduced rate of surface melt can counterintuitively raise the modeled water
952 level (Fig. 6 around day 30), whereas in reality, much of that water would enter the inefficient subglacial hydrologic system
953 when moulin water levels exceed flotation. If the moulin model were coupled to a two-component subglacial model that
954 represents the inefficient system alongside the channelized system, we would anticipate a much-improved ability to assimilate
955 a wide range of meltwater input rates.

956 5 Conclusions

957 Results from the MouSh model show that moulins are not static cylinders. ~~Their shapes oscillate daily by some 30% around~~
958 ~~an equilibrium value reached within the first week of diurnally oscillating inputs. Daily fluctuations~~Daily fluctuations in
959 moulin capacity change the water volume held in the englacial hydrologic system, which in turn influences the evolution of
960 the subglacial channels that moulins feed. When we represent a moulin as a static cylinder in our englacial–subglacial
961 hydrology model, these daily fluctuations can be ~~substantially over-estimated~~overestimated or underestimated, affecting the
962 volume of water stored englacially and the hydraulic gradient of the subglacial system. Modeled moulin size and shape may
963 provide a more realistic representation of moulin water level and the englacial void ratio commonly used in subglacial
964 hydrology models, particularly with future efforts to improve the parameterization of moulin development above the water
965 line. This could be achieved by using an englacial hydrology – channelized subglacial system model, such as the MouSh model
966 we present here, to characterize variability in moulin size and shape, or by coupling moulin models to more complete models
967 of the subglacial system (channelized, distributed, and optionally weakly connected) to make a unified englacial–subglacial
968 hydrology model system. Improving the representation of the englacial–subglacial system to explicitly include moulins would
969 have greatest efficacy during periods of rapidly varying supraglacial input (e.g., during the beginning and end of the melt
970 season and during melt events) and in inland areas with thick ice and high overburden pressures. These are coincident with
971 situations where subglacial models without moulins, or with implicitly static moulins, tend to perform poorly.

972

973 *Code and Data availability.* The Moulin Shape model is publicly available at [https://github.com/kpoinar/moulin-physical-](https://github.com/kpoinar/moulin-physical-model/tree/MouSh_beta_revisions)
974 ~~model/tree/MouSh_beta_revisions~~<https://github.com/kpoinar/moulin-physical-model> (we will make a release when revisions
975 are complete). The model results used in the analysis presented here are archived at the University at Buffalo Libraries at
976 <http://hdl.handle.net/10477/82587>.

977

978 *Author contributions.* L.C.A. and K.P. jointly conceived of and developed the MouSh model. Both L.C.A. and K.P. designed
979 the study, executed the model runs, analyzed the data, produced the figures, and wrote the manuscript. C.T. implemented the
980 subglacial module, participated in discussions, and edited the manuscript.

981

982 *Acknowledgements.* This work was supported by NASA Cryosphere grant 80NSSC19K0054 (L.C.A. and K.P.), the Global
983 Modeling and Assimilation Office at NASA Goddard Space Flight Center funded under the NASA Modeling, Analysis, and
984 Prediction (MAP) program (L.C.A.), the Research and Education in eEnergy, Environment and Water (RENEW) Institute at
985 the University at Buffalo (K.P.), and the United States National Science Foundation award number NSF-ANS 1603835 (C.T.).
986 We acknowledge DigitalGlobe, Inc. for providing WorldView images via the Enhanced View Web Hosting Services and the
987 support therein provided by the Polar Geospatial Center under NSF-OPP awards 1043681 and 1559691. We thank two
988 anonymous reviewers and editor Dr. Elizabeth Bagshaw for constructive feedback which substantially improved manuscript
989 clarity and completeness.

990

991 *Competing interests.* An author is a member of the editorial board of The Cryosphere. The peer-review process was guided by
992 an independent editor, and the authors have no other competing interests to declare.

993 **References**

994 Aadnøy, B. S.: A complete elastic model for fluid-induced and in-situ generated stresses with the presence of a borehole,
995 *Energy Sources*, 9, 239–259, 1987.

996 Alley, R. B.: Flow-law hypotheses for ice-sheet modeling, *J. Glac.*, 38(129), 245–256,
997 <https://doi.org/10.3189/S0022143000003658>, 1992.

998 Alley, R. B., Dupont, T. K., Parizek, B. R., and Anandakrishnan, S.: Access of surface meltwater to beds of sub-freezing
999 glaciers: preliminary insights, *Ann. Glac.*, 40, 8–14, <https://doi.org/10.3189/172756405781813483>, 2005.

1000 Amadei, B.: *Rock Anisotropy and the Theory of Stress Measurements*, Springer-Verlag, Berlin, New York., 1983.

1001 Andrews, L. C., Catania, G. A., Hoffman, M. J., Gulley, J. D., Lüthi, M. P., Ryser, C., Hawley, R. L. and Neumann, T. A.:
1002 Direct observations of evolving subglacial drainage beneath the Greenland Ice Sheet, *Nature*, 514(7520), 80–83,
1003 <https://doi.org/10.1038/nature13796>, 2014.

1004 Andrews, L. C., Hoffman, M. J., Neumann, T. A., Catania, G. A., Lüthi, M. P., Hawley, R. L., Schild, K. M., Ryser, C. and
1005 Morriss, B. F.: Seasonal Evolution of the Subglacial Hydrologic System Modified by Supraglacial Lake Drainage in Western
1006 Greenland, *J. Geophys. Res. Earth Surf.*, 123(6), 1479–1496, <https://doi.org/10.1029/2017JF004585>, 2018.

1007 Banwell, A. F., Willis, I. C. and Arnold, N. S.: Modeling subglacial water routing at Paakitsoq, W Greenland, *J. Geophys. Res.*
1008 *Earth Surf.*, 118(3), 1282–1295, <https://doi.org/10.1002/jgrf.20093>, 2013.

1009 Banwell, A. F., Hewitt, I., Willis, I. and Arnold, N.: Moulin density controls drainage development beneath the Greenland ice
1010 sheet, *J. Geophys. Res. Earth Surf.*, 2015JF003801, <https://doi.org/10.1002/2015JF003801>, 2016.

- 1011 Bartholomaeus, T. C., Anderson, R. S. and Anderson, S. P.: Growth and collapse of the distributed subglacial hydrologic system
1012 of Kennicott Glacier, Alaska, USA, and its effects on basal motion, *J. Glac.*, 57(206), 985–1002,
1013 <https://doi.org/10.3189/002214311798843269>, 2011.
- 1014 Bartholomew, I. D., Nienow, P., Sole, A., Mair, D., Cowton, T. and King, M. A.: Short-term variability in Greenland Ice Sheet
1015 motion forced by time-varying meltwater drainage: Implications for the relationship between subglacial drainage system
1016 behavior and ice velocity, *J. Geophys. Res. Earth Surf.*, 117(F3), F03002, <https://doi.org/10.1029/2011JF002220>, 2012.
- 1017 Bell, R. E.: The role of subglacial water in ice-sheet mass balance, *Nature Geosci*, 1(5), 297–304,
1018 <https://doi.org/10.1038/ngeo186>, 2008.
- 1019 Benn, D. I., Thompson, S., Gulley, J., Mertes, J., Luckman, A. and Nicholson, L.: Structure and evolution of the drainage
1020 system of a Himalayan debris-covered glacier, and its relationship with patterns of mass loss, *TC*, 11, 2247–2264,
1021 <https://doi.org/10.5194/tc-11-2247-2017>, 2017.
- 1022 Boulton, G. S., Lunn, R., Vidstrand, P. and Zatzepin, S.: Subglacial drainage by groundwater–channel coupling, and the origin
1023 of esker systems: part II—theory and simulation of a modern system, *Quat. Sci. Rev.*, 26(7–8), 1091–1105,
1024 <https://doi.org/10.1016/j.quascirev.2007.01.006>, 2007.
- 1025 Catania, G. A. and Neumann, T. A.: Persistent englacial drainage features in the Greenland Ice Sheet, *Geophys. Res. Lett.*,
1026 37(2), L02501, <https://doi.org/10.1029/2009GL041108>, 2010.
- 1027 Catania, G. A., Neumann, T. A. and Price, S. F.: Characterizing englacial drainage in the ablation zone of the Greenland Ice
1028 Sheet, *J. Glac.*, 54(187), 567–578, <https://doi.org/10.3189/002214308786570854>, 2008.
- 1029 Chandler, D. M., Wadham, J. L., Lis, G. P., Cowton, T., Sole, A., Bartholomew, I., Telling, J., Nienow, P., Bagshaw, E. B.,
1030 Mair, D., Vinen, S. and Hubbard, A.: Evolution of the subglacial drainage system beneath the Greenland Ice Sheet revealed
1031 by tracers, *Nature Geosci*, 6(3), 195–198, <https://doi.org/10.1038/ngeo1737>, 2013.
- 1032 [Christmann, J., Helm, V., Khan, S. A., Kleiner, T., Müller, R., Morlighem, M., Neckel, N., Rückamp, M., Steinhage, D.,
1033 Zeising, O., and Humbert, A.: Elastic deformation plays a non-negligible role in Greenland’s outlet glacier flow, *Commun
1034 Earth Environ*, 2, 1–12, <https://doi.org/10.1038/s43247-021-00296-3>, 2021.](https://doi.org/10.1038/s43247-021-00296-3)
1035
- 1036 Chu, V. W.: Greenland Ice Sheet hydrology: A review, *Prog. Phys. Geogr.*, 38(1), 19–54,
1037 <https://doi.org/10.1177/0309133313507075>, 2014.
- 1038 Chudley, T. R., Christoffersen, P., Doyle, S. H., Bougamont, M., Schoonman, C. M., Hubbard, B. and James, M. R.:
1039 Supraglacial lake drainage at a fast-flowing Greenlandic outlet glacier, *PNAS*, 116(51), 25468–25477,
1040 <https://doi.org/10.1073/pnas.1913685116>, 2019.
- 1041 Church, G., Grab, M., Schmelzbach, C., Bauder, A., and Maurer, H.: Monitoring the seasonal changes of an englacial conduit
1042 network using repeated ground-penetrating radar measurements, *TC*, 14, 3269–3286, <https://doi.org/10.5194/tc-14-3269-2020>,
1043 2020.
- 1044 Clarke, G. K. C.: Lumped-element analysis of subglacial hydraulic circuits, *J. Geophys. Res.*, 101(B8), 17547–17559,
1045 <https://doi.org/10.1029/96JB01508>, 1996.
- 1046 Clarke, G. K. C.: Hydraulics of subglacial outburst floods: new insights from the Spring–Hutter formulation, *J. Glac.*, 49(165),
1047 299–313, <https://doi.org/10.3189/172756503781830728>, 2003.

- 1048 Colgan, W. and Steffen, K.: Modelling the spatial distribution of moulins near Jakobshavn, Greenland, IOP Conf. Ser.: Earth
1049 Environ. Sci., 6(1), 012022, <https://doi.org/10.1088/1755-1307/6/1/012022>, 2009.
- 1050 Colgan, W., Rajaram, H., Anderson, R., Steffen, K., Phillips, T., Joughin, I., Zwally, H. J. and Abdalati, W.: The annual
1051 glaciohydrology cycle in the ablation zone of the Greenland ice sheet: Part 1. Hydrology model, J. Glac., 57(204), 697–709,
1052 <https://doi.org/10.3189/002214311797409668>, 2011.
- 1053 Covington, M. D., Banwell, A. F., Gulley, J., Saar, M. O., Willis, I. and Wicks, C. M.: Quantifying the effects of glacier
1054 conduit geometry and recharge on proglacial hydrograph form, J. Hydro., 414–415, 59–71,
1055 <https://doi.org/10.1016/j.jhydrol.2011.10.027>, 2012.
- 1056 Covington, M. D., Gulley, J. D., Trunz, C., Mejia, J. and Gadd, W.: Moulin Volumes Regulate Subglacial Water Pressure on
1057 the Greenland Ice Sheet, Geophys. Res. Lett., 47(20), e2020GL088901, <https://doi.org/10.1029/2020GL088901>, 2020.
- 1058 Cowton, T., Nienow, P., Sole, A., Wadham, J., Lis, G., Bartholomew, I., Mair, D. and Chandler, D.: Evolution of drainage
1059 system morphology at a land-terminating Greenlandic outlet glacier, J. Geophys. Res. Earth Surf., 118(1), 29–41,
1060 <https://doi.org/10.1029/2012JF002540>, 2013.
- 1061 Cowton, T., Nienow, P., Bartholomew, I. and Mair, D.: Variability in ice motion at a land-terminating Greenlandic outlet
1062 glacier: the role of channelized and distributed drainage systems, J. Glac., 62(233), 451–466,
1063 <https://doi.org/10.1017/jog.2016.36>, 2016.
- 1064 Cuffey, K. M. and Paterson, W. S. B.: The Physics of Glaciers, Elsevier., 2010.
- 1065 Das, S. B., Joughin, I., Behn, M. D., Howat, I. M., King, M. A., Lizarralde, D. and Bhatia, M. P.: Fracture Propagation to the
1066 base of the Greenland Ice Sheet during supraglacial lake drainage, Science, 320(5877), 778–781,
1067 <https://doi.org/10.1126/science.1153360>, 2008.
- 1068 Dow, C. F., Kulesa, B., Rutt, I. C., Tsai, V. C., Pimentel, S., Doyle, S. H., van As, D., Lindbäck, K., Pettersson, R., Jones, G.
1069 A. and Hubbard, A.: Modeling of subglacial hydrological development following rapid supraglacial lake drainage, J. Geophys.
1070 Res. Earth Surf., 120(6), 2014JF003333, <https://doi.org/10.1002/2014JF003333>, 2015.
- 1071 [Dow, C. F., Werder, M. A., and Walker, R. T.: Modeling Antarctic subglacial lake filling and drainage cycles, 10, 1381–1393,](https://doi.org/10.5194/tc-10-1381-2016)
1072 <http://dx.doi.org/10.5194/tc-10-1381-2016>, 2016.
1073
- 1074 Downs, J. Z., Johnson, J. V., Harper, J. T., Meierbachtol, T., and Werder, M. A.: Dynamic hydraulic conductivity reconciles
1075 mismatch between modeled and observed winter subglacial water pressure, J. Geophys. Res. Earth Surf., 123(4), 818–836,
1076 <https://doi.org/10.1002/2017JF004522>, 2018.
- 1077 Flowers, G. E.: Subglacial modulation of the hydrograph from glacierized basins, Hydrol. Process., 22(19), 3903–3918,
1078 <https://doi.org/10.1002/hyp.7095>, 2008.
- 1079
- 1080 Flowers, G. E.: Modelling water flow under glaciers and ice sheets, Proc. Math. Phys. 471, 20140907–20140907,
1081 <https://doi.org/10.1098/rspa.2014.0907>, 2015.
- 1082 Flowers, G. E.: Hydrology and the future of the Greenland Ice Sheet, Nature Comm., 9(1), 2729,
1083 <https://doi.org/10.1038/s41467-018-05002-0>, 2018.
- 1084 Flowers, G. E. and Clarke, G. K. C.: A multicomponent coupled model of glacier hydrology 1. Theory and synthetic examples,
1085 J. Geophys. Res., 107(B11), 2287, <https://doi.org/10.1029/2001JB001122>, 2002.

- 1086 Forster, R. R., Box, J. E., van den Broeke, M. R., Miège, C., Burgess, E. W., van Angelen, J. H., Lenaerts, J. T. M., Koenig,
1087 L. S., Paden, J., Lewis, C., Gogineni, S. P., Leuschen, C. and McConnell, J. R.: Extensive liquid meltwater storage in firn
1088 within the Greenland ice sheet, *Nature Geosci.*, 7(2), 95–98, <https://doi.org/10.1038/ngeo2043>, 2014.
- 1089 Fountain, A. G. and Walder, J. S.: Water flow through temperate glaciers, *Rev. Geophys.*, 36(3), 299–328,
1090 <https://doi.org/10.1029/97RG03579>, 1998.
- 1091 Gajek, W., Gräff, D., Hellmann, S., Rempel, A. W., and Walter, F.: Diurnal expansion and contraction of englacial fracture
1092 networks revealed by seismic shear wave splitting, *Comm. Earth. Environ.*, 2, 1–8, [https://doi.org/10.1038/s43247-021-00279-](https://doi.org/10.1038/s43247-021-00279-4)
1093 4, 2021.
- 1094 Gelaro, R., McCarty, W., Suárez, M. J., Todling, R., Molod, A., Takacs, L., Randles, C. A., Darmenov, A., Bosilovich, M. G.,
1095 Reichle, R., Wargan, K., Coy, L., Cullather, R., Draper, C., Akella, S., Buchard, V., Conaty, A., da Silva, A. M., Gu, W., Kim,
1096 G.-K., Koster, R., Lucchesi, R., Merkova, D., Nielsen, J. E., Partyka, G., Pawson, S., Putman, W., Rienecker, M., Schubert, S.
1097 D., Sienkiewicz, M., and Zhao, B.: The Modern-Era Retrospective Analysis for Research and Applications, Version 2
1098 (MERRA-2), *J. Climate*, 30, 5419–5454, <https://doi.org/10.1175/JCLI-D-16-0758.1>, 2017.
- 1099 Germain, S. L. S. and Moorman, B. J.: Long-term observations of supraglacial streams on an Arctic glacier, *J. Glac.*, 65(254),
1100 900–911, <https://doi.org/10.1017/jog.2019.60>, 2019.
- 1101 Goodman, R. E.: *Introduction to Rock Mechanics*, 2nd ed., Wiley, New York., 1989.
- 1102 Gulley, J. D., Benn, D. I., Sreaton, E. and Martin, J.: Mechanisms of englacial conduit formation and their implications for
1103 subglacial recharge, *Quat. Sci. Rev.*, 28(19–20), 1984–1999, <https://doi.org/10.1016/j.quascirev.2009.04.002>, 2009.
- 1104 Gulley, J. D., Spellman, P. D., Covington, M. D., Martin, J. B., Benn, D. I. and Catania, G.: Large values of hydraulic roughness
1105 in subglacial conduits during conduit enlargement: implications for modeling conduit evolution, *Earth Surf. Process.*
1106 *Landforms*, 39(3), 296–310, <https://doi.org/10.1002/esp.3447>, 2014.
- 1107 Hewitt, I. J.: Seasonal changes in ice sheet motion due to melt water lubrication, *EPSL*, 371–372, 16–25,
1108 <https://doi.org/10.1016/j.epsl.2013.04.022>, 2013.
- 1109 Hoffman, M. J. and Price, S.: Feedbacks between coupled subglacial hydrology and glacier dynamics, *J. Geophys. Res. Earth*
1110 *Surf.*, 119(3), 414–436, <https://doi.org/10.1002/2013JF002943>, 2014.
- 1111 Hoffman, M. J., Catania, G. A., Neumann, T. A., Andrews, L. C. and Rumrill, J. A.: Links between acceleration, melting, and
1112 supraglacial lake drainage of the western Greenland Ice Sheet, *J. Geophys. Res. Earth Surf.*, 116(F4), F04035,
1113 <https://doi.org/10.1029/2010JF001934>, 2011.
- 1114 Hoffman, M. J., Andrews, L. C., Price, S. A., Catania, G. A., Neumann, T. A., Lüthi, M. P., Gulley, J., Ryser, C., Hawley, R.
1115 L. and Morriss, B.: Greenland subglacial drainage evolution regulated by weakly connected regions of the bed, *Nature Comm.*,
1116 7, 13903, <https://doi.org/10.1038/ncomms13903>, 2016.
- 1117 Holmlund, P.: Internal geometry and evolution of moulins, *J. Glac.*, 34(117), 242–248, 1988.
- 1118 Iken, A.: Measurements of water pressure in moulins as part of a movement study of the White Glacier, Axel Heiberg Island,
1119 Northwest Territories, Canada, *J. Glac.*, 11(61), 53–58, 1972.
- 1120 Iken, A. and Bindschadler, R.: Combined measurements of subglacial water pressure and surface velocity of Findelengletscher,
1121 Switzerland: conclusions about drainage system and sliding mechanism, *J. Glac.*, 32(110), 101–119,
1122 <https://doi.org/10.3189/S0022143000006936>, 1986.

- 1123 Iken, A., Echelmeyer, K., Harrison, W. and Funk, M.: Mechanisms of fast flow in Jakobshavns Isbræ, West Greenland: Part
1124 I. Measurements of temperature and water level in deep boreholes, *J. Glac.*, 39(131), 15–25,
1125 <https://doi.org/10.1017/S0022143000015689>, 1993.
- 1126 Jarosch, A. H. and Gudmundsson, M. T.: A numerical model for meltwater channel evolution in glaciers, *TC*, 6(2), 493–503,
1127 <https://doi.org/10.5194/tc-6-493-2012>, 2012.
- 1128 Kirsch, G.: *Die Theorie der Elastizität und die Bedürfnisse der Festigkeitslehre*, Springer, Berlin., 1898.
- 1129 Krawczynski, M. J., Behn, M. D., Das, S. B., and Joughin, I.: Constraints on the lake volume required for hydro-fracture
1130 through ice sheets, *Geophys. Res. Lett.*, 36, L10501, <https://doi.org/10.1029/2008GL036765>, 2009.
- 1131 [Lai, C.-Y., Stevens, L. A., Chase, D. L., Creyts, T. T., Behn, M. D., Das, S. B., and Stone, H. A.: Hydraulic transmissivity
1132 inferred from ice-sheet relaxation following Greenland supraglacial lake drainages, *Nat Commun*, 12, 3955,
1133 <https://doi.org/10.1038/s41467-021-24186-6>, 2021.](https://doi.org/10.1038/s41467-021-24186-6)
1134
- 1135 Lüthi, M. P., Ryser, C., Andrews, L. C., Catania, G. A., Funk, M., Hawley, R. L., Hoffman, M. J. and Neumann, T. A.: Heat
1136 sources within the Greenland Ice Sheet: dissipation, temperate paleo-firn and cryo-hydrologic warming, *TC*, 9(1), 245–253,
1137 <https://doi.org/10.5194/tc-9-245-2015>, 2015.
- 1138 MacFerrin, M., Machguth, H., As, D. van, Charalampidis, C., Stevens, C. M., Heilig, A., Vandecrux, B., Langen, P. L.,
1139 Mottram, R., Fettweis, X., Broeke, M. R. van den, Pfeffer, W. T., Moussavi, M. S. and Abdalati, W.: Rapid expansion of
1140 Greenland’s low-permeability ice slabs, *Nature*, 573(7774), 403–407, <https://doi.org/10.1038/s41586-019-1550-3>, 2019.
- 1141 MacGregor, J. A., Fahnestock, M. A., Colgan, W. T., Larsen, N. K., Kjeldsen, K. K. and Welker, J. M.: The age of surface-
1142 exposed ice along the northern margin of the Greenland Ice Sheet, *J. Glac.*, 66(258), 667–684,
1143 <https://doi.org/10.1017/jog.2020.62>, 2020.
- 1144 Mair, D., Nienow, P., Willis, I. and Sharp, M.: Spatial patterns of glacier motion during a high-velocity event: Haut Glacier
1145 d’Arolla, Switzerland, *J. Glac.*, 47(156), 9–20, <https://doi.org/10.3189/172756501781832412>, 2001.
- 1146 Mair, D., Nienow, P. W., Sharp, M. J., Wohlleben, T. and Willis, I.: Influence of subglacial drainage system evolution on
1147 glacier surface motion: Haut Glacier d’Arolla, Switzerland, *J. of Geophys Res. Solid Earth*, 107(B8),
1148 <https://doi.org/10.1029/2001JB000514>, 2002.
- 1149 Mankoff, K. D., Gulley, J. D., Tulaczyk, S. M., Covington, M. D., Liu, X., Chen, Y., Benn, D. I. and Głowacki, P. S.:
1150 Roughness of a subglacial conduit under Hansbreen, Svalbard, *J. Glac.*, 1–13, <https://doi.org/10.1017/jog.2016.134>, 2017.
- 1151 McGrath, D., Colgan, W., Steffen, K., Lauffenburger, P. and Balog, J.: Assessing the summer water budget of a moulin basin
1152 in the Sermeq Avannarleq ablation region, Greenland ice sheet, *J. Glac.*, 57(205), 954–964,
1153 <https://doi.org/10.3189/002214311798043735>, 2011.
- 1154 McQuillan, M. and Karlstrom, L.: Fluid resonance in elastic-walled englacial transport networks, *J. Glac.*, 1–14,
1155 <https://doi.org/10.1017/jog.2021.48>, 2021.
- 1156 Meierbachtol, T. W., Harper, J. and Humphrey, N.: Basal Drainage System Response to Increasing Surface Melt on the
1157 Greenland Ice Sheet, *Science*, 341(6147), 777–779, <https://doi.org/10.1126/science.1235905>, 2013.
- 1158 Mejia, J. Z., Gulley, J. D., Trunz, C., Covington, M. D., Bartholomäus, T. C., Xie, S., and Dixon, T. H.: Isolated Cavities
1159 Dominate Greenland Ice Sheet Dynamic Response to Lake Drainage, *Geophys. Res. Lett.*, 48, e2021GL094762,
1160 <https://doi.org/10.1029/2021GL094762>, 2021.

- 1161 Miège, C., Forster, R. R., Brucker, L., Koenig, L. S., Solomon, D. K., Paden, J. D., Box, J. E., Burgess, E. W., Miller, J. Z.,
1162 McNerney, L., Brautigam, N., Fausto, R. S. and Gogineni, S.: Spatial extent and temporal variability of Greenland firn aquifers
1163 detected by ground and airborne radars, *J. Geophys. Res. Earth Surf.*, 121(12), 2016JF003869,
1164 <https://doi.org/10.1002/2016JF003869>, 2016.
- 1165
- 1166 Moon, T., Joughin, I., Smith, B., van den Broeke, M. R., van de Berg, W. J., Noël, B. and Usher, M.: Distinct patterns of
1167 seasonal Greenland glacier velocity, *Geophys. Res. Lett.*, 41(20), 2014GL061836, <https://doi.org/10.1002/2014GL061836>,
1168 2014.
- 1169 Moreau, L.: L'exploration du cryokarst glaciaire et son intérêt scientifique pour l'étude du drainage des eaux de fonte : porches,
1170 cavités, crevasses, bédrières et moulins., *Collection EDYTEM. Cahiers de géographie*, 8, 163–170, 2009.
- 1171 Müller, F. and Iken, A.: Velocity fluctuations and water regime of Arctic valley glaciers, *IAHS*, 95, 165–182, 1973.
- 1172 Naruse, R., Okuhira, F., Ohmae, H., Kawada, K. and Nakawo, M.: Closure Rate of a 700 m Deep Bore Hole at Mizuho Station,
1173 East Antarctica, *Ann. Glac.*, 11, 100–103, <https://doi.org/10.3189/S0260305500006406>, 1988.
- 1174 Nossokoff, A.: Using Small Scale Physical Experiments to Improve Enthalpy Based Models of Ice Sheets, M.S., University
1175 of Colorado, Boulder, 2013.
- 1176 Paterson, W. S. B.: Secondary and tertiary creep of glacier ice as measured by borehole closure rates, *Rev. Geophys.*, 15(1),
1177 47–55, <https://doi.org/10.1029/RG015i001p00047>, 1977.
- 1178 Pitcher, L. H. and Smith, L. C.: Supraglacial Streams and Rivers, *Ann. Rev. Earth Planetary Sci.*, 47(1), 421–452,
1179 <https://doi.org/10.1146/annurev-earth-053018-060212>, 2019.
- 1180 Poinar, K. and Andrews, L. C.: Challenges in predicting Greenland supraglacial lake drainages at the regional scale, *TC*, 15,
1181 1455-1483, <https://doi.org/10.5194/tc-15-1455-2021>, 2021.
- 1182 Poinar, K., Joughin, I., Das, S. B., Behn, M. D., Lenaerts, J. T. M. and van den Broeke, M. R.: Limits to future expansion of
1183 surface-melt-enhanced ice flow into the interior of western Greenland, *Geophys. Res. Lett.*, 42(6), 2015GL063192,
1184 <https://doi.org/10.1002/2015GL063192>, 2015.
- 1185 Poinar, K., Joughin, I., Lenaerts, J. T. M. and Broeke, M. R. V. D.: Englacial latent-heat transfer has limited influence on
1186 seaward ice flux in western Greenland, *J. Glac.*, 1–16, <https://doi.org/10.1017/jog.2016.103>, 2016.
- 1187 Poinar, K., Joughin, I., Lilien, D., Brucker, L., Kehrl, L. and Nowicki, S.: Drainage of Southeast Greenland Firn Aquifer Water
1188 through Crevasses to the Bed, *Front. Earth Sci.*, 5, <https://doi.org/10.3389/feart.2017.00005>, 2017.
- 1189 Priest, S. D.: *Discontinuity Analysis for Rock Engineering*, 1st ed., Chapman & Hall, London; New York., 1993.
- 1190 [Reeh, N., Christensen, E. L., Mayer, C., and Olesen, O. B.: Tidal bending of glaciers: a linear viscoelastic approach, 37, 83–](https://doi.org/10.3189/172756403781815663)
1191 [89, https://doi.org/10.3189/172756403781815663](https://doi.org/10.3189/172756403781815663), 2003.
- 1192
- 1193 Röösl, C., Walter, F., Ampuero, J.-P., and Kissling, E.: Seismic moulin tremor, *J. Geophys. Res. Solid Earth* 121, 5838–5858,
1194 <https://doi.org/10.1002/2015JB012786>, 2016.
- 1195 Ryser, C., Lüthi, M. P., Andrews, L. C., Hoffman, M. J., Catania, G. A., Hawley, R. L., Neumann, T. A. and Kristensen, S. S.:
1196 Sustained high basal motion of the Greenland ice sheet revealed by borehole deformation, *J. Glac.*, 60(222), 647–660,
1197 <https://doi.org/10.3189/2014JoG13J196>, 2014.

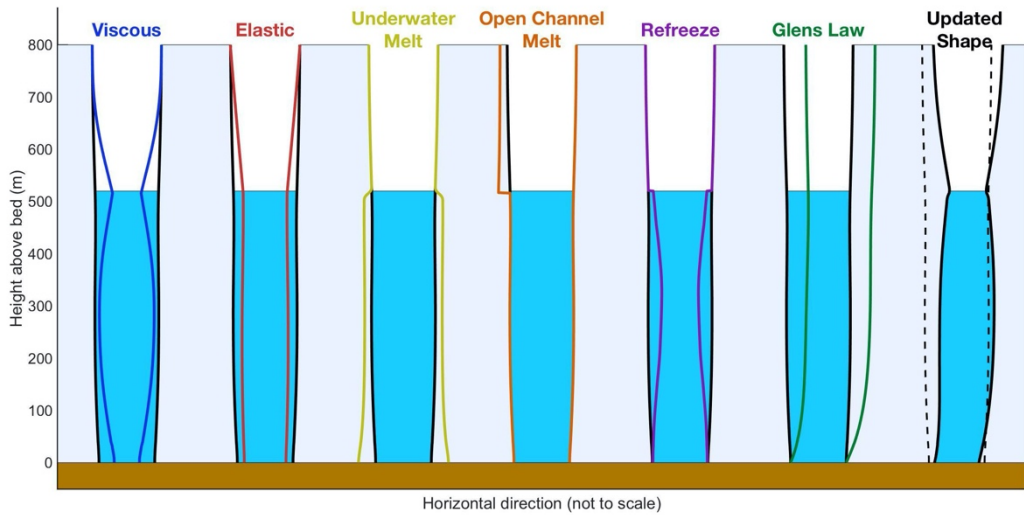
- 1198 Scheingross, J. S. and Lamb, M. P.: A Mechanistic Model of Waterfall Plunge Pool Erosion into Bedrock, *J. Geophys. Res. Earth Surf.*, 122(11), 2079–2104, <https://doi.org/10.1002/2017JF004195>, 2017.
- 1200 Schoof, C.: Ice-sheet acceleration driven by melt supply variability, *Nature*, 468(7325), 803–806,
1201 <https://doi.org/10.1038/nature09618>, 2010.
- 1202 Selmes, N., Murray, T. and James, T. D.: Fast draining lakes on the Greenland Ice Sheet, *Geophys. Res. Lett.*, 38(15), L15501,
1203 <https://doi.org/10.1029/2011GL047872>, 2011.
- 1204 Shreve, R. L.: Movement of water in glaciers, *J. Glac.*, 11(62), 205–214, <https://doi.org/10.1017/S002214300002219X>, 1972.
- 1205 Smith, L. C., Chu, V. W., Yang, K., Gleason, C. J., Pitcher, L. H., Rennermalm, A. K., Legleiter, C. J., Behar, A. E., Overstreet,
1206 B. T., Moustafa, S. E., Tedesco, M., Forster, R. R., LeWinter, A. L., Finnegan, D. C., Sheng, Y. and Balog, J.: Efficient
1207 meltwater drainage through supraglacial streams and rivers on the southwest Greenland ice sheet, *PNAS*, 112(4), 1001–1006,
1208 <https://doi.org/10.1073/pnas.1413024112>, 2015.
- 1209 Smith, L. C., Yang, K., Pitcher, L. H., Overstreet, B. T., Chu, V. W., Rennermalm, Å. K., Ryan, J. C., Cooper, M. G., Gleason,
1210 C. J., Tedesco, M., Jeyaratnam, J., As, D. van, Broeke, M. R. van den, Berg, W. J. van de, Noël, B., Langen, P. L., Cullather,
1211 R. I., Zhao, B., Willis, M. J., Hubbard, A., Box, J. E., Jenner, B. A. and Behar, A. E.: Direct measurements of meltwater runoff
1212 on the Greenland ice sheet surface, *PNAS*, 114(50), E10622–E10631, <https://doi.org/10.1073/pnas.1707743114>, 2017.
- 1213 [Smith, L. C., Andrews, L. C., Pitcher, L. H., Overstreet, B. T., Rennermalm, Å. K., Cooper, M. G., Cooley, S. W., Ryan, J. C.,
1214 Miège, C., Kershner, C., and Simpson, C. E.: Supraglacial River Forcing of Subglacial Water Storage and Diurnal Ice Sheet
1215 Motion, 48, e2020GL091418, <https://doi.org/10.1029/2020GL091418>, 2021.](https://doi.org/10.1029/2020GL091418)
1216
- 1217 Spring, U. and Hutter, K.: Numerical studies of Jökulhlaups, *Cold Reg Sci Technol.*, 4(3), 227–244,
1218 [https://doi.org/10.1016/0165-232X\(81\)90006-9](https://doi.org/10.1016/0165-232X(81)90006-9), 1981.
- 1219 Spring, U. and Hutter, K.: Conduit flow of a fluid through its solid phase and its application to intraglacial channel flow, *Int.*
1220 *J. Eng. Sci.*, 20(2), 327–363, [https://doi.org/10.1016/0020-7225\(82\)90029-5](https://doi.org/10.1016/0020-7225(82)90029-5), 1982.
- 1221 Tedstone, A. J., Nienow, P. W., Gourmelen, N., Dehecq, A., Goldberg, D. and Hanna, E.: Decadal slowdown of a land-
1222 terminating sector of the Greenland Ice Sheet despite warming, *Nature*, 526(7575), 692–695,
1223 <https://doi.org/10.1038/nature15722>, 2015.
- 1224 Trunz, C.: Modeling and Measuring Water Level Fluctuations in the Greenland Ice Sheet: How Moulin Life Cycle and Shape
1225 can Inform us on the Subglacial Drainage System, Ph.D., University of Arkansas, Fayetteville, Arkansas, 156 pp., 2021.
- 1226 Turcotte, D. L. and Schubert, G.: *Geodynamics*, Cambridge University Press., 2002.
- 1227 Vaňková, I., Voytenko, D., Nicholls, K. W., Xie, S., Parizek, B. R., and Holland, D. M.: Vertical Structure of Diurnal Englacial
1228 Hydrology Cycle at Helheim Glacier, East Greenland, *Geophys. Res. Lett.*, 45, 8352–8362,
1229 <https://doi.org/10.1029/2018GL077869>, 2018.
- 1230 Vaughan, D. G.: Tidal flexure at ice shelf margins, *J. Geophys. Res. Solid Earth*, 100(B4), 6213–6224,
1231 <https://doi.org/10.1029/94JB02467>, 1995.
- 1232 Weertman, J.: Theory of water-filled crevasses in glaciers applied to vertical magma transport beneath oceanic ridges, *J.*
1233 *Geophys. Res.*, 76, 1171–1183, <https://doi.org/10.1029/JB076i005p01171>, 1971.
- 1234 Weertman, J.: Can a water-filled crevasse reach the bottom surface of a glacier?, *IASH*, 95, 139–145, 1973.

- 1235 Weertman, J.: Dislocation Based Fracture Mechanics, World Scientific Publishing Company, Singapore, 1996.
- 1236 Werder, M. A.: The hydrology of subglacial overdeepenings: A new supercooling threshold formula, *Geophys. Res. Lett.*, 43,
1237 2015GL067542, <https://doi.org/10.1002/2015GL067542>, 2016.
- 1238 Werder, M. A., Schuler, T. V. and Funk, M.: Short term variations of tracer transit speed on alpine glaciers, *TC*, 4(3), 381–
1239 396, 2010.
- 1240 Werder, M. A., Hewitt, I. J., Schoof, C. G. and Flowers, G. E.: Modeling channelized and distributed subglacial drainage in
1241 two dimensions, *J. Geophys. Res. Earth Surf.*, 118(4), 2140–2158, <https://doi.org/10.1002/jgrf.20146>, 2013.
- 1242 Williams, J. J., Gourmelen, N. and Nienow, P.: Dynamic response of the Greenland ice sheet to recent cooling, *Sci. Rep.*,
1243 10(1), 1647, <https://doi.org/10.1038/s41598-020-58355-2>, 2020.
- 1244 Wright, P. J., Harper, J. T., Humphrey, N. F. and Meierbachtol, T. W.: Measured basal water pressure variability of the western
1245 Greenland Ice Sheet: Implications for hydraulic potential, *J. Geophys. Res. Earth Surf.*, 121(6), 2016JF003819,
1246 <https://doi.org/10.1002/2016JF003819>, 2016.
- 1247 Yang, K. and Smith, L. C.: Internally drained catchments dominate supraglacial hydrology of the southwest Greenland Ice
1248 Sheet, *J. Geophys. Res. Earth Surf.*, 2016JF003927, <https://doi.org/10.1002/2016JF003927>, 2016.
- 1249 Yang, K., Smith, L. C., Chu, V. W., Pitcher, L. H., Gleason, C. J., Rennermalm, A. K. and Li, M.: Fluvial morphometry of
1250 supraglacial river networks on the southwest Greenland Ice Sheet, *GISci. Remote Sens.*, 53(4),
1251 <https://doi.org/10.1080/15481603.2016.1162345>, 2016.

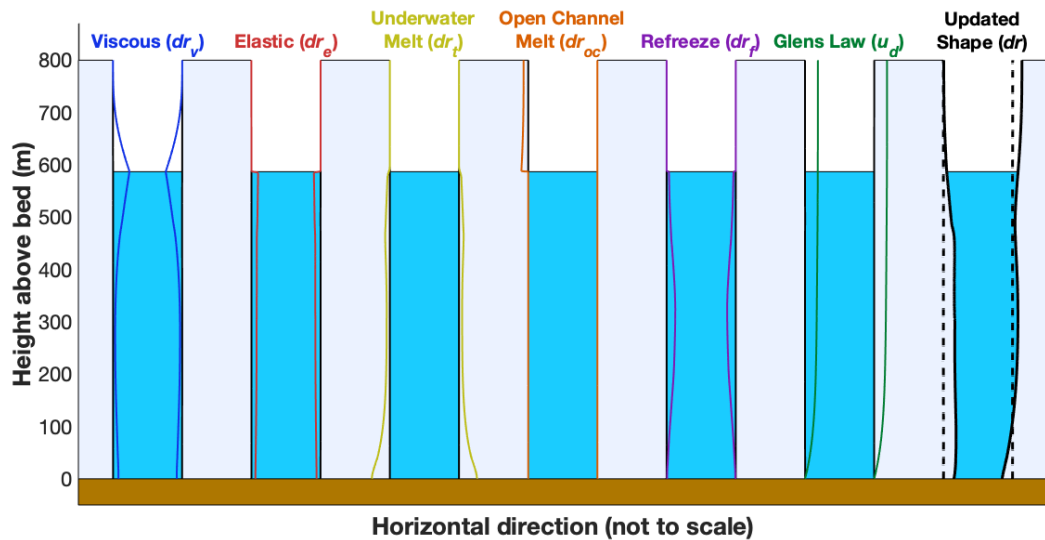
1252

1253

1254



1256



1257

1258 **Figure 1. Processes included in the MouSh model.** Black lines show a base moulin geometry that each process acts on, and colored lines
 1259 show the change in moulin geometry (not to scale) due to that process alone. From left to right: changes in moulin geometry due to viscous
 1260 deformation; elastic deformation; melting by turbulent energy dissipation of flowing water inside the moulin; melting by open-channel water
 1261 flow along bare ice; refreezing over winter inside the moulin; and deformation due to ice motion prescribed by Glen’s flow law. Unlike the
 1262 other components, elastic deformation is instantaneous, but applied over the model timestep (Sect. 2.2.1; Supplement [S2S1](#)). The right-most

1263 moulin shows the moulin geometry before (dashed black lines) and after (solid black lines and blue water) aseveral hypothetical model
 1264 timesteptimesteps, i.e., the sum of all processes shown in the preceding panels. Changes are not to scale.

1265 Figure

1266

1267

1268

1269

1270

1271

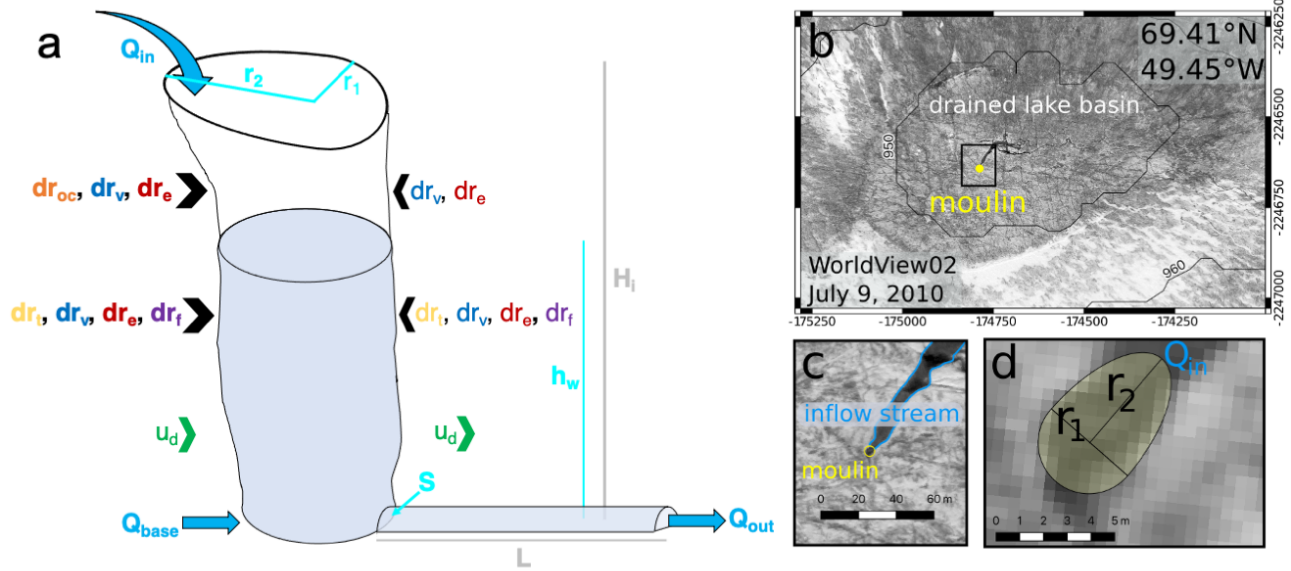
1272

1273

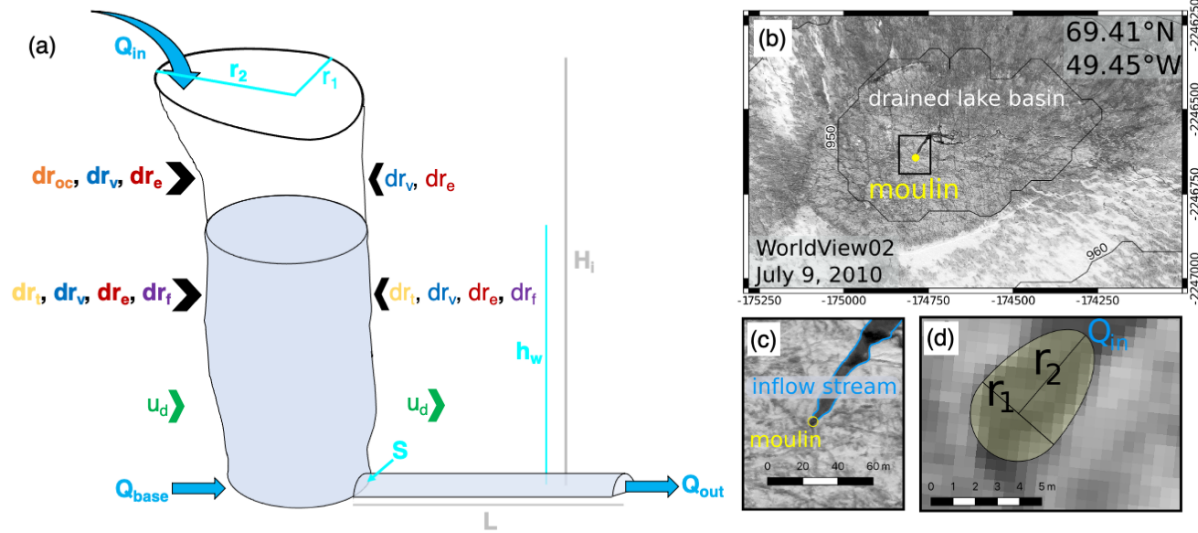
1274

1275

1276 FIGURE 2



1277



1278
 1279 **Figure 2. MouSh geometry and surface expression of a moulin and its reflection in the MouSh model.** (a) Schematic of MouSh
 1280 geometry and inputs. Inflow and outflow of the system are indicated by Q_{in} , Q_{out} , and Q_{base} . Time evolving moulin and subglacial parameters
 1281 include moulin radii (r_1 , r_2), moulin water level (h_w), and subglacial cross-sectional area (S). r_1 and r_2 are evolved by dr_{oc} , dr_v , dr_e , dr_f , and
 1282 dr_i (open channel melting, viscous deformation, elastic deformation, refreezing, and turbulent melting, respectively; colored as in Fig. 1). u_d
 1283 shears the moulin as prescribed by Glen's Flow Law. Ice thickness and subglacial path length are indicated by H_i and L , respectively. Ice
 1284 flow is from left to right. ~~Further details are in Sect. 2.~~ Modified from Trunz (2021). (b) WorldView-2 scene from July 2010 of an
 1285 approximately 1.2×0.8 km region surrounding the example moulin (yellow) formed by a drained supraglacial lake. (c) Detail of panel b,
 1286 with the inflow stream and moulin indicated. (d) Detail of panel c, showing the moulin minor radius r_1 , major radius r_2 , and water input Q_{in}
 1287 from the inflow stream, as represented in the MouSh model. Maps generated by authors. WorldView image © 2010 DigitalGlobe, Inc.

1288 **Figure**

1289

1290

1291

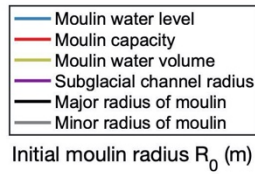
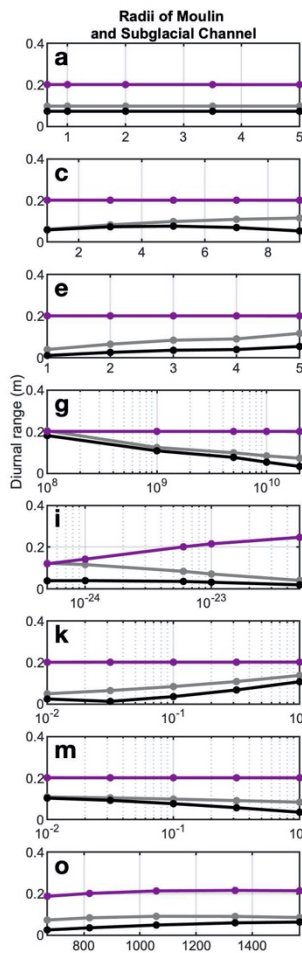
1292

1293

1294

1295

1296 **FIGURE 3**



Initial moulin radius R_0 (m)

Ice enhancement factor F_e

Ice temperature scenario T

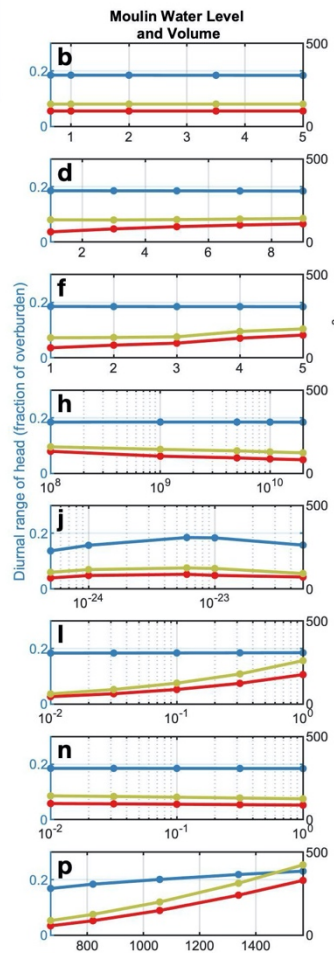
Shear modulus E (Pa)

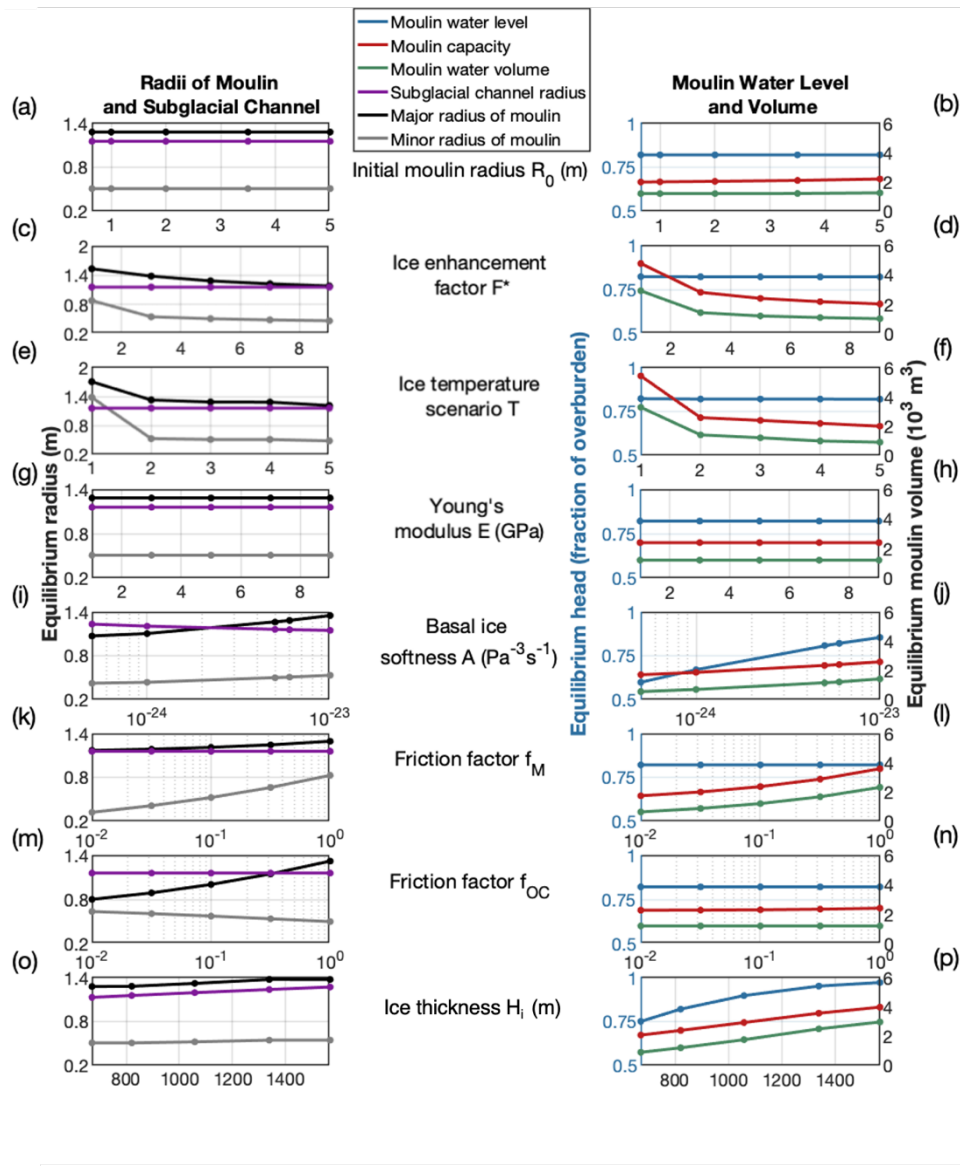
Basal ice softness A ($\text{Pa}^{-3}\text{s}^{-1}$)

Friction factor f_m

Friction factor f_{oc}

Ice thickness H_i (m)

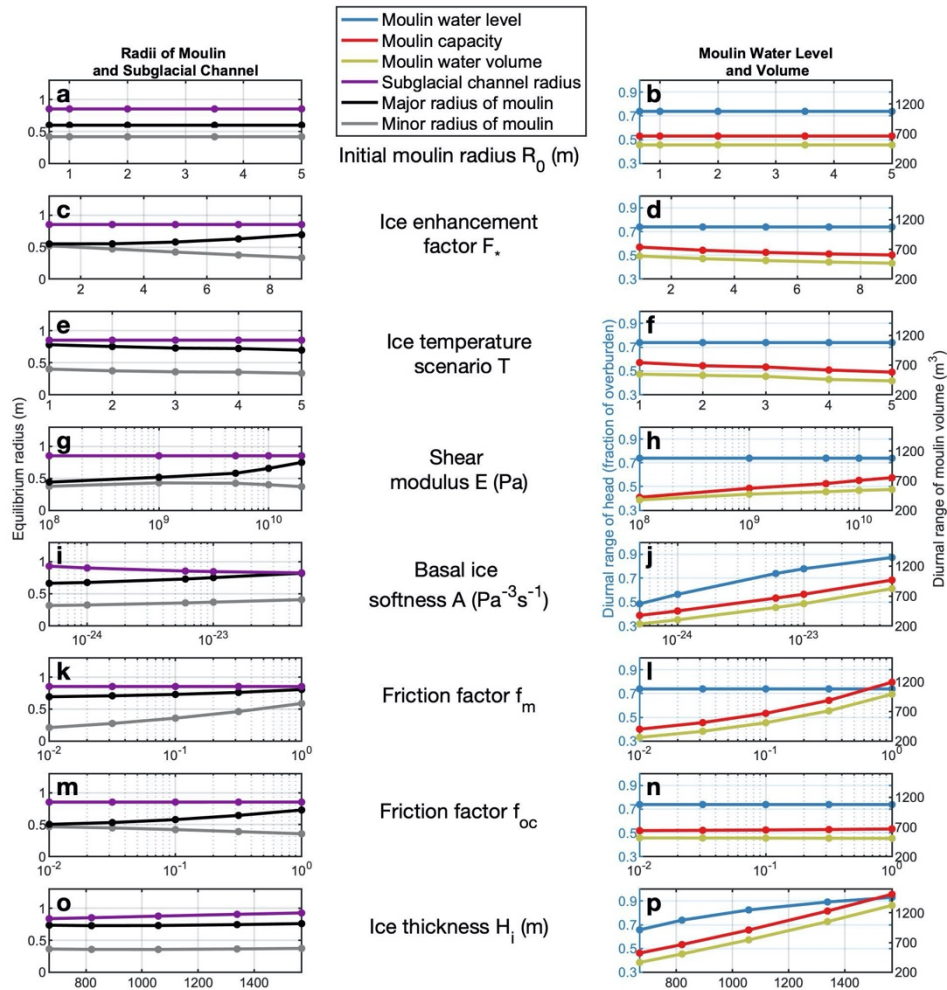


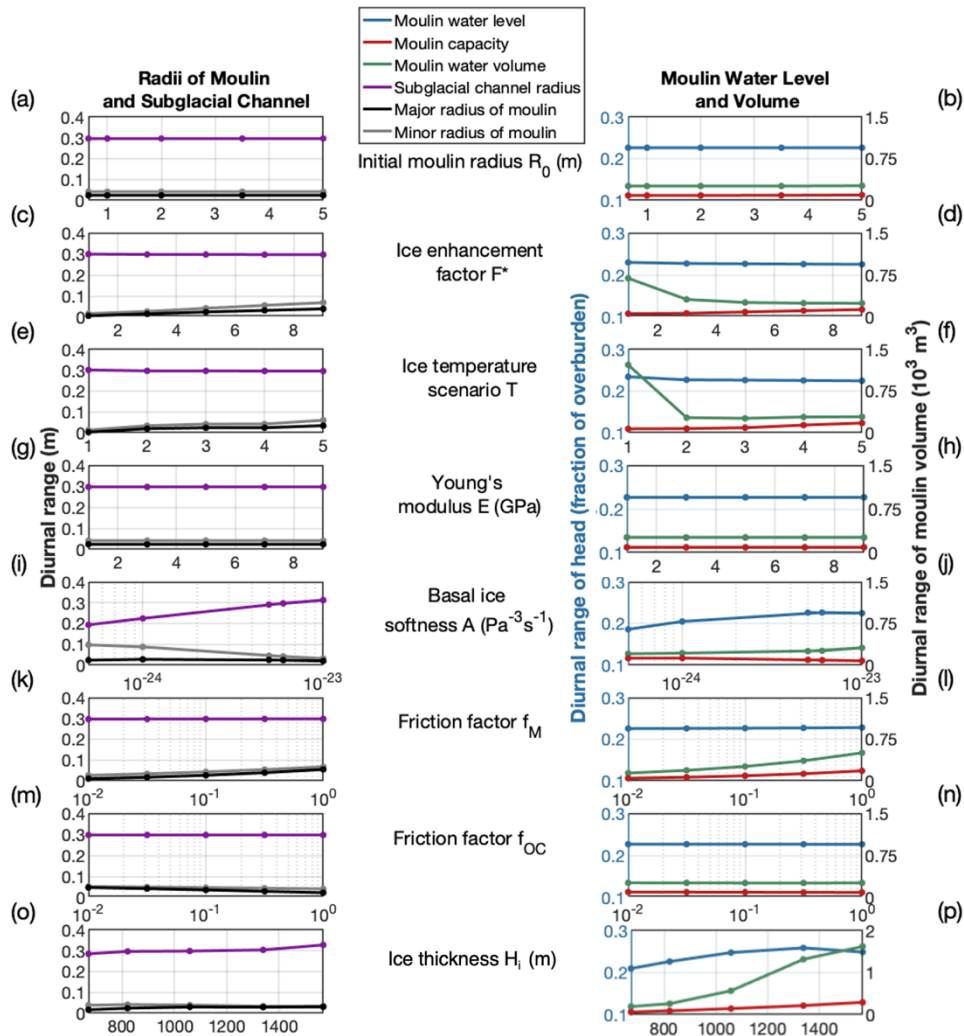


1298

1299 **Figure 3. Results of parameter sensitivity studies for 1040-day MouSh model runs.** Shown are the sensitivity of moulin size to initial
 1300 condition for moulin radius (a–b), enhancement factor for englacial ice (c–d), ice temperature scenario (e–f), Young's modulus (g–h), softness
 1301 of basal ice (i–j), friction factor for water flow beneath the water line (k–l), friction factor for water flow above the water line (m–n), and ice
 1302 thickness (o–p). The left column shows the moulin radii (black and grey) at the mean water level and the mean subglacial channel radius
 1303 (purple) averaged over the final 24-hour period of the 1040-day model run. The right column shows the equilibrium water level (blue),
 1304 moulin volume capacity (red), and volume of water in the moulin (green) averaged over the same 24-hour period. Overall, moulin radius
 1305 is most sensitive to the friction factors, while moulin water level and volume are most sensitive to ice thickness H_i (also an indicator of the
 1306 hydraulic potential gradient) and basal ice softness A . Note the different y-axis range in panels (c) and (e).

1307





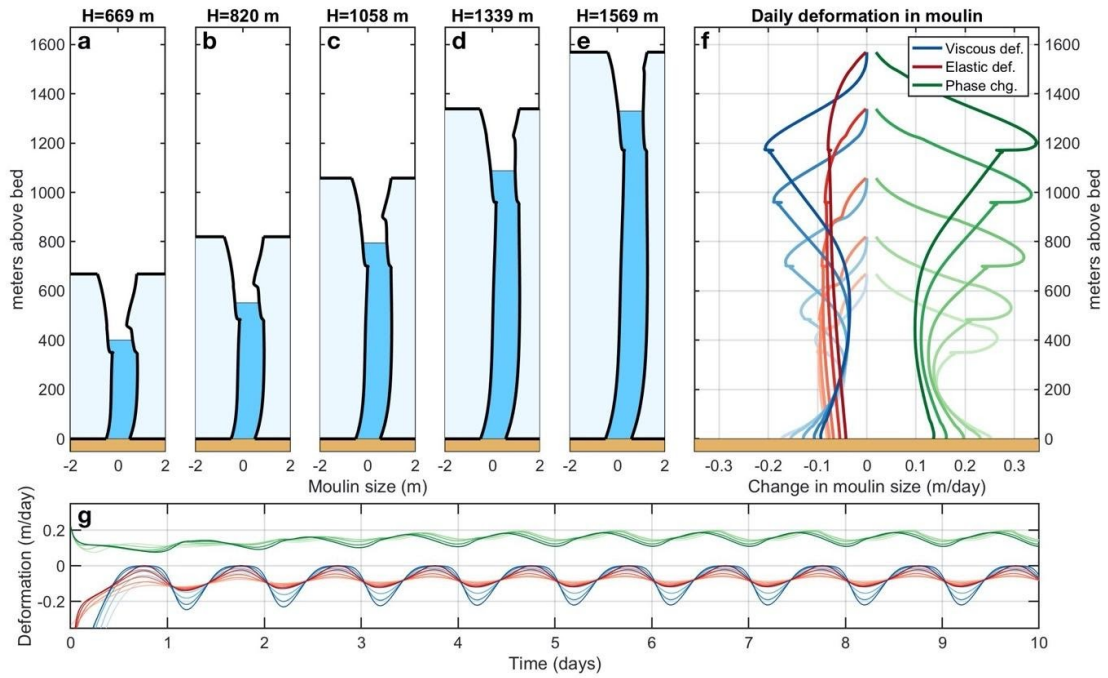
1311

1312 **Figure 4. Diurnal variations in moulin sizes in 1040-day parameter sensitivity runs.** Shown are the sensitivity of diurnal variation in
 1313 moulin size and water storage metrics to initial condition for moulin radius (a–b), enhancement factor for englacial ice (c–d), ice temperature
 1314 scenario from coldest to warmest ice (e–f), Young's modulus (g–h), softness of basal ice (i–j), friction factor for water flow beneath the water
 1315 line (k–l), friction factor for water flow above the water line (m–n), and ice thickness (o–p). The left column shows diurnal variations in
 1316 moulin radii (black and grey) at the equilibrium water level and the subglacial channel radius (purple) in the final 24-hour period of the
 1317 ten40-day model run. The right column shows the diurnal variation in water level (blue), moulin volume (red), and volume of water in the
 1318 moulin (goldgreen) within the same 24-hour period. *Note the right y-axis difference in panel (p).*

1319

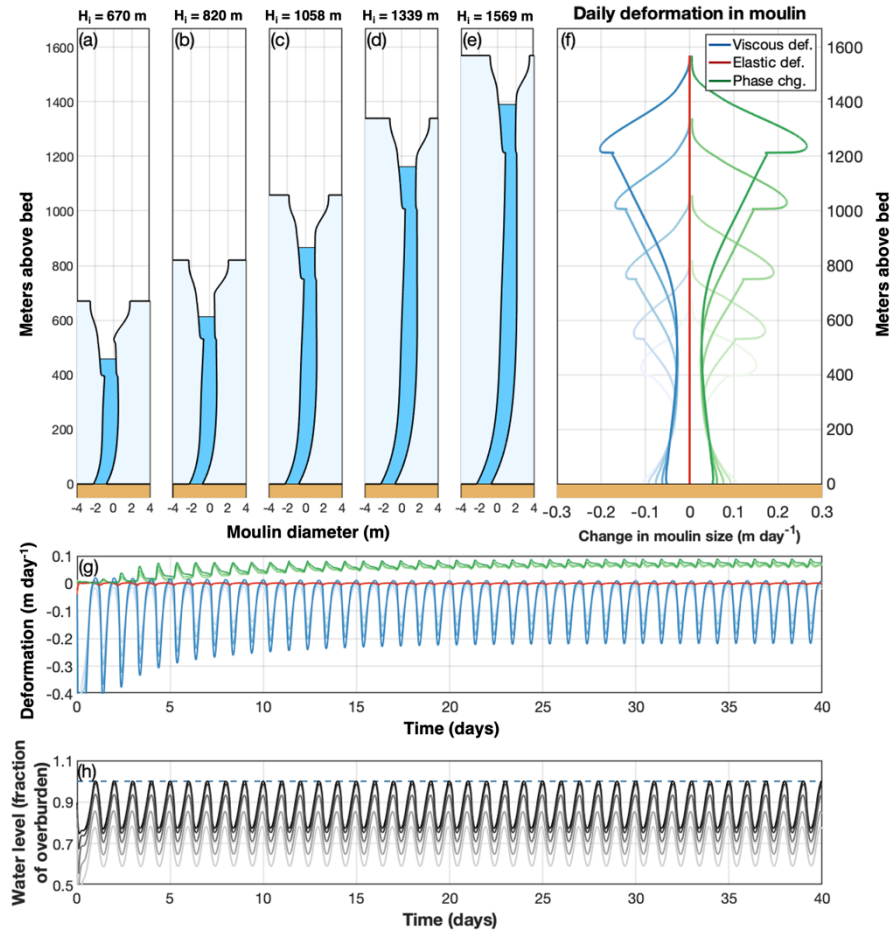
1320 **Figure**

1321 **FIGURE 5**



1322

1323



1324

1325 **Figure 5. Contributions of viscous deformation, elastic deformation, and phase changes to moulin geometry.** (a–e) Equilibrium
 1326 geometries of five moulins in ice of different ice thicknesses H_i and different distances from the terminus (same as Fig. 6o–p) averaged over
 1327 the final 24-hour period of a 1040-day model run. (f) Vertical variation of viscous deformation (blue), elastic deformation (red), and phase
 1328 change (green) contributions to moulin geometry averaged over the same 24-hour period. Negative values indicate contributions to moulin
 1329 closure; positive values open the moulin. Darkening shades of each color map to moulins of increasing ice thickness. Closure and opening
 1330 rates are greatest at the minimum daily water level (which is inferable by the lower notch in the moulin wall). (g) Time series of the
 1331 components shown in panel f (colors the same) at the mean water level over the entire 1040-day model run. The greater diurnal range in
 1332 water level in moulins in thick ice drives the observed larger diurnal variations in viscous and elastic deformation. (h) For
 1333 reference, moulin water level as fraction of overburden for different ice thicknesses H_i . Lighter greys indicate thinner ice; blue dashed line
 1334 indicates where fraction of overburden = 1.

1335

1336

1337

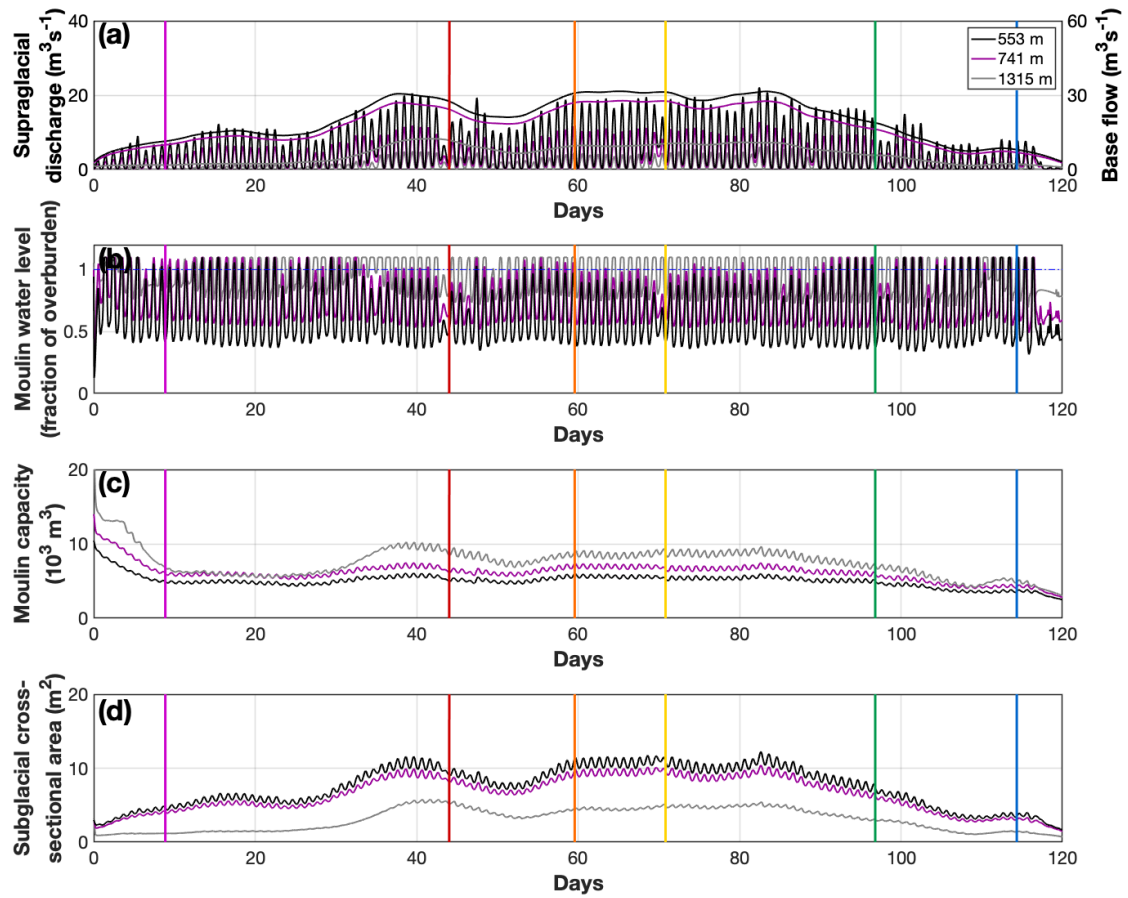
1338

1339

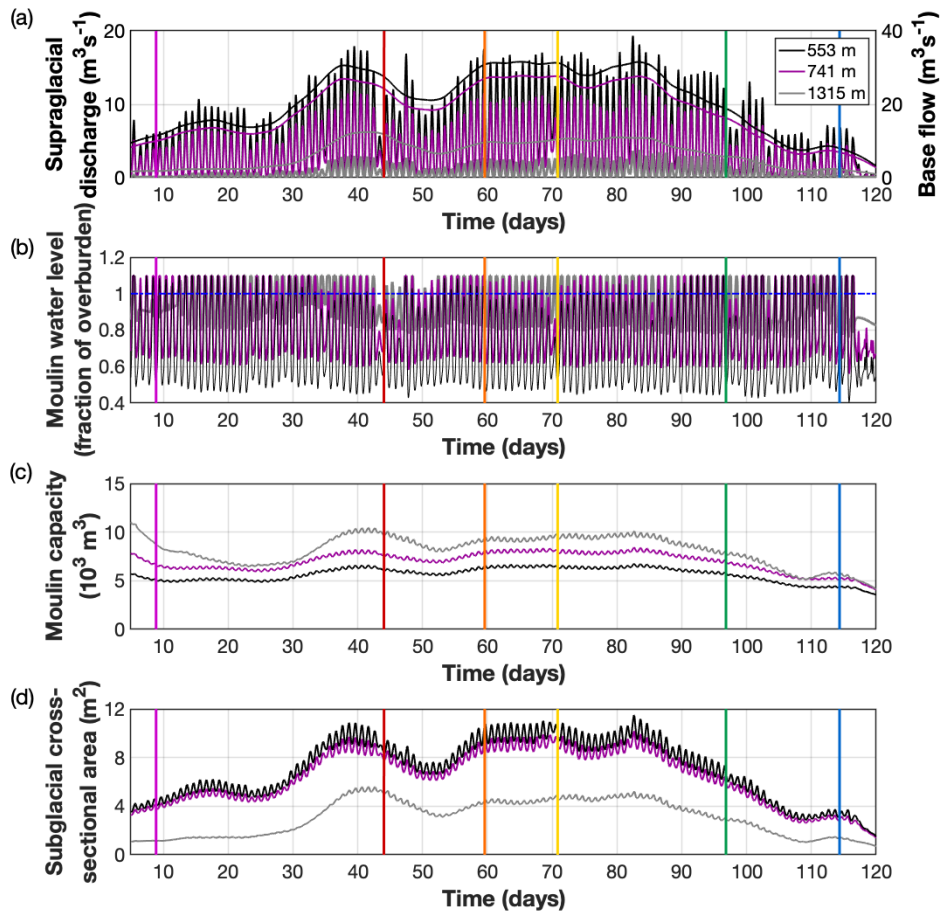
1340

1341

1342 **Figure** **FIGURE** 6



1343



1344

1345 **Figure 6. MouSh model runs with realistic supraglacial and ice conditions.** The model runs are for a low-elevation [basinBasin_1](#) (553 m
 1346 ice thickness; black lines), mid-elevation [basinBasin_2](#) (741 m ice thickness; purple lines), and high-elevation [basinBasin_3](#) (1315 m ice
 1347 thickness; grey lines). (a) Supraglacial discharge into the moulin Q_{in} and prescribed base flow Q_{base} . (b) Moulin water level as a fraction of
 1348 overburden. Note that the highest elevation moulin exceeds the ice surface most days. (c) Moulin capacity, or the total moulin volume. (d)
 1349 Subglacial channel cross-sectional area. Colored vertical lines indicate times in Fig. 7. Note x-axes start on day 5.

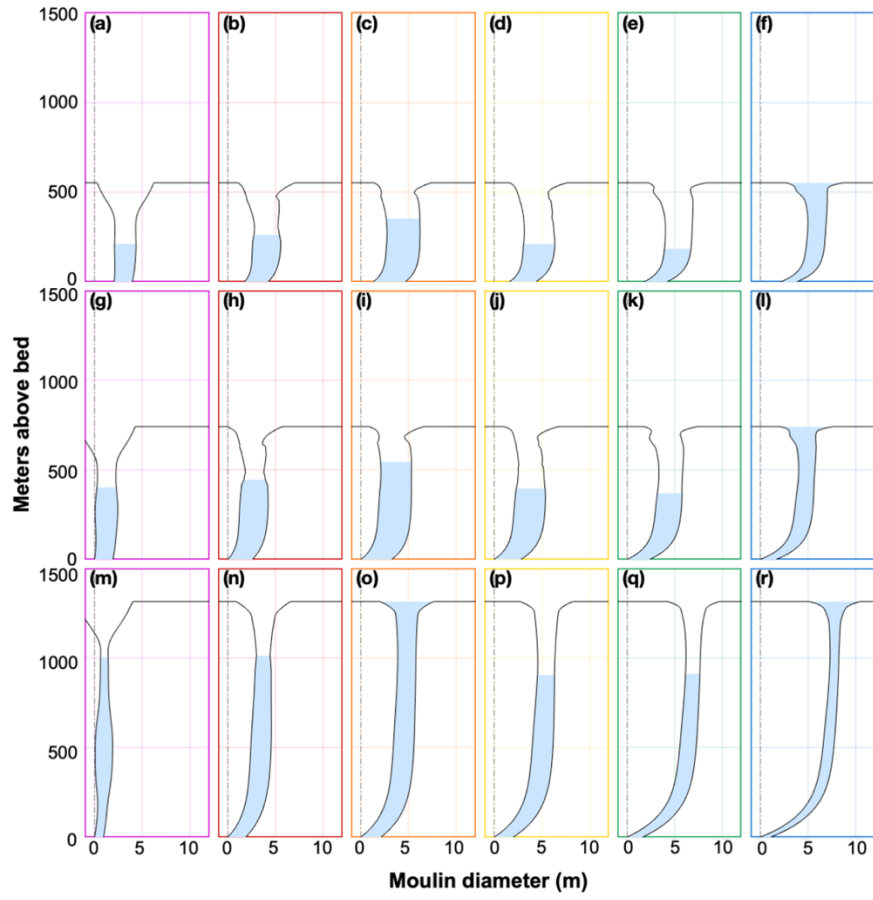
1350

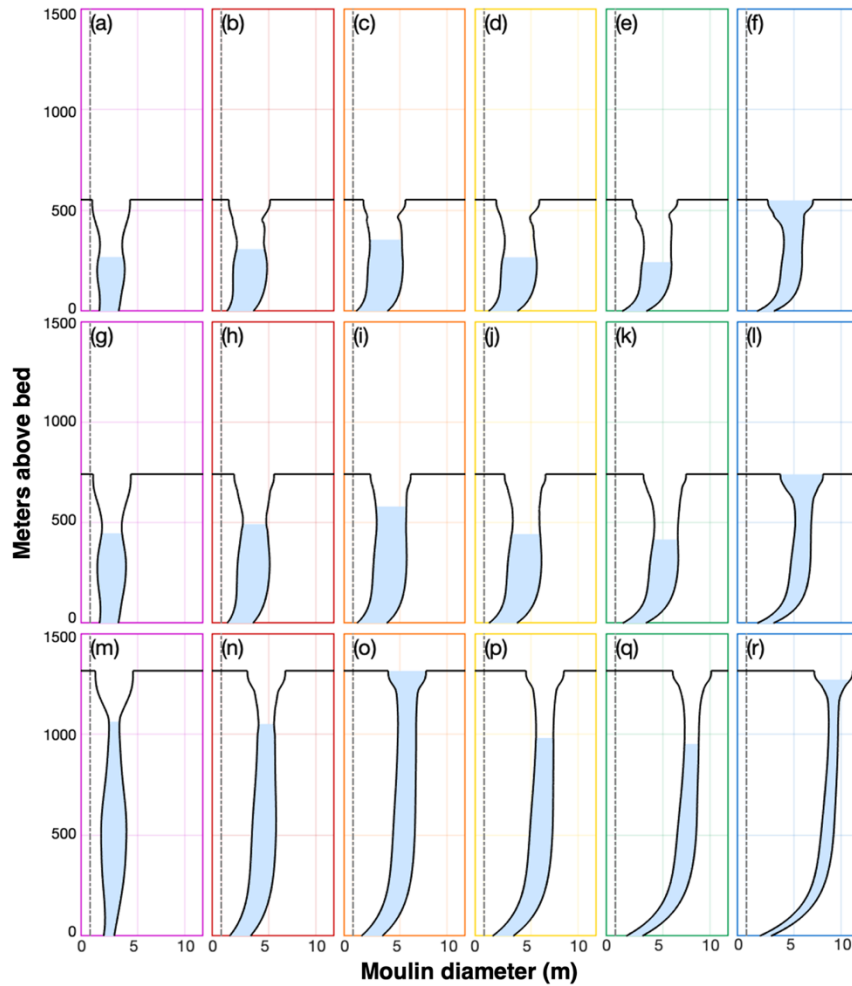
1351

1352

1353

1354





1357

1358 **Figure 7. Evolution of moulin geometry over the melt season.** Colored boxes correspond to the times indicated with colored vertical lines

1359 in Fig. 6. (a–f) Basin 1 with ice thickness of 553 m. (g–l) Basin 2 with ice thickness of 741 m. (m–r) Basin 3 with ice thickness of 1315 m.

1360 Axes are not to scale.

1361

1362

1363

1364

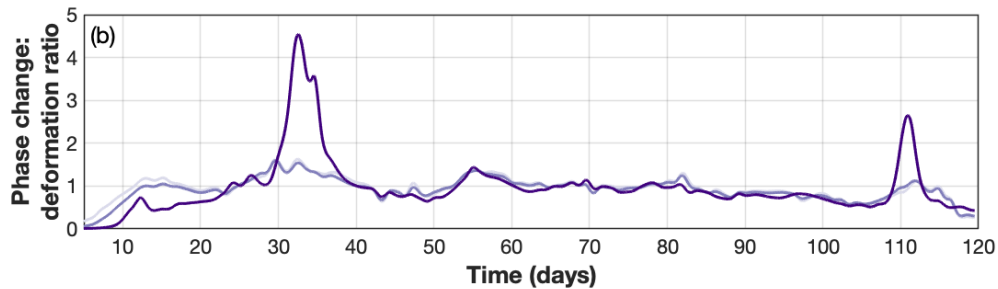
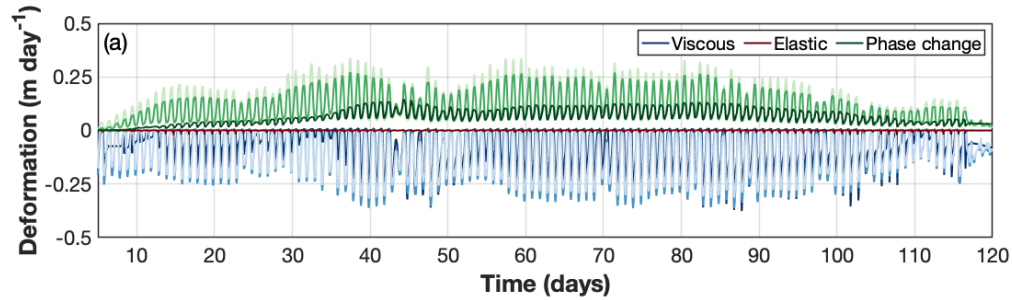
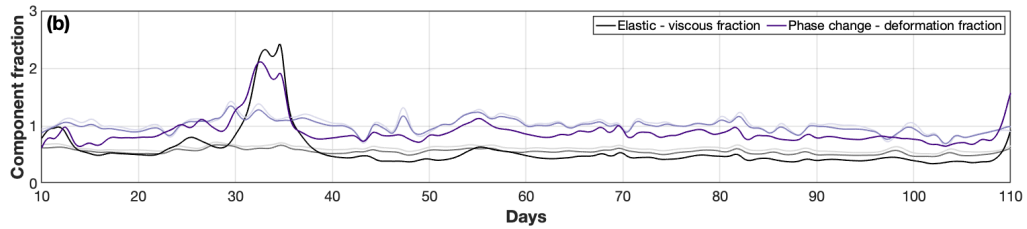
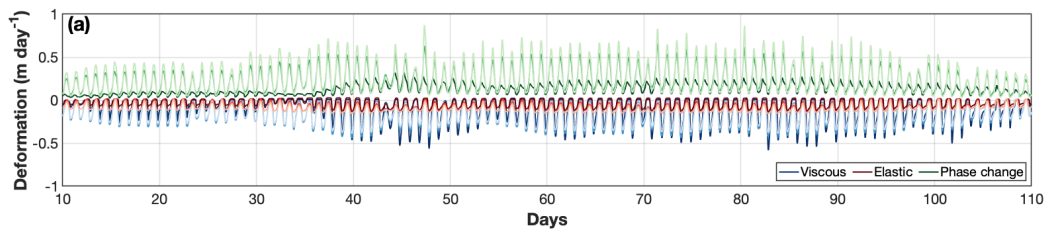
1365

1366

1367

1368 **Figure**

1369 **FIGURE 8**



1370

1371

1372 **Figure 8. Time series of viscous, elastic and phase change components of moulin evolution and their relative importance in**
 1373 **determining moulin geometry. (a) Time varying viscous (blues), elastic (reds), and phase change (melting, greens) components of moulin**
 1374 **geometry. (b) The ratio of elastic to viscous deformation (greys) indicates the relative importance of the two deformational processes in**
 1375 **moulin evolution. All values are lower than 1, indicating that viscous deformation is always greater. The (b) The daily ratio of the total**
 1376 **amount of phase change (melting above and below the water line) to total deformation (elastic plus viscous; purples). Values above 1 indicate**
 1377 **that melting dominates; values below 1 indicate that deformation dominates. Data is smoothed over 24 h. For both panels, light colors are**
 1378 **for Basin 1 ($H_i=553$ m), medium colors for Basin 2 ($H_i=741$ m), and dark colors for Basin 3 ($H_i=1315$ m). Note x-axes start on day 5.**

1379

1380

1381

1382

1383

1384

1385

1386

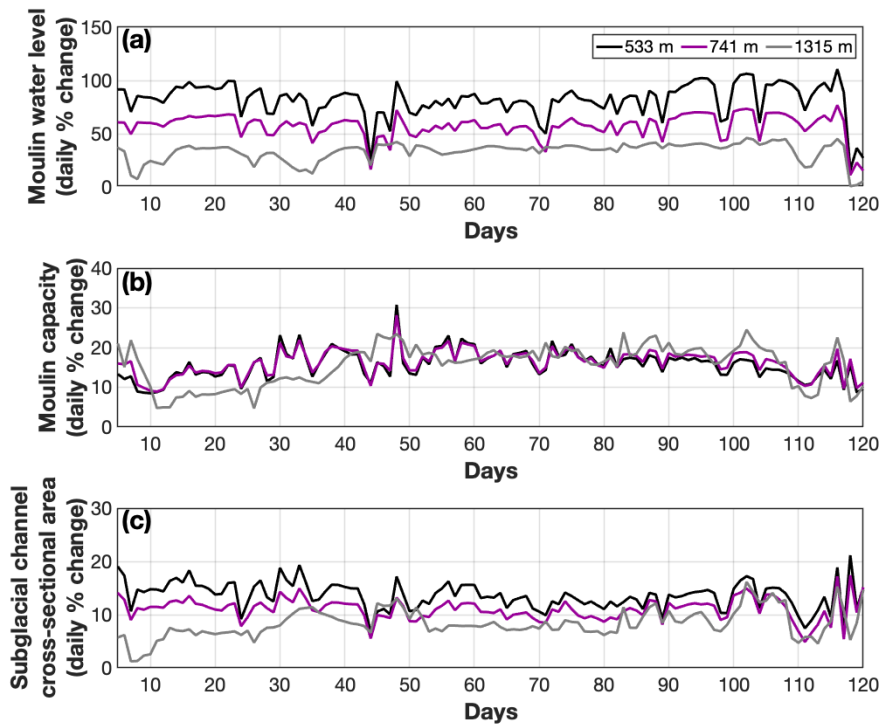
1387

1388

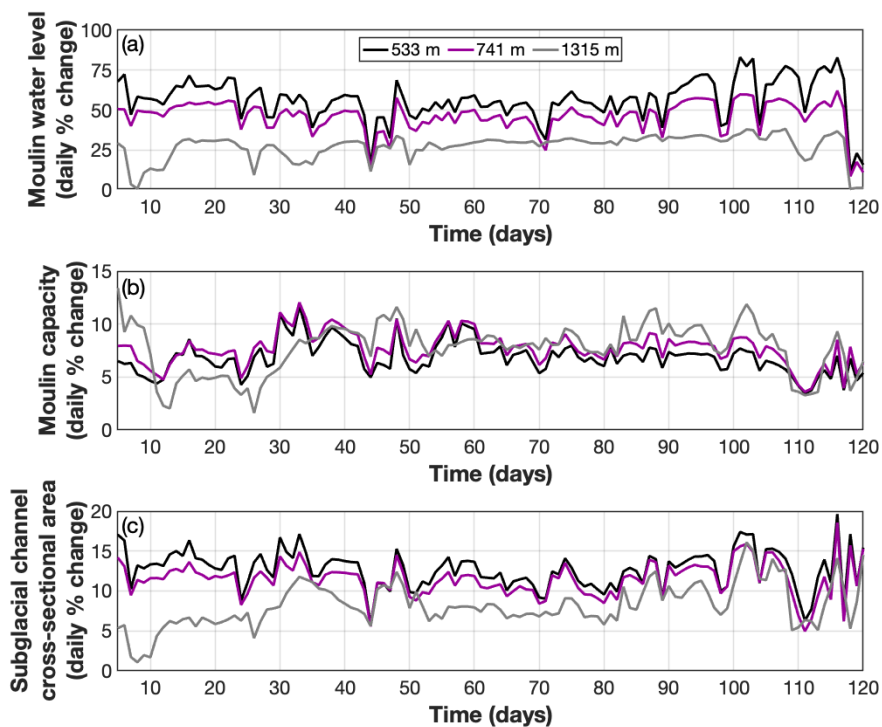
1389

1390

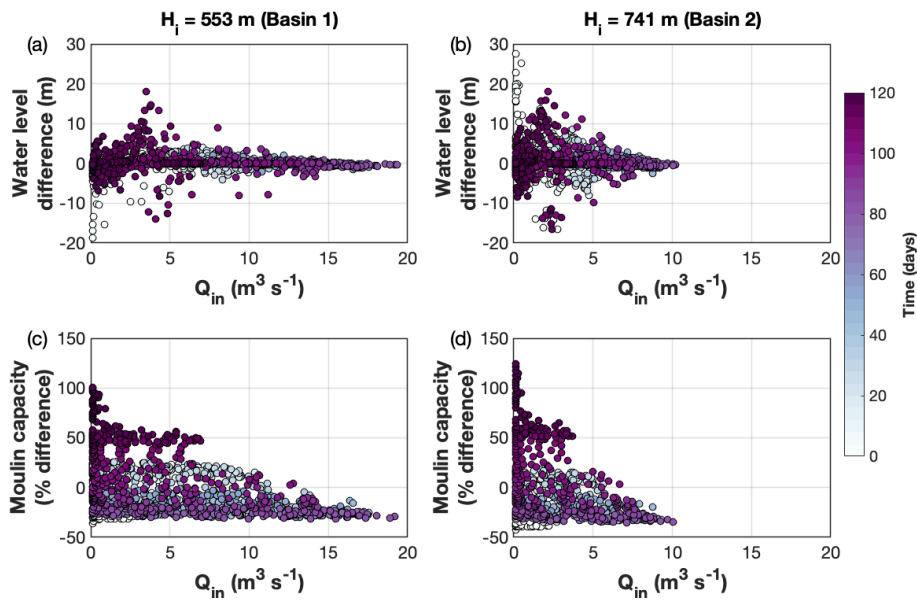
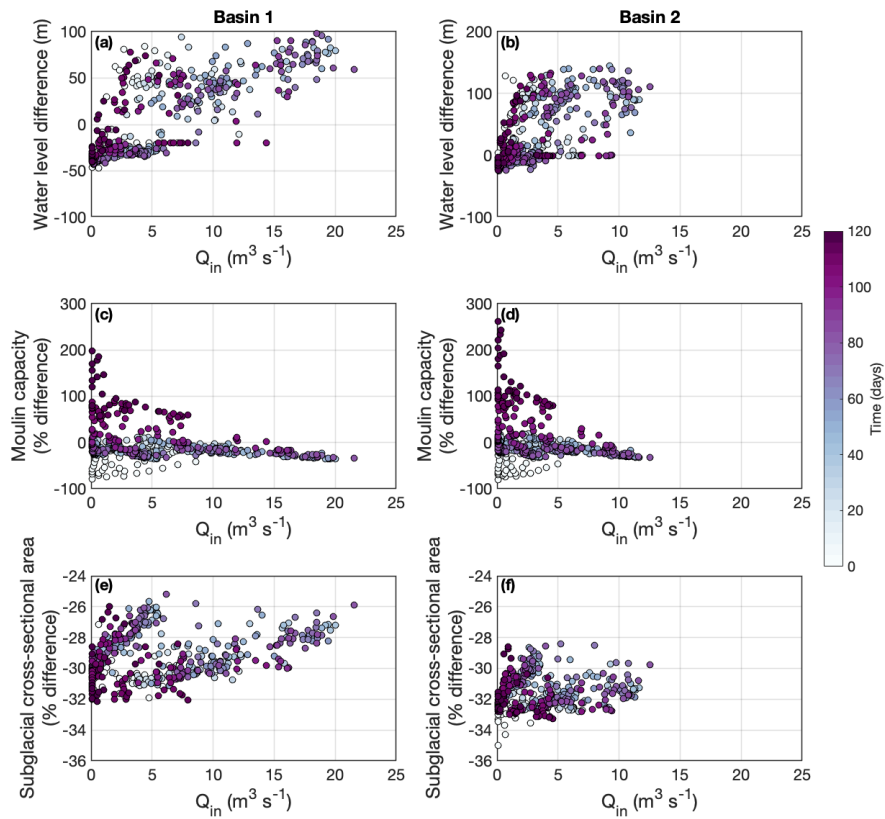
1391 ~~Figure~~ FIGURE 9



1392



1395 **Figure 9. Daily percentage change in moulin variables relative to the daily mean value.** (a) Daily percentage change in moulin water
 1396 level relative to the daily mean water level for Basins 1, 2, and 3 (black, purple, and grey lines, respectively). (b) Daily percentage change
 1397 in moulin capacity relative to the daily mean moulin capacity. (c) Daily percentage change in the subglacial channel cross-sectional area
 1398 relative to the daily mean value. For (b–c), colors are as in (a).



1408

1409

1410 **Figure 10. Difference between variable and fixed moulin geometries for Basin 1 and 2** (ice thicknesses of 553 m and 741 m,
1411 respectively). The fixed moulins are cylinders with a fixed radius of 1.6 and 1.4 m (for Basin 1) and 2 m (Basin 2), respectively, which are
1412 the time-mean radii at the equilibrium mean water level for the variable moulins. In all instances, the difference is calculated as
1413 $(cylindrical - variable)$ with instances of percentage difference calculated as $(cylindrical - variable) / (variable)$. (a, b) Difference in moulin
1414 water level for Basin 1 (black) and Basin 2 (purple), respectively, plotted every hour. Negative values indicate periods where the variable
1415 moulin water levels are higher than those of the fixed cylindrical moulin. (c, d) Percentage difference in moulin capacity, plotted every 2
1416 hours for clarity. When values are negative, the variable moulin is larger than the fixed cylindrical moulin. (e, f) Percentage difference in
1417 subglacial channel cross-sectional area. These values are persistently negative, indicating that the subglacial channel is larger with a variable
1418 moulin.
1419

1420

1421

1422

1423

1424

1425 **Table 1. MouSh model constants and parameter ranges.** During realistic runs (Sect. 2.4) Median values were 2.5.3) Values
 1426 used during realistic model experiments are generally used. In instances where values used differ from the median value, of
 1427 the values used is indicated in parentheses. sensitivity experiment.

Constant		Value	Units	
ρ_i	Ice density	910	kg m ⁻³	
ρ_w	Water density	1000	kg m ⁻³	
g	Gravitational acceleration	9.81	m s ⁻²	
L_f	Latent heat of fusion	335000	J kg ⁻¹	
M_w	Dynamic viscosity (liquid water)	0.0017916	Pa s	
K_w	Thermal conductivity (liquid water)	0.555	J (m K s) ⁻¹	
C_w	Heat capacity (liquid water)	4210	J (K kg) ⁻¹	
C_i	Heat capacity (ice)	2115	J (K kg) ⁻¹	
Parameter		Median value	Range	Units
R_0	Initial moulin radius	2.4 (3)	0.5 to 5	m
E	Ice deformation enhancement factor	5	1 to 9	-
$T(z)$	Ice temperature	-6 (FOXX profile)	-23 to 0	°C
Ψ	Young's modulus	5 (9)	1 to 9	GPa
A	Basal ice softness	6×10^{-24}	5×10^{-25} to 5×10^{-23}	Pa ⁻³ s ⁻¹
f_M	Friction factor (under water)	0.1	0.01 to 1	-
f_{OC}	Friction factor (subaerial / open channel)	1 (0.8)	0.01 to 1	-
H	Ice thickness	1058 (553, 741, 1315)	669 to 1569	m

Constant	Description	Value	Units	
ρ_i	Ice density	910	kg m ⁻³	
ρ_w	Water density	1000	kg m ⁻³	
ν	Poisson's ratio	0.3	-	
C_p	Heat capacity (ice)	2115	J (K kg) ⁻¹	
C_w	Heat capacity (liquid water)	4210	J (K kg) ⁻¹	
g	Gravitational acceleration	9.81	m s ⁻²	
K_i	Thermal conductivity (ice)	2.1	J (m K s) ⁻¹	
K_w	Thermal conductivity (liquid water)	0.555	J (m K s) ⁻¹	
L_f	Latent heat of fusion	335000	J kg ⁻¹	
Parameter	Description	Realistic run value	Range	Units
A	A	<i>T_i & F* dependent</i>		Pa ⁻³ s ⁻¹
	A_{sub}	6 x 10 ⁻²⁴	5 x 10 ⁻²⁵ to 5 x 10 ⁻²³	
E	Young's modulus	5	1 to 9	GPa
F *	Ice deformation enhancement factor	5	1 to 9	-
f	f_{oc}	0.1	0.01 to 1	-
	f_m	0.8	0.01 to 1	
H_i	Ice thickness*	553, 741, 1315	669 to 1569	m
n	Glen's Flow Law exponent	3	-	-
R_0	Initial moulin radius	2	0.5 to 5	m
$T_i(z)$	Ice temperature	-6 (FOXX profile)	-23 to 0 **	°C

* H_i defines distance from terminus L and surface slope a based on a perfectly plastic ice surface profile

**including Iken et al. (1993), Lüthi et al. (2015), and Ryser et al. (2014)

1428

1429

1430

1431 **Table 2. General ice and moulin input parameters for realistic runs**

Parameter	Basin 1	Basin 2	Basin 3
Ice thickness (m)	553	741	1315
Distance from terminus (km)	13.6	24.5	77.1
Catchment size (km ²)	19.8	18.4	55.5
Moulin input, mean diurnal range (m·s ⁻³)	11.5	6.7	2.5
Moulin input, maximum value (m·s ⁻³)	22.4 19.3	12.8	6.3 8
Baseflow, mean value (m·s ⁻³)	20.2	21.2 17.7	6.2

1432

Elastic deformation around a cylindrical hole in ice

Supplement **S1** for “Controls on Greenland moulin geometry and evolution from the Moulin Shape model”, *The Cryosphere*.

Contents

S1.1	Introduction	1
S1.2	Aadnøy’s setup and stress solutions	2
S1.2.1	Assumptions	2
S1.2.2	Solution	2
S1.3	Integrated elastic deformation	3
S1.4	Simplest case: Non-varying deviatoric and shear stresses	5
S1.5	Instantaneous elastic deformation and calculated deformation rates	5

S1.1 Introduction

Here we describe the derivation of the elastic deformation component of the MouSh model. It is based on Aadnøy [1987].

Bernt Aadnøy, a petroleum engineer, derived expressions for the stresses surrounding a borehole (wellbore) through competent rock [Aadnøy, 1987]. He applied the Kirsch [1898] solutions for a circular hole in a plate, stacking many plates to achieve a borehole. He derives an analytic solution for the stress field near a cylindrical borehole through a uniform, solid (non-porous) medium. From the stress solution, we derive the resulting strains using an elastic constitutive relation (Hooke’s Law) and integrate the strains to get the total elastic deformation at the borehole wall. We take this borehole through rock as a direct analogue to a moulin through ice.

We treat the moulin as a stack of independent plates, each with a hole in them, of radius a . The radius of the hole in each plate (equivalently, at each elevation z) is independent of the radius in the plate above and below, but generally, $a(z)$ is smoothly varying because the forces at each z are smoothly varying.

S1.2 Aadnøy's setup and stress solutions

Aadnøy [1987] finds the stress field around a borehole by summing the independent stress contributions from three sources: hydrostatic stress ($P = P_w - P_i = \rho_w g(h_w - z) - \rho_i g(H_i - z)$), deviatoric stresses (σ_x and σ_y), and shear stress (τ_{xy}). The sign of the pressure P is “positive outward”, i.e., net water pressure ($P_w > P_i$) opens the moulin and net ice pressure ($P_i > P_w$) closes the moulin.

S1.2.1 Assumptions

The Aadnøy [1987] solution is based on the Kirsch [1898] equations, which describe the stresses around a hole when the rock is subject to deviatoric stress in one direction, but elaborates from them by adding a second deviatoric stress, a shear stress, and pressure. The Kirsch [1898] and Aadnøy [1987] equations assume that the rock (ice) is a competent linear elastic material. The Kirsch [1898] solution is appropriate for a material stressed below its elastic limit, or roughly one half its compressive strength [Goodman, 1989]. The compressive strength of ice is 3–10 MPa [Fransson, 2009], making the elastic limit 1–5 MPa. This is equivalent to the cryostatic pressure in an empty borehole in ice 100–500 m thick, or the cryo/hydrostatic pressure in a borehole in ice 1–6 km thick that is water-filled to flotation. Because moulin water levels are typically $> \sim 50\%$ the flotation level and ice thicknesses are of order ~ 100 –1000 m, moulins meet these requirements. We note that toward the beginning or end of the melt season (when water levels are lowest), and in thick ice ($> \sim 1000$ m), the ice surrounding the moulin likely approaches or may exceed the elastic limit.

Aadnøy [1987] assumes plane strain in z , i.e., $\epsilon_z = 0$ (no vertical deformation anywhere). This is consistent with the assumptions of our overall MouSh model and is the most basic formulation in solid mechanics. The total absence of vertical deformation in the face of finite horizontal deformation can be accommodated by an effective infinite domain in the cross-sectional plane of the moulin (xy). We happen to make this assumption anyway by summing elastic deformation from the point at infinity to the moulin wall (Sect. S1.3).

Alternately, Aadnøy [1987] also presents a plane stress solution. Plane strain is appropriate for thin plates with free surfaces (the top and bottom, z -facing surfaces), which differs from our “stack of plates” domain because our stacked plates have no free surfaces (excepting the topmost and bottommost plates). Aadnøy [1987]’s plane stress solution differs by a factor of $\frac{1+\nu}{1+\nu+\nu^2}$ from the plane strain solution [Goodman, 1989]; for $\nu = 0.3$, this is a change of 7%. The difference is small and plane stress is a less appropriate formulation than plane strain.

S1.2.2 Solution

The Aadnøy [1987] solution is in cylindrical coordinates (r, θ, z). The radius of the hole is a . Figure S1 shows the problem geometry.

The Kirsch [1898] equations for stresses around a hole in an infinite plate made of an elastic material are as follows:

$$\begin{aligned}
\sigma_r &= \frac{\Delta\sigma_x + \Delta\sigma_y}{2} \left(1 - \frac{a^2}{r^2}\right) + \frac{\Delta\sigma_x - \Delta\sigma_y}{2} \left(1 + \frac{3a^4}{r^4} - \frac{4a^2}{r^2}\right) \cos 2\theta + \Delta\tau_{xy} \left(1 + \frac{3a^4}{r^4} - \frac{4a^2}{r^2}\right) \sin 2\theta + \frac{a^2}{r^2} \Delta P \\
\sigma_\theta &= \frac{\Delta\sigma_x + \Delta\sigma_y}{2} \left(1 + \frac{a^2}{r^2}\right) - \frac{\Delta\sigma_x - \Delta\sigma_y}{2} \left(1 + \frac{3a^4}{r^4}\right) \cos 2\theta - \Delta\tau_{xy} \left(1 + \frac{3a^4}{r^4}\right) \sin 2\theta - \frac{a^2}{r^2} \Delta P \\
\sigma_z &= \Delta\sigma_{zz} - 2\nu(\Delta\sigma_x - \Delta\sigma_y) \frac{a^2}{r^2} \cos 2\theta - 4\nu\Delta\tau_{xy} \frac{a^2}{r^2} \sin 2\theta
\end{aligned} \tag{S1}$$

Here, ΔP is the change in pressure around the borehole. In the rock mechanics example, ΔP is equivalent to P , the pressure, because it assumes the borehole was recently drilled. For the moulin case, where the water level fluctuates by the minute, ΔP is the change in pressure over the time interval in question. The same applies to the deviatoric stresses $\Delta\sigma_x$ and $\Delta\sigma_y$ and the shear stress $\Delta\tau_{xy}$: these are changes in the stress field over a time interval.

Applying Hooke's Law to these equations yields the corresponding strain at any point in the domain. Hooke's Law is just a linear combination of the three stresses in Eqn. S1:

$$\begin{aligned}
\epsilon_r &= E^{-1} (\sigma_r - \nu(\sigma_\theta + \sigma_z)) \\
\epsilon_\theta &= E^{-1} (\sigma_\theta - \nu(\sigma_r + \sigma_z)) \\
\epsilon_z &= E^{-1} (\sigma_z - \nu(\sigma_r + \sigma_\theta))
\end{aligned} \tag{S2}$$

where E is Young's modulus (~ 1 GPa) and ν is Poisson's ratio (~ 0.3 for ice; unitless).

S1.3 Integrated elastic deformation

To calculate the radial expansion or contraction of moulin size, we must know the total elastic deformation of the moulin wall. This is the spatial integral of ϵ_r , from the borehole wall ($r = a$) to the end of the domain ($r = \infty$). Deformation will be greatest at the borehole wall ($r = a$) and will fall off to zero as $r \rightarrow \infty$.

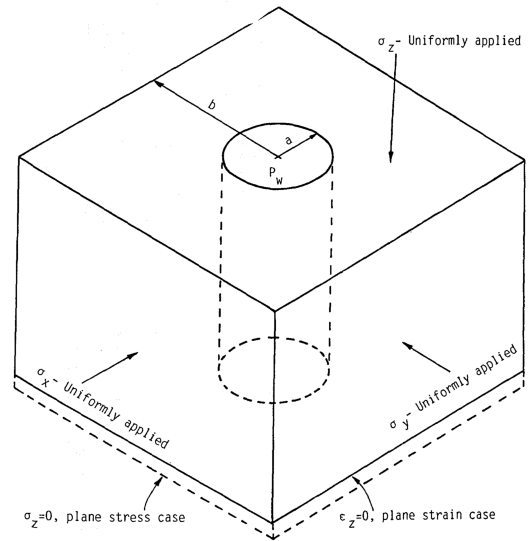


Figure S1: Problem setup, adapted from Aadnøy [1987], of a borehole in a rock medium. We adapt this to a cylindrical moulin through ice. We use the plane strain case, although the plane stress case is equivalent within 7%.

Integrating Eqn. S2 over $r|_{\infty}^a$ entails integrating each stress from Eqn. S1 over the same limits, then summing them together with the appropriate constants involved. So, must simply integrate all the r -dependent terms in the Eqn. S1 stresses over $r|_{\infty}^a$. We ignore any constant (r -independent) terms in Eqn. S1 because these do not contribute to spatially varying deformation.

Eqn. S1 with the constants removed are as follows:

$$\begin{aligned}\sigma_r^* &= \left(\Delta P - \frac{\Delta\sigma_x + \Delta\sigma_y}{2} \right) \left(\frac{a^2}{r^2} \right) + \left(\frac{\Delta\sigma_x - \Delta\sigma_y}{2} \cos 2\theta + \Delta\tau_{xy} \sin 2\theta \right) \left(\frac{3a^4}{r^4} - \frac{4a^2}{r^2} \right) \\ \sigma_\theta^* &= - \left(\Delta P - \frac{\Delta\sigma_x + \Delta\sigma_y}{2} \right) \left(\frac{a^2}{r^2} \right) - \left(\frac{\Delta\sigma_x - \Delta\sigma_y}{2} \cos 2\theta + \Delta\tau_{xy} \sin 2\theta \right) \left(\frac{3a^4}{r^4} \right) \\ \sigma_z^* &= (-2\nu (\Delta\sigma_x - \Delta\sigma_y) \cos 2\theta - 4\nu \Delta\tau_{xy} \sin 2\theta) \left(\frac{a^2}{r^2} \right)\end{aligned}\quad (S3)$$

Indefinite integrals of Eqn. S3 are as follows:

$$\begin{aligned}\int \sigma_r^* dr &= (2\Delta P - (\Delta\sigma_x + \Delta\sigma_y)) \left(\frac{a^2}{2r} \right) + ((\Delta\sigma_x - \Delta\sigma_y) \cos 2\theta + 2\Delta\tau_{xy} \sin 2\theta) \left(\frac{2a^2}{r} - \frac{3a^4}{2r^3} \right) \\ \int \sigma_\theta^* dr &= -(2\Delta P - (\Delta\sigma_x + \Delta\sigma_y)) \left(\frac{a^2}{2r} \right) + ((\Delta\sigma_x - \Delta\sigma_y) \cos 2\theta + 2\Delta\tau_{xy} \sin 2\theta) \left(\frac{3a^4}{2r^3} \right) \\ \int \sigma_z^* dr &= 2\nu \left(\frac{a^2}{r} \right) ((\Delta\sigma_x - \Delta\sigma_y) \cos 2\theta + 2\Delta\tau_{xy} \sin 2\theta)\end{aligned}\quad (S4)$$

These all have dimensions of Pa·m.

Next, we evaluate definite integrals of Eqn. S4, over $r|_{\infty}^a$. Every term in the $r \rightarrow \infty$ expressions go to zero. Similarly, all tangential variations (coordinate θ) do not affect moulin size, so we replace all $\cos 2\theta$ or $\sin 2\theta$ with its average absolute value, $\frac{1}{2}$. This gives

$$\begin{aligned}\int_{\infty}^r \sigma_r^* dr &= a \left(\Delta P - \frac{1}{2}(\Delta\sigma_x + \Delta\sigma_y) + \frac{1}{4}(\Delta\sigma_x - \Delta\sigma_y) + \frac{1}{2}\tau_{xy} \right) \\ \int_{\infty}^r \sigma_\theta^* dr &= a \left(-\Delta P + \frac{1}{2}(\Delta\sigma_x + \Delta\sigma_y) + \frac{3}{4}(\Delta\sigma_x - \Delta\sigma_y) + \frac{3}{4}\Delta\tau_{xy} \right) \\ \int_{\infty}^r \sigma_z^* dr &= \nu a ((\Delta\sigma_x - \Delta\sigma_y) + 2\Delta\tau_{xy})\end{aligned}\quad (S5)$$

Finally, we take a linear combination of Eqns. S5: a sum with the appropriate coefficients from Hooke's Law (Eqn. S2) to get the strain in the r , θ , and z directions, although we discard strain in the θ or z directions. We thus obtain u_r , the total radial deformation in r , by $u_r = \int_{\infty}^a \epsilon_r dr$.

$$\begin{aligned}
u_r &= \int_{\infty}^a \epsilon_r dr = E^{-1} \left[\int_{\infty}^a \sigma_r^* dr - \nu \left(\int_{\infty}^a \sigma_{\theta} dr + \int_{\infty}^a \sigma_z dr \right) \right] \\
&= \frac{a}{E} \left[(1 + \nu) \left(\Delta P - \frac{1}{2}(\Delta\sigma_x + \Delta\sigma_y) \right) + \frac{1}{4}(\Delta\sigma_x - \Delta\sigma_y)(1 - 3\nu - 4\nu^2) + \frac{1}{4}\Delta\tau_{xy}(2 - 3\nu - 8\nu^2) \right] \\
&\text{for } \Delta P = \rho_w g(\Delta h_w - z) - \rho_i g(\Delta H_i - z) = \Delta P_w - \Delta P_i
\end{aligned} \tag{S6}$$

In the moulin model, we assume that all pressure changes ΔP are due to changes in water level Δh_w and that the ice thickness H_i stays constant. Thus, $\Delta P = \rho_w g(\Delta h_w - z) = \Delta P_w$.

As a check, the integrated displacement u_r (Eq. S6) increases with moulin radius a . This makes sense as a tighter radius of curvature (low a) is more difficult to deform radially (low u_r). Inward deformation (moulin closure) will have negative u_r and outward deformation (moulin expansion) will have positive u_r .

For a typical Greenland Ice Sheet moulin with radius $a \sim 1$ meter, the pressure change associated with $\Delta h_w \sim 1$ meter will induce elastic deformation of a few micrometers. This water level change would typically occur over many minutes to a few hours, yielding elastic deformation of up to some 10^{-4} meters per day.

S1.4 Simplest case: Non-varying deviatoric and shear stresses

The deviatoric and shear stresses σ_x , σ_y and τ_{xy} are generally not well known and are variable from place to place in the ablation zone. The spatial variation typically occurs over scales of a few kilometers, and the range may be roughly $[-50 \text{ kPa } +50 \text{ kPa}]$. However, Eq. S6 uses their changes over a time interval, $\Delta\sigma_x$, $\Delta\sigma_y$ and $\Delta\tau_{xy}$. For a moulin advecting through the ablation zone at $\sim 100 \text{ m/yr}$, the stress changes $\Delta\sigma_x$, $\Delta\sigma_y$ and $\Delta\tau_{xy}$ are trivial ($\sim 1 \text{ kPa}$) over a melt season. Thus, we make a further simplification that $\Delta\sigma_x = \Delta\sigma_y = \Delta\tau_{xy} = 0$, which yields the most basic expression for radial elastic deformation u_r :

$$u_r = \frac{a}{E}(1 + \nu)\Delta P \tag{S7}$$

This is the same equation as is commonly used for dilatometer testing in rock mechanics [Goodman, 1989, page 190].

S1.5 Instantaneous elastic deformation and calculated deformation rates

Elastic displacement is an instantaneous process that occurs in reaction to a change in stress. In the case of a moulin during the melt season, the water level in the moulin changes essentially

continuously, which induces continuous changes in pressure (ΔP), which drives continuous elastic deformation (Eqs. S6–S7), although we calculate it only once per timestep. To compare elastic deformation (instantaneous) to viscous deformation (occurring over a time interval), we assume the deformation rate occurs over the entire timestep:

$$\text{elastic deformation rate} = \frac{u_r}{\Delta t} \quad (\text{S8})$$

This is analogous to how we calculate a viscous deformation rate or a rate of refreezing.

More precisely, one could express this in terms of the rate of pressure change, $\frac{\Delta P}{\Delta t}$:

$$\frac{u_r}{\Delta t} = \frac{a}{E}(1 + \nu)a\frac{\Delta P}{\Delta t} \quad (\text{S9})$$

This approach assumes that the water pressure varies smoothly over the time interval in question. This is generally true: we run the model at 5-minute timesteps, and the most common discontinuous variations in pressure are likely sourced from rain storms or other sudden melt events (time scales of hours).

References

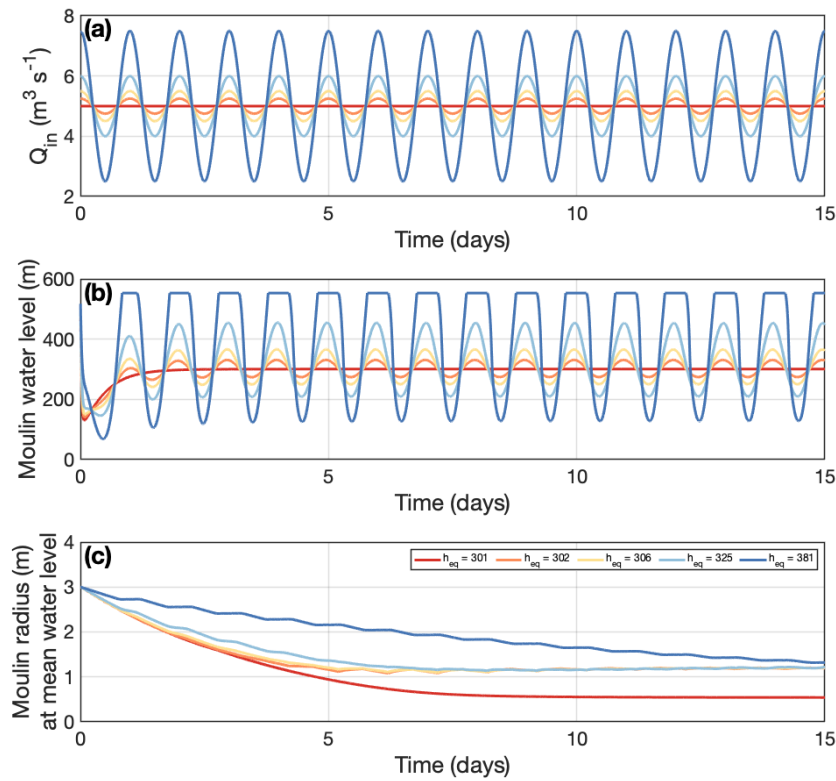
- Bernt Sigve Aadnøy. A Complete Elastic Model for Fluid-Induced and In-Situ Generated Stresses with the Presence of a Borehole. *Energy Sources*, 9:239–259, 1987.
- Lennart Fransson. Ice Handbook for Engineers. *Lulea Tekniska Universitet*, pages 1–31, 2009.
- Richard E Goodman. *Introduction to Rock Mechanics*, volume 2. Wiley New York, 1989. ISBN 9780471812005. URL <https://books.google.com/books?id=ndNRAAAAMAAJ>.
- Ernst Gustav Kirsch. Die theorie der elastizität und die bedürfnisse der festigkeitslehre. *Zeitschrift des Vereines Deutscher Ingenieure*, 42:797–807, 1898. URL <https://books.google.com/books?id=pvBuPwAACAAJ>.

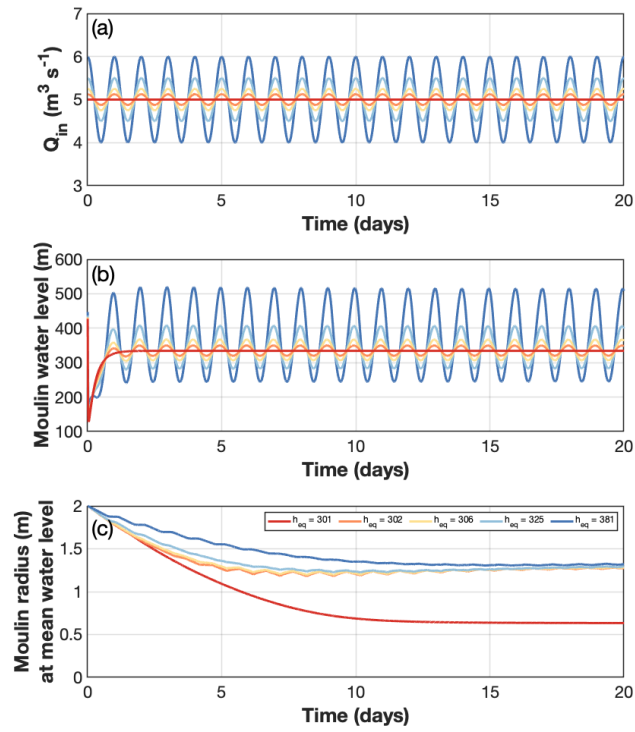
MouSh Sensitivity to model choices

Supplement S2 for “Controls on Greenland moulin geometry and evolution from the Moulin Shape model”, *The Cryosphere*.

S2.1 The impact of diurnal supraglacial variability

Under steadily varying conditions, the modeled moulin should reach a quasi-equilibrium state independent of initial conditions with melting opposing viscous and elastic deformation below the water line and the only change being driven by shear deformation. We examine the quasi-equilibrium state and the impact of supraglacial variability on this state. Increasing the amplitude of the diurnal Q_{in} signal results in an increase in the mean water level but not very little change in the moulin radius at the mean water level apart from an amplitude of zero (Fig. S2). The magnitude of the Q_{in} signal impacts both the mean moulin water level and the radius at that water level (Fig. S3). The increase changes in mean moulin water level is in response to variations in Q_{in} amplitude and magnitude are non-linear (Fig. S4). Further description is included in Sect. 2.5.1 and 3.1.

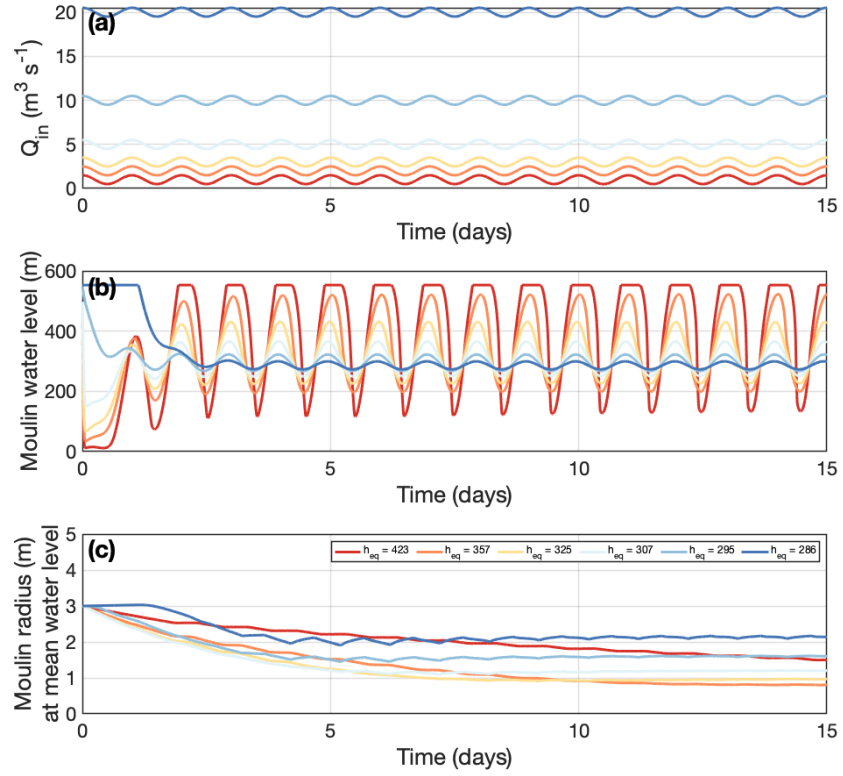




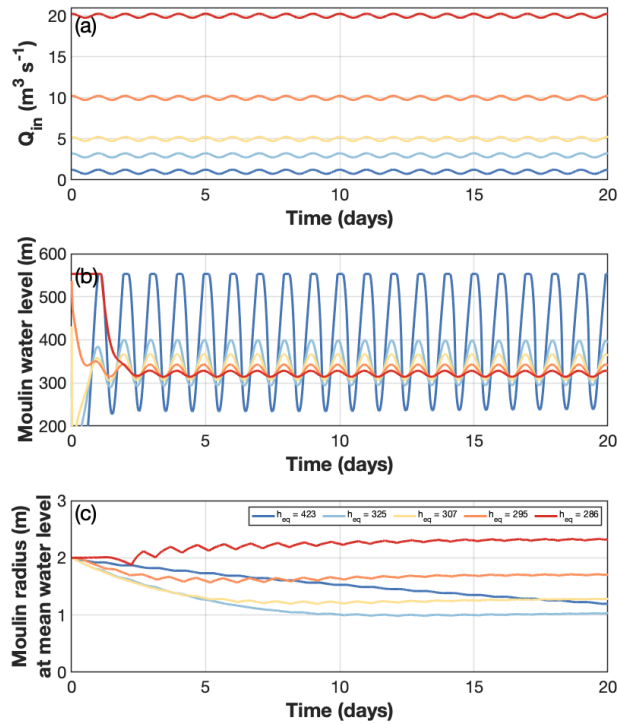
20

21 **Figure S2.** The impact of the Q_{in} amplitude (a) on moulin water level (b) and the major moulin radius at the mean
 22 moulin water level over the last 24 h (c) for 65 different Q_{in} amplitudes, $0 \text{ m}^3 \text{ s}^{-1}$ (red), $0.25 \text{ m}^3 \text{ s}^{-1}$ (orange), $0.5 \text{ m}^3 \text{ s}^{-1}$
 23 ($1 \text{ m}^3 \text{ s}^{-1}$ (mid-blue), $2 \text{ m}^3 \text{ s}^{-1}$ (dark blue). Mean or quasi-equilibrium water levels indicated in (c). All
 24 runs have a magnitude of $5 \text{ m}^3 \text{ s}^{-1}$. Ice thickness is 553 m with flotation at approximately 503 m.

25



26

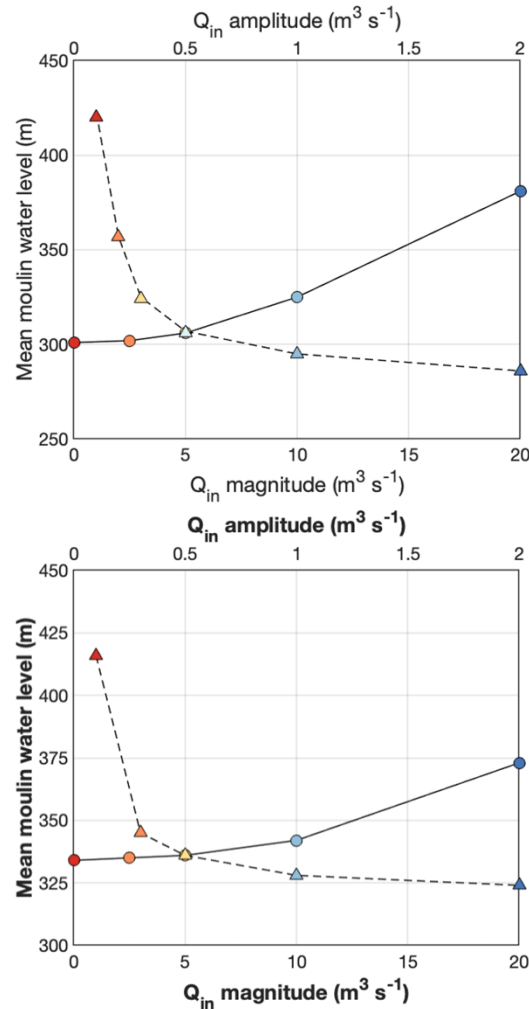


27

28 **Figure S3.** The impact of the Q_{in} magnitude (a) on moulin water level (b) and the major moulin radius at the mean
 29 moulin water level over the last 24 h (c) for 65 different Q_{in} magnitudes, $1 \text{ m}^3 \text{ s}^{-1}$ (red), $2 \text{ m}^3 \text{ s}^{-1}$ (orange), $3 \text{ m}^3 \text{ s}^{-1}$
 30 1 (light blue), $5 \text{ m}^3 \text{ s}^{-1}$ (dark yellow), $5 \text{ m}^3 \text{ s}^{-1}$ (light blue), $10 \text{ m}^3 \text{ s}^{-1}$ (mid-blue), $20 \text{ m}^3 \text{ s}^{-1}$ (dark blue/red). Mean or

31 quasi-equilibrium water levels indicated in (c). All runs have an amplitude of $0.5 \text{ m}^3 \text{ s}^{-1}$. Ice thickness is 553 m with
 32 flotation at approximately 503 m.

33



34

35

36 **Figure S4.** Mean moulin water level as a function of Q_{in} magnitude (circles) and amplitude (triangles).
 37 Colored as indicated in Figures S6 and S7: Q_{in} magnitudes, $1 \text{ m}^3 \text{ s}^{-1}$ (red), $2.3 \text{ m}^3 \text{ s}^{-1}$ (orange), $3.5 \text{ m}^3 \text{ s}^{-1}$ (dark yellow),
 38 $5.1 \text{ m}^3 \text{ s}^{-1}$ (light blue), $10 \text{ m}^3 \text{ s}^{-1}$ (mid-blue), $20 \text{ m}^3 \text{ s}^{-1}$ (dark-blue); Q_{in} amplitudes, $0 \text{ m}^3 \text{ s}^{-1}$ (red), $0.25 \text{ m}^3 \text{ s}^{-1}$ (orange),
 39 $0.5 \text{ m}^3 \text{ s}^{-1}$ (dark yellow), $1 \text{ m}^3 \text{ s}^{-1}$ (mid-light blue), $2 \text{ m}^3 \text{ s}^{-1}$ (dark blue).

40

41

42 S2.2 Sensitivity to model choices

43

44 To explore the impact of various parameterizations and model choices, we perform a set of experiments that examine
 45 the impact of various parameterizations and model choices on the MouSh modeled moulin water level and moulin
 46 capacity, two components of a moulin that can directly impact the englacial and subglacial hydrologic systems. In
 47 each model run, all characteristics and forcings are kept the same as in the control run, except the parameterization of
 48 interest. Specific details are detailed below, and the results of these exploratory runs are in Figure S5 and Figure S6.
 49 All moulin water level differences are presented as $test - control$ and percentage differences are $(test - control) /$
 50 $control$.

51

52 **S2.2.1 Control run**

53 The control run is the Basin 1 experiment detailed in Sect. 2.5.2 and Table 2, with the exception that diurnal variability
54 of Q_m is reduced by 30% to prohibit prolonged periods when daily peak water levels overtop the moulin.
55

56 **S2.2.2 Circular geometry (Experiment 1)**

57 The circular run uses a circular cross-sectional area. In practice, this simply means that open channel melting above
58 the water line is applied uniformly around the moulin perimeter (instead of only to r_2 as in the elliptical formulation)
59 such that the moulin plan view cross-sectional area is circular and only one radius is evolved. Deformation due to
60 elastic, viscous and turbulent melting below the water line is then only calculated for the single radius. This
61 parameterization removes any asymmetry ~~except for that imposed by shear deformation~~. Both runs have the same
62 initial circular plan view cross-sectional area.
63

64 The use of a circular geometry has little impact on moulin water level over the course of the melt season (Fig. S5a).
65 Compared to the control run, the circular geometry generally exhibits slight increases in moulin water level (< 0.5 m).
66 These increases become slightly higher at higher Q_m values; ~~or during one period at the end of the melt season.~~
67 ~~However, differences never exceed 3 m.~~ The primary difference comes in the moulin capacity; ~~which: the circular~~
68 ~~geometry can be up to 4731% smaller approaching than the control moulin as~~ the end of the melt season approaches
69 (Fig. S5b). This difference is concentrated in regions that are not generally water filled except at high water levels,
70 thus has limited impact on moulin water level ~~until the end of the melt season when water levels are highest and the~~
71 ~~control moulin has evolved most substantially from the circular initial condition.~~ This difference is the result of the
72 control moulin run becoming more elliptical.
73

74 **S2.3 Surface stress impact**

75 ~~Currently, elastic deformation is based on the Aadnøy (1987), which describes the stresses around a vertical hole. The~~
76 ~~default deviatoric and stress values are $\sigma_x = 0 \text{ kPa}$, $\sigma_y = 50 \text{ kPa}$, and $\tau_{xy} = -50 \text{ kPa}$, based on a remote~~
77 ~~sensing study (Poinar and Andrews, 2020). However, these values are generally poorly constrained. We examine~~
78 ~~higher surface stresses $\sigma_x = 0 \text{ kPa}$, $\sigma_y = 500 \text{ kPa}$, and $\tau_{xy} = -500 \text{ kPa}$ (10x surface stresses) and the simplest~~
79 ~~case, deviatoric and shear stresses equal to zero: $\sigma_x = \sigma_y = \tau_{xy} = 0 \text{ kPa}$ (Zero surface stresses). Our derivation of~~
80 ~~deviatoric and shear stress equations and out parameterization for time variation can be found in Supplement S1.~~
81

82 ~~Deviatoric and shear stresses primarily impact the near surface, unsubmerged regions. Therefore, the impact on moulin~~
83 ~~water level is minimal, except during the beginning and end of the melt season when water levels are high (Fig. S5c).~~
84 ~~Though overall the difference in moulin water levels between 10x surface stresses or Zero surface stresses and the~~
85 ~~control run is on the order of +/- 1 m. Zero surface stresses results in a slightly larger moulin (up to 8.5% by the end~~
86 ~~of the melt season), while 10x surface stresses results in a slightly smaller moulin (up to 29% by the end of the melt~~
87 ~~season) (Fig. S5d). This comparison suggests that the simplifying case (Zero surface stresses) has minimal impact on~~
88 ~~the model results except during periods when water levels comparatively higher than the mean water level.~~
89

90 **S2.2.3 Elastic deformation (Experiment 2)**

91 ~~For completeness, we include elastic deformation within the moulin model. Our formulation is dependent on the~~
92 ~~change in moulin water level and the moulin radius (Supplement 1). Thus, elastic deformation within MouSh is~~
93 ~~substantially smaller than viscous deformation due to the relatively small moulin radii modeled here. We examine~~
94 ~~whether the inclusion of elastic deformation impacts moulin water level and capacity by performing a run without~~
95 ~~elastic deformation.~~
96

97 ~~In its current formulation, the exclusion of elastic deformation has almost no impact on moulin water level and capacity~~
98 ~~(Fig. S5c-d). This comparison suggests that the simplifying case (no elastic deformation) has minimal impact on the~~
99 ~~model results.~~
100

101 **S2.2.4 Distance from terminus (Experiment 3)**

102 In our simple parameterization of the subglacial model, the hydraulic gradient is set by the water level in the moulin
103 and the distance from the terminus. Because the hydraulic gradient exerts an important control over both the subglacial

104 channel and moulin evolution, we examine the impact of different subglacial lengths (L). We compare the control run,
105 $L = 13.6$ km, to model runs with one half, $L = 6.8$ km, and one and one half, $L = 20.4$ km while using the same ice
106 thickness (553m). This change directly impacts the hydraulic gradient calculated in Eq. 28.24.

107

108 Modifying the distance from terminus and the associated hydraulic gradient can result in substantial changes to both
109 the moulin water level ($\pm \sim 200$ m) and moulin capacity ($\pm \sim 40$ %; Fig. S5e-f). Reducing Shortening L
110 reduces both moulin water level and moulin capacity. Lower water levels reduce water velocities and allows viscous
111 and elastic deformation to increase, resulting in a smaller moulin. While increasing L results in higher moulin water
112 levels and a larger moulin. Higher moulin water levels increase turbulent melting linearly and reduce viscous and
113 elastic deformation non-linearly. In addition, with a longer L , the moulin has more instances of water level being
114 above floatation, which permits viscous and elastic deformation to open the moulin. The difference in moulin water
115 levels tends to be exacerbated during higher Q_{in} values (Fig. S5e), resulting in larger differences from the control run
116 during the middle of the melt season and less impact during the onset and cessation of melting.

117

118 S2.2.5 Base flow (Experiment 4)

119 Our simple parameterization of the subglacial system means that the model represents only a single moulin and a long
120 channel. This is an oversimplification of what is generally a complex arborescent network (e.g., Werder et al., 2013)
121 with multiple moulins along a single channel (Andrews et al., 2014). To parameterize this connectivity, we prescribe
122 a base flow term to be 5 times the 5-day lagged moving average moulin input directly into the subglacial channel-
123 (Fig. 6a). This definition removes diurnal signals but preserves melt events and the seasonal pattern of melt. Without
124 baseflow, MouSh can produce unrealistically high water levels with realistic meltwater inputs. While an alternative
125 would be to either substantially dampen the diurnal variability or increase moulin inputs, we believe that our current
126 approach best approximates the natural system. Unfortunately, prescribing a larger initial subglacial cross-sectional
127 area does not mitigate the above problem because moulin and subglacial channel size are not dependent on the initial
128 conditions after several days the first few weeks. Here we examine the impact of reducing the base flow to 2 times the
129 5-day lagged moving average.

130

131 The prescribed base flow acts to maintain a larger subglacial channel and permits more rapid growth due to melting;
132 this behavior is non-linear (see Eq. 28). Therefore, reducing the amount of base flow into the subglacial system
133 reduces the ability of the subglacial channel to accommodate the large diurnal swings in Q_{in} . Therefore, a reduction in
134 base flow results in higher moulin water levels for much of the model run (Fig. S5g). Interestingly though, during
135 diurnal minimums, the water levels are lower in the low base flow run relative to the control (negative values in Fig
136 S5g). This is likely due to greater moulin growth (increased turbulent melting and reduced or negative viscous and
137 elastic deformation) associated with higher water levels. The moulin capacity difference displays a clear seasonal
138 pattern (Fig. S5h). Early in During the tails of the melt season, the lower base flow run exhibits a smaller similar
139 capacity due to less total water in the system control, but as diurnal variability and maximum daily water levels increase
140 to above floatation, the low baseflow moulin begins to grow relative to the control run moulin.

141

142 S2.2.6 Static subglacial geometry (Experiment 5)

143 The MouSh model is meant to model moulin geometry. However, to permit water flow through the moulin, we include
144 a simple time-evolving subglacial channel (Sect. 2.4.2). A fixed subglacial channel would, in essence, provide the
145 simplest subglacial component. However, a fixed subglacial channel results in both extremely low and extremely high
146 moulin water levels when Q_{in} values are both high and low, respectively; therefore, during a run an experiment with
147 seasonally evolving Q_{in} , the subglacial channel size must be chosen very carefully to produce vaguely realistic moulin
148 water levels and capacities. Therefore, we examine the impact of fixing the subglacial cross-sectional area S using a
149 fixed ~~cosinusoidal run~~ ~~co-sinusoidal supraglacial~~ of 8040 days (as described in Eq. 22). For this comparison, we fix S
150 $= 21.95$ m² (Fixed S), which is approximately equal to the mean value of the subglacial channel cross-sectional area in
151 the control run experiment; this minimizes differences between the runs.

152

153 The moulin with a fixed subglacial cross-sectional area has similar quasi-equilibrium water levels but less diurnal
154 variability in both moulin water level and water storage than the moulin (Fig. 6b). The model run with a variable fixed
155 subglacial cross-sectional area (Fig. S6) channel also displays a slightly lower radius at the mean water level of the
156 last 10 experiment days. The primary conclusion here is that the moulin geometry and variability is, at least in part,
157 driven by the characteristics of the subglacial hydrologic model used. Such dependency is not uncommon in models

158 of the glacial hydrologic system. For example, the presence of modeled channels is dependent on the prescribed
159 location of supraglacial inputs and prescribed conductivity of the surrounding system. Therefore, the subglacial model
160 used with the MouSh model should be carefully considered.

161

162

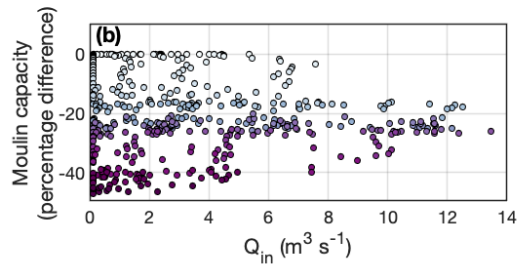
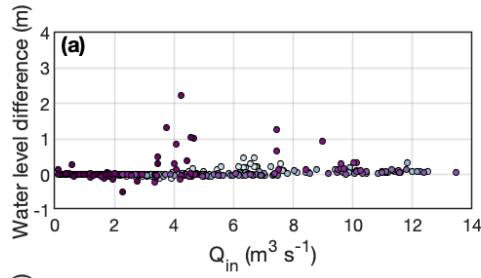
163

164

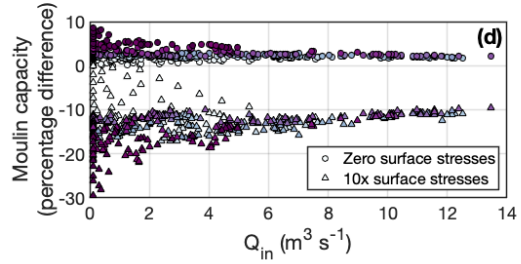
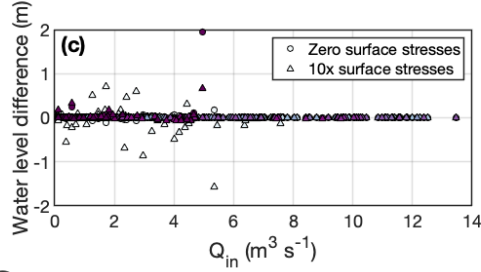
165

|

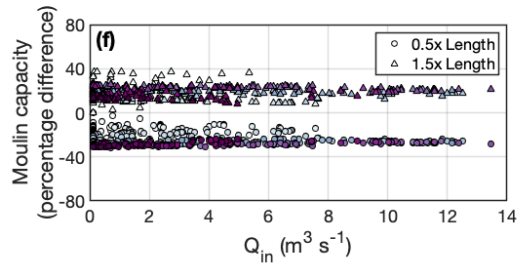
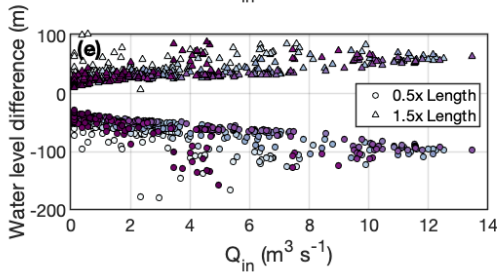
Circular geometry



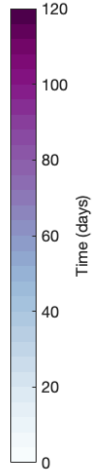
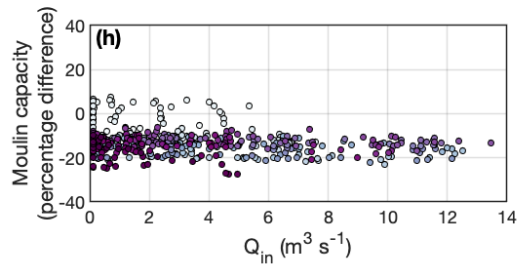
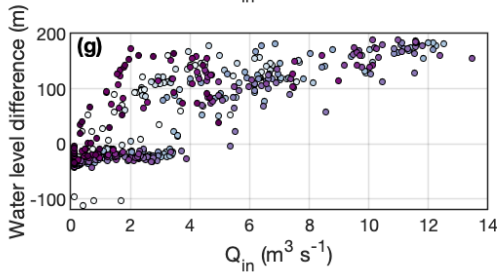
Surface stresses

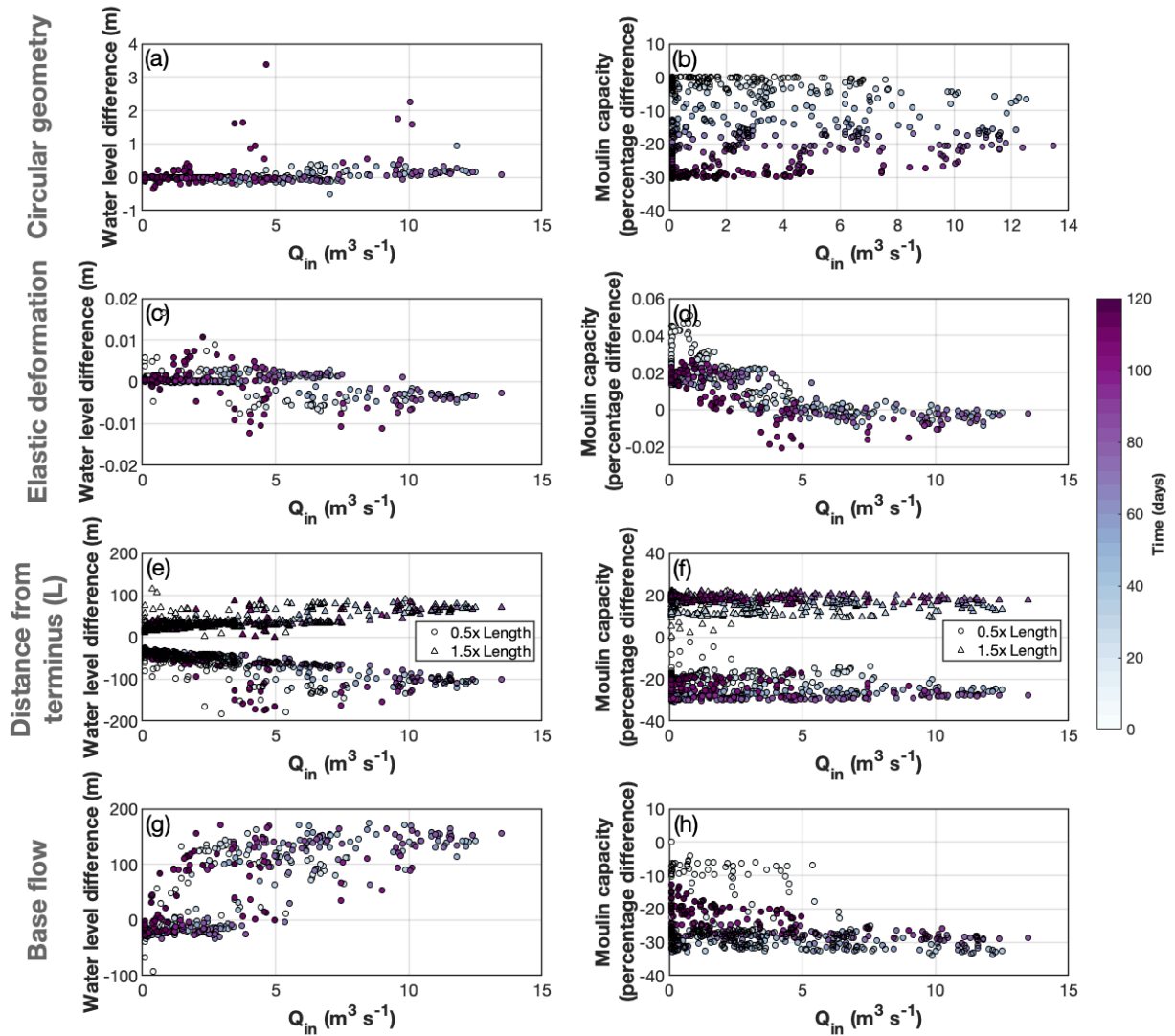


Distance from terminus (L)



Base flow





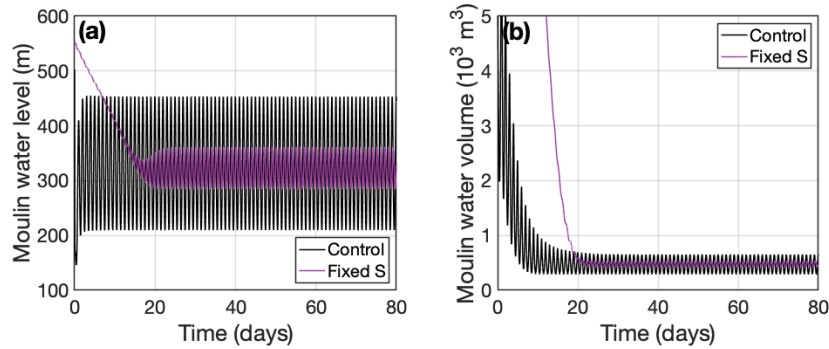
167

168

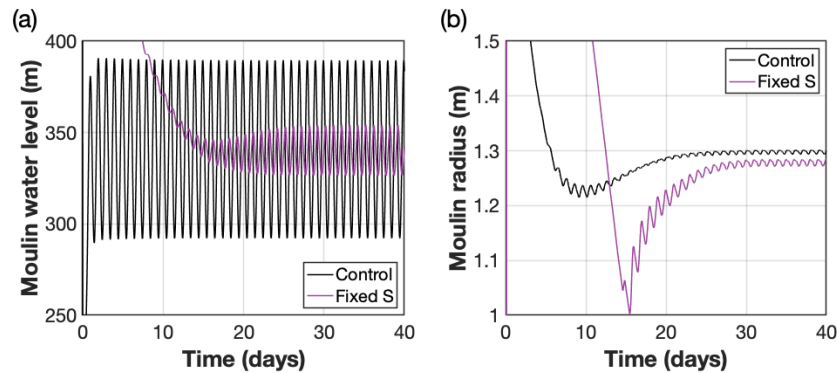
169 **Figure S5.** Moulin water level and capacity differences relative to the Basin 1 ($H_i = 553$ m) control run for a circular
 170 geometry (a-b); ~~varying surface stresses~~elastic deformation (c-d); varying distances from the terminus or subglacial
 171 path length (L ; e-f); and a reduced baseflow (g-h). In all panels on the left-hand side, the differences are experiment
 172 minus control. In all panels on the right-hand side, moulin capacity is plotted as a percent difference from the control
 173 run such that positive values indicate a capacity larger than the control run and negative values indicate a capacity
 174 smaller than the control run.

175

176



177



178

179 **Figure S6.** Moulin water level (a) and moulin radius at the mean water volume level (b) from experimental runs with
 180 a run experiments with variable subglacial S (*Control*; black) and a fixed subglacial cross-sectional area of 21.95 m²
 181 (*Fixed S*; purple).

182

183 References

184 Aadnøy, B. S.: A complete elastic model for fluid-induced and in-situ generated stresses with the presence of a
 185 Borehole, 9, 239–259, 1987.

186 Andrews, L. C., Catania, G. A., Hoffman, M. J., Gulley, J. D., Lüthi, M. P., Ryser, C., Hawley, R. L., and Neumann,
 187 T. A.: Direct observations of evolving subglacial drainage beneath the Greenland Ice Sheet, *Nature*, 514, 80–83,
 188 <https://doi.org/10.1038/nature13796>, 2014.

189 Werder, M. A., Hewitt, I. J., Schoof, C. G., and Flowers, G. E.: Modeling channelized and distributed subglacial
 190 drainage in two dimensions, *J. Geophys. Res. Earth Surf.*, 118, 2140–2158, <https://doi.org/10.1002/jgrf.20146>, 2013.